**An Integrated Flywheel Energy Storage System with a Homopolar Inductor Motor/Generator and High-Frequency Drive**

by

Perry I-Pei Tsao

B.S. (Massachusetts Institute of Technology, Cambridge) 1997
M.S. (University of California, Berkeley) 1999

A dissertation submitted in partial satisfaction of the
requirements for the degree of
Doctor of Philosophy

in

Engineering-Electrical Engineering and Computer Sciences

in the

GRADUATE DIVISION
of the
UNIVERSITY OF CALIFORNIA, BERKELEY

Committee in charge:
Professor Seth R. Sanders, Chair
Professor Ronald S. Fearing
Professor Dennis K. Lieu

Fall 2003

The dissertation of Perry I-Pei Tsao is approved:

Chair Date

Date

Date

University of California, Berkeley

Fall 2003

**An Integrated Flywheel Energy Storage System with a Homopolar Inductor Motor/Generator and High-Frequency Drive**



by

Perry I-Pei Tsao

# Abstract

An Integrated Flywheel Energy Storage System with a Homopolar Inductor Motor/Generator and High-Frequency Drive

by

Perry I-Pei Tsao

Doctor of Philosophy in Engineering-Electrical Engineering and Computer Sciences

University of California, Berkeley

Professor Seth R. Sanders, Chair

This thesis presents the design, construction, and test of a high-speed integrated flywheel energy storage system. This flywheel system integrates a homopolar inductor motor/alternator and a steel energy storage rotor to achieve high power density energy storage using low-cost materials. A six-step inverter drive strategy that minimizes inverter VA-rating and enables high frequency operation is also implemented.

Lumped parameter design equations are developed, and used to optimize the flywheel system. Analytical expressions for rotor and stator losses from harmonics in the six-step drive are also developed.

A prototype flywheel energy storage was built. A novel method for constructing the slotless stator was developed and implemented. The prototype flywheel was designed for $30kW$ of power, $140W \cdot hr$ of energy storage, and an operating speed range of $50,000rpm$ - $100,000rpm$.

Experiments were conducted for speeds up to $60,000rpm$ and power levels up to $10kW$.

System efficiencies of 83%, which includes losses in the power electronics and the motor, were achieved. Most experimental results were in line with designed values. Experimental measurements of the harmonic losses showed very good agreement with the analytical calculations, and demonstrated that low rotor losses had been achieved.

Professor Seth R. Sanders
Dissertation Committee Chair

To Celia

# Contents

# List of Figures

# List of Tables

## Acknowledgments

I received a great deal help from many people in the course of working on this thesis. I'd like to thank my advisor Seth for his advice and encouragement, Matt Senesky for his helping hand in lab, and Warner Carlisle, Joe Gavazza, and Ben Lake of the ERL Machine Shop for their tremendous help in the construction and design of the prototype. I'd also like to acknowledge my parents and Celia for their patience and continual support.

# Chapter 1

# Introduction

This work describes the design of an integrated flywheel energy storage system with a homopolar inductor motor/generator and a high frequency drive for high power applications. A system level design methodology for integrated flywheels and detailed design and analysis of the motor/generator of the flywheel system are presented. In this introduction, background information on applications for flywheels, competing energy storage technologies, different flywheel technologies, and an overview of this thesis are presented.

## 1.1 High Power Energy Storage Applications

Some energy storage applications require high peak power output but for only a short amount of time, so the total amount of energy required is small. One example is in hybrid electric vehicles, where a high power electrical energy storage system is used to augment the power of an internal combustion engine (ICE) during rapid acceleration and to recover energy during regenerative braking. The use of this transient energy storage system improves the efficiency of the ICE by allowing it to run at more efficient operating points. Although the peak power during acceleration

and braking can be quite high, the time period for full-power acceleration and braking is only on the order of 10's of seconds, and thus requires only a modest amount of energy storage.

A second example is in power quality applications. Many sensitive industrial process can be severely impacted by momentary voltage sags or outages. Examples include data centers, semiconductor production, and paper production. In these instances, even a very short outage can cause hours of downtime and production loss. It has been estimated that over 80% of utility power problems last less than 1 second [15], so an energy storage system capable of supplying power for only a few seconds can greatly reduce the frequency and resulting damage from these power quality problems.

Both these applications share the characteristic of high peak power requirements with only modest energy storage requirements. The question is"What type of energy storage technology is best suited for this type of applications?" The term "best suited" assumes that the minimum requirements for the application are met, and usually refers to some balance between "lightest weight," "smallest volume," or "least expensive."

The notion of "least expensive" can be determined by comparing the $\$/kW$ and $\$/kW \cdot hr$ parameters for each technology (which ideally should include maintenance, disposal, and other life-cycle costs). Four basic performance parameters can be used determine to gauge the other three facets of "best suited." The first four performance parameters to consider are the specific power ($W/kg$), power density ($W/l$), specific energy ($W \cdot hr/kg$), and energy density ($W \cdot hr/l$). The terms "gravimetric power/energy density" and "volumetric power/energy density" are also used, but the first set of terms will be used here. Obviously, there are many other important factors to consider, such as efficiency, reliability, or speed of response, but these basic performance parameters provide a good starting point.

In the high power energy storage applications under consideration here, the limiting factor on improved performance is often the ability to meet the peak power requirement for the application. For these applications, a higher specific power, a higher power density, or lower $\$/kW$ would improve performance more than higher specific energy, higher power density, or lower $\$/kW \cdot hr$. Improved performance could mean anything from a more mileage efficient car to a smaller power quality solution. The development of the flywheel system in this thesis is aimed at these applications.

## 1.2 Competing Technologies

### 1.2.1 Batteries

Currently, batteries are by far the most widely used technology for these applications. The most commonly used batteries are lead-acid and nickel metal-hydride (NiMH) type batteries. Lead-acid batteries are often used in stationary applications such as back up power supplies where low cost is most important, and NiMH batteries are the most widely used for hybrid electric vehicles because of their higher specific power, higher power density, and longer lifetime. The Honda Civic Hybrid, Honda Insight, and Toyota Prius all use NiMH batteries.

There are several drawbacks to using batteries in high power applications, however. Since batteries have lower specific and volumetric power densities than the other technologies, they result in a heavier and larger system. Batteries also have lower efficiencies at high power levels, and can suffer from reduced lifetime under these conditions as well.

### 1.2.2 Ultracapacitors

Ultracapacitors operate similarly to normal capacitors, storing energy by separating charge with a very thin dielectric. The difference is that ultracapacitors have much higher surface area densities, allowing them to store much more energy. As a result, ultracapacitors have a higher power densities and high power efficiencies than batteries. Ultracapacitors are not widely used commercially for high power applications, although they are often used as an alternative to a battery backup system in consumer electronics to provide short term backup power. Although they are a promising technology, they are still expensive, have an unproven lifetime, and have a more limited temperature range than flywheels. Ultracapacitors also tend to have a large series resistance which imposes a large time constant and thus slower response time [9].

### 1.2.3 Flywheels

Flywheel energy storage systems operate by storing energy mechanically in a rotating flywheel. Electrical energy is stored by using a motor which spins the flywheel, thus converting the electric energy into mechanical energy. To recover the energy, the same motor is used to slow the flywheel down, converting the mechanical energy back into to electrical energy. Flywheels have higher power densities, higher efficiency, longer lifetime and a wider operating temperature range than batteries. Although flywheels have lower energy densities than batteries, their energy density is high enough to meet the requirements for many high power applications and still realize performance benefits over batteries.

There are two basic classes of flywheels based on the material used in the rotor. The first class uses a rotor made up of an advanced composite material such as carbon-fiber or graphite. These materials have very high strength to weight ratios, which give flywheels the potential of

having high specific energy. The second class of flywheels uses steel as the main structural material in the rotor. This class includes traditional flywheel designs which have large diameters, rotate slowly, and low power and energy densities, but also includes some newer high performance flywheels as well, such as the one made by Activepower, Inc. [32] and the one presented in this thesis. The flywheel in this thesis is an integrated flywheel, which means that the energy storage accumulator and the electromagnetic rotor are combined in a single-piece solid steel rotor. By using an integrated design, the energy storage density of a high power steel rotor flywheel energy storage system can approach that of a composite rotor system, but avoid the cost and technical difficulties associated with a composite rotor. The advantages of integrated flywheel systems are discussed in more depth in Chapter 2.

### 1.2.4 Comparison of Technologies

Fig. 1.1 plots the specific power and specific energy for lead-acid and NiMH batteries, ultracapacitors [9], and various examples of steel rotor ("Active Power" [32], "Piller" [22], "U. Newcastle" [11], and "UC Berkeley" the flywheel described in this thesis), and composite rotor ("Trinity" [5], "Beacon Power" [27], and "ETHZ" [3]) flywheels. Also plotted are three lines indicating the range of specific power and specific energy required for power-assist HEVs, dual-mode HEVs, and EVs. For example, the line for the parallel hybrid electric vehicle indicates that an energy storage unit with a specific power between $600W/kg$ and $3000W/kg$ and a specific energy between $3W \cdot hr/kg$ and $20W \cdot hr/kg$ would be suitable for a power-assist hybrid electric vehicle.

The power-assist and dual-mode HEV requirements were determined by the Department of Energy (DOE) and used as minimum and desired goals for the energy storage development in the Partnership for the Next Generation Vehicles (PNGV) program [29]. In power-assist HEVs

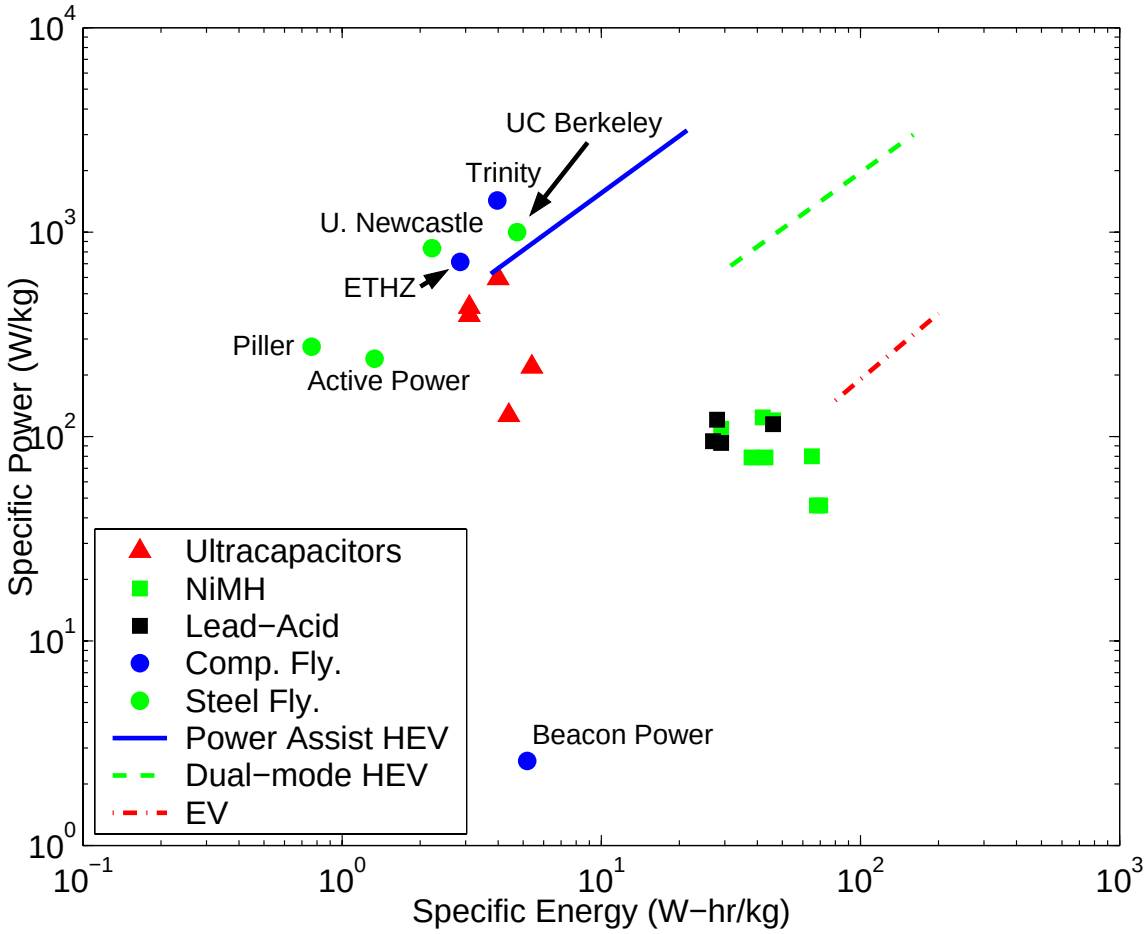


Figure 1.1: Comparison of specific energy and specific power.

the energy storage is primarily used to augment the internal combustion engine (ICE) during acceleration and regenerative braking, while in dual-mode HEVs the energy storage system is used for longer period of time and may be able to power the vehicle over a certain distance independent of the ICE. The EV requirement is drawn from the US Advanced Battery Consortium's (USABC) development goals.

This graph highlights how flywheels and ultracapacitors have much higher specific power, and batteries have a much higher energy density. Also, it should be noted that the desired specific power and specific energy varies for the different applications, and that batteries are not as

well suited to applications in power-assist hybrid electric vehicles as flywheels or ultracapacitors.

## 1.3 Thesis Overview

The remainder of this work focuses on the design of an integrated steel rotor flywheel energy storage system. The goal of this project is to design a high power density, high efficiency, flywheel system that is a performance and economically competitive alternative to batteries for high power applications. The contributions of this thesis center around three main areas: integrated flywheel design, homopolar inductor motor design for flywheels, and high-frequency drive design.

A description of the advantages of integrated flywheel energy storage systems is presented in Chapter 2. In the second part of Chapter 2, the reasons for choosing a homopolar inductor motor for an integrated flywheel are presented. The equations for designing and modeling a homopolar inductor motor are developed in Chapter 3.

A design methodology for integrated flywheel systems is presented in Chapter 4. The high-frequency six-step drive scheme and sensorless controller design is presented in Chapter 5. An analysis of harmonic currents induced by the six-step drive and associated copper and rotor losses is presented in Chapter 6.

As a demonstration of the above concepts, a prototype integrated flywheel energy storage system incorporating a homopolar inductor motor, high-frequency six-step drive, and sensorless control is built and its experimental results are presented. The construction of the prototype is detailed in Chapter 7. Experimental results are then presented and analyzed in Chapter 8 and conclusions are presented in Chapter 9.

# Chapter 2

# Flywheel Energy Storage Systems

This chapter introduces the key system design issues for flywheel energy storage systems. First, the energy storage requirements in hybrid electric vehicles are presented. Then integrated flywheel energy storage systems and their advantages are described. The motor requirements for flywheel systems and homopolar motors are discussed in Section 2.2, and the bearing requirements are discussed in Section 2.3.

## 2.1 Flywheel System Design

The design of the flywheel system begins by examining the requirements for a flywheel energy storage system in a hybrid electric vehicle. Then the rotor design, motor design, and bearing design are discussed.

### 2.1.1 Hybrid Electric Vehicle Energy Storage Requirements

As discussed in the introduction, hybrid electric vehicles and power quality applications share the characteristic that they have high power requirements and modest energy storage re-

| | |
|---|---|
| Power | 30kW |
| Energy storage capacity | 140 W·hr |
| System mass | 36 kg |
| Power density | 833 W/kg |
| Energy density | 3.9W·hr/kg |

Table 2.1: Machine design parameters

quirements. However, there is a stronger need to minimize weight, volume, and cost in hybrid electric vehicles than for power quality applications, and this translates into tighter performance requirements for the hybrid electric vehicle application. Therefore, the focus of this thesis is on meeting the requirements for a hybrid electric vehicle, with the understanding that a flywheel meeting those requirements will also be suitable for power quality applications. Numerous studies have been conducted to determine the optimal sizing of the energy storage system for a small passenger hybrid electric vehicle [2, 41, 4]. Based on the studies and what would be a feasible goal for a prototype, a design goal of a $30kW$, $140W \cdot hr$ flywheel system was chosen. A table of the parameters is presented in Table 2.1.

Perhaps the best way to evaluate the validity of these studies and whether or not the goals chosen for the prototype would be practical in an HEV is to compare them to the specifications of the commercially available hybrid electric vehicles. In Table 2.2 the Toyota Prius Hybrid is compared to the similar but non-hybrid Toyota Corolla, and likewise, the Honda Civic Hybrid is compared the non-hybrid Honda Civic Coupe. From Table 2.2 it can be seen that the specific power of the battery packs in the hybrids is lower than that of the prototype flywheel, and the hybrids have significantly higher mileage than their non-hybrid counterparts. This suggests that a flywheel would meet the requirements for an HEV, and an HEV passenger car with a flywheel energy storage system of our suggested dimensions would indeed offer a further performance improvement.

| Car | Vehicle Weight | Total Power | Electric Power | Battery Weight kg | Specific Power W/kg | City/Hwy. Mileage (mpg) |
|---|---|---|---|---|---|---|
| Toyota Prius Hybrid | 1260kg | 73kW (98hp) | 33kW (44hp) | 45kg | 733 | 52/45 |
| Toyota Corolla | 1140kg | 97kW (130hp) | – | – | – | 30/39 |
| Honda Civic Hybrid | 1230kg | 64kW (85hp) | 10kW (13.4hp) | 18kg (est.) | 555 | 48/47 |
| Honda Civic Coupe | 1090kg | 85kW (115hp) | – | – | – | 29/38 |

*Sources:* Toyota.com and Honda.com websites. All cars are 2003 model year.

Table 2.2: Hybrid Electric Vehicle and Standard Vehicle Comparison.

Further widespread adoption of hybrid electric vehicles seems likely. Several US automakers have announced plans for hybrid vehicles, and they are reasonably popular with consumers. In December 2001, four years after the first Toyota Prius was introduced in Japan, Toyota announced that it was making a profit on sales of the Prius [30]. Whether or not it makes economic sense for consumers to purchase a hybrid vehicle is still debatable however, because the savings in gasoline consumption and reduced emissions do not make up for the extra cost of the hybrid, except in Japan and Europe where fuel taxes are much higher [26].

Although it seems unlikely that flywheels will overtake the head start that batteries have in small passenger hybrid electric vehicles, the purpose of the above example is to illustrate that a steel rotor flywheel energy storage system can meet the power density requirements even for this demanding of an application. Flywheels are being actively developed for larger vehicles such as military vehicles, buses and trains [16], where the need for higher power density is more pronounced.

### 2.1.2 Integrated Flywheel Design

This section describes the reasoning behind the choice of the basic flywheel configuration chosen for this project. The three basic configurations are described, and comparisons are made in terms of specific power and specific energy. A comparison between a composite and steel rotor is also made.

As shown in Fig. 2.1, there are three basic configurations for a flywheel energy storage. In the "conventional design," the rotor has a large diameter section, where most of the kinetic energy is stored, attached to a smaller diameter section, which is used by the motor to spin the flywheel. This is the most common design and it used in [27, 3, 22], however, this configuration tends to have a larger housing and containment structure because of the additional rotor length.

The second configuration is called a "barrel" or "inside-out" type, which is used in [5]. This design, while advantageous for a composite rotor flywheel which stores energy in a composite ring with lightweight hub in the center, is not an efficient design for an isotropic steel rotor flywheel from the energy storage standpoint.

The third configuration, used in [32, 11] and the UC Berkeley flywheel, is an "integrated design" in which the electromagnetic and energy storage portions of the rotor are combined. This type of design is not well suited for a composite rotor flywheels because of the need for electromagnetic material for torque production, however, unlike the other configurations, in the integrated configuration the housing and stator of the motor comprise a large portion of the vacuum and burst containment for the flywheel. Minimizing the weight of the containment structure is important since the containment structure usually weighs several times more than the rotor. The weight savings from this type of design can be substantial, and additional advantages include lower component count, reduced material costs, lower mechanical complexity, and reduced manufacturing

costs.

**Integrated Steel Rotor Flywheel Systems vs. Composite Rotor Flywheel Systems**

Many flywheels are built with composite rotors because of the higher strength-to-weight ratio of composites versus steel. Unfortunately, the strength advantage is reduced by the additional mechanical complexity of a composite rotor and the safety derating factor necessary for composites. The derating is necessary because the failure behavior for composite materials is more difficult to predict than for steel. Composite rotors also impose a stricter limit on the rotor operating temperature and temperature cycling.

Furthermore, while a composite flywheel of a certain energy storage capacity may have a lighter rotor than a steel flywheel system of the same energy storage capacity, the rotor itself is only a small fraction of the overall flywheel system weight. Since the remainder of the system, such as the stator, containment, and electronics remain basically the same, the reduction in weight is a very small percentage of the total system weight. This is particularly true for high power flywheels designed for discharges in the range of tens of seconds. Since many flywheel systems are aimed at power quality and hybrid vehicle load-levelling applications that require short, high power discharges, many of them fall into this category. However, because the mass of the electromagnetic rotor and stator is a function of power, for flywheels with a high ratio of power-versus-energy-storage, the electromagnetic portions of the rotor and stator will comprise an even larger portion of the system mass, further reducing the advantage of composite rotors.

In a similar manner, the vacuum and burst containment necessary for composite rotors also offsets their advantages over steel rotors, especially when compared to an integrated design where a large portion of the containment structure is comprised by the motor stator and housing.

Perhaps the most attractive feature of a steel rotor integrated flywheel design is that it is

similar in material composition, design, and complexity to a standard electric machine, therefore it is reasonable to expect that for volume production the manufacturing costs of such a flywheel would be comparable to those of a similar-sized electric machine. The cost of a standard electric machine can be estimated based on its weight, and using this method, the cost of a steel rotor integrated flywheel design could be much lower than other designs.

The integrated flywheel configuration can achieve comparable specific energy to a composite rotor flywheel system. While a comparison between a composite rotor and steel rotor of the same weight (disregarding all the other components of the flywheel system) might indicate that twice as much energy could be stored in the composite rotor, the additional housing and containment weight for the composite rotor in a conventional or barrel configuration versus a steel rotor in an integrated configuration offsets this advantage to a certain degree.

As an example, consider a composite rotor $100kW$ and $420W \cdot hr$ flywheel energy storage system with a rotor of mass $40kg$ and total system weight of $545kg$ [5]. The rotor of a steel rotor flywheel with the same energy storage available might weigh two times more, but since the rotor weight is a small fraction of the total system weight and the weight of the remainder of the system remains basically the constant, the steel rotor system would have a specific energy only 7% lower. It would be incorrect to say that a well-engineered composite flywheel energy storage system *could not* have a higher specific energy, but it is argued that a steel rotor flywheel in an integrated configuration could have comparable specific energy at lower complexity and lower cost.

In conclusion, the motivation and goal of this project is to demonstrate that a high power integrated flywheel system with a solid-steel rotor can achieve similar performance to a composite rotor flywheel system, with less complexity, lower manufacturing costs, and lower material costs.

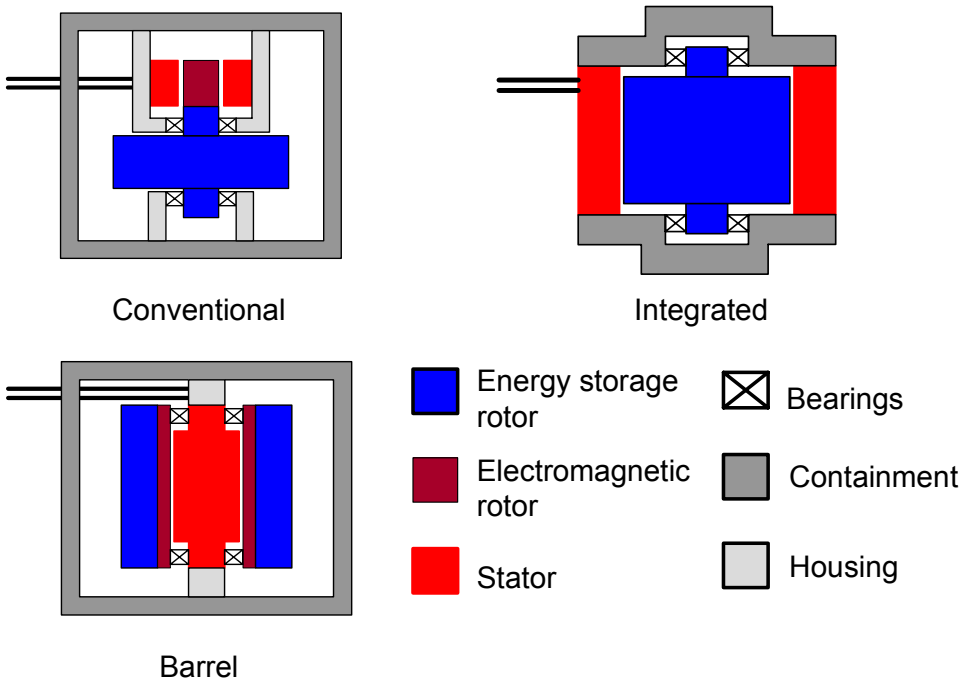


Figure 2.1: Various flywheel configurations.

## 2.2 Flywheel Motors

High efficiency, a robust rotor structure, and low rotor losses, are the key requirements for a flywheel system's motor/generator. High efficiency is required so that the flywheel can be an effective energy storage medium. Motor efficiency must be high over the entire speed and power range of operation, in this case $50,000rpm$ to $100,000rpm$, with a power rating of up to $30kW$. In addition, the zero power spinning losses of the machine must be very low. A robust rotor structure is necessary for obvious reliability and safety reasons.

The third requirement of low rotor losses is also critical and drives many of the design decisions in a flywheel system. Because high-speed flywheels operate in a vacuum to reduce windage losses, the main paths for heat transfer from the rotor are through radiation and through the bearings (if ball bearings are used). The amount of heat transfer through radiation is small

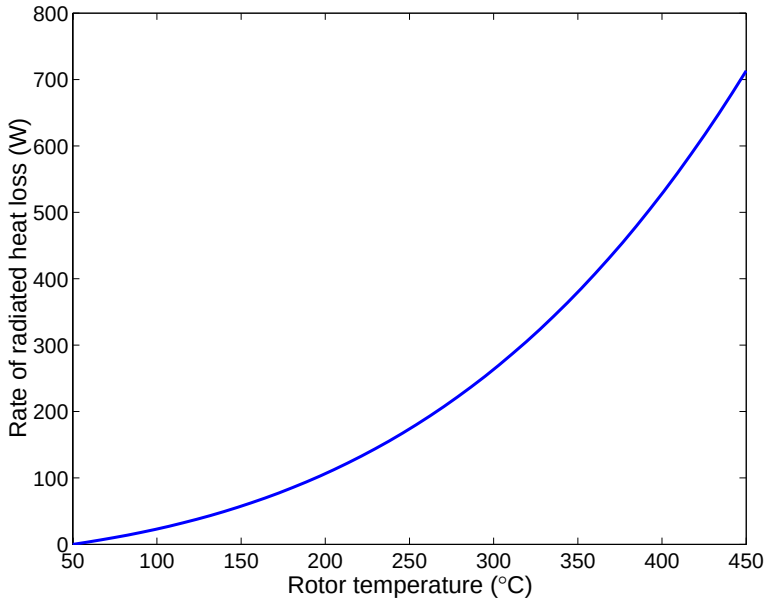


Figure 2.2: Rate of radiated heat loss versus rotor temperature. Stator temperature assumed to be $50°C$.

except at high temperatures, and the thermal path through the bearings is minimal, therefore, controlling the rotor losses is critical to prevent overheating of the rotor. Fig. 2.2 plots the rate of heat loss through radiation versus rotor temperature. This graph was calculated for the prototype rotor, and assumes that the stator temperature remains at $50°C$. From this, it can be seen that even $300W$ of rotor loss (1% of the $30kW$ output power) would lead to a steady-state rotor temperature of $320°C$. This thermal limit on rotor losses rules out machines such as induction machines and switched reluctance machines because of their respective conduction and core losses on the rotor. The remaining motors to consider are permanent magnet and synchronous reluctance.

### 2.2.1 Motor Selection

Permanent magnet (PM) motors are currently the most commonly used motors for fly-wheel systems [5, 18, 40]. While they have the advantages of high efficiency and low rotor losses, the presence of PMs on the rotor makes the rotor more temperature sensitive (thus requiring even

lower rotor losses), and the mechanical structure of the rotor more complicated because of the brittleness and low strength of the PMs. The cost of the PMs, especially the high-temperature Sm-Co type, can also be considerable.

Synchronous reluctance (SR) motors are also used in some flywheel systems. They can also have high efficiency, low rotor losses, and low zero torque spinning losses. Unfortunately, it is difficult to construct a SR rotor with a high $L_d/L_q$ ratio while maintaining a robust rotor structure. Examples of SR rotors constructed using several axially bonded sheets of high strength steel as in [37] and [20] have been made, however this leads to a moderate $L_d/L_q$ ratio which in turn leads to a moderate power factor. Low power factor increases the required VA rating of the drive and can add significantly to the cost of the system.

All three of these motor types, PM, SR, and homopolar inductor, share the advantage of high efficiency, however PM rotors tend to be more temperature sensitive, mechanically complex, and costly; and solid rotor SR motors have either complex rotor structures or low power factors. While these issues can be overcome, homopolar inductor motors present an attractive alternative with a low-cost rotor machined from a single piece of steel that is more robust and less temperature sensitive than PM or SR rotors. In addition, a homopolar inductor motor with a slotless stator and six-step drive eliminates stator slot harmonics and maintains low rotor losses while also allowing operation at unity (or any desired) power factor.

These advantages of robust rotor structure and low rotor losses make homopolar inductor motors particularly well-suited for flywheel energy storage applications.

### 2.2.2 Homopolar Inductor Motors

Although not widely used in practice, homopolar inductor motors have been researched for a variety of applications. They are sometimes referred to as “synchronous homopolar motors”

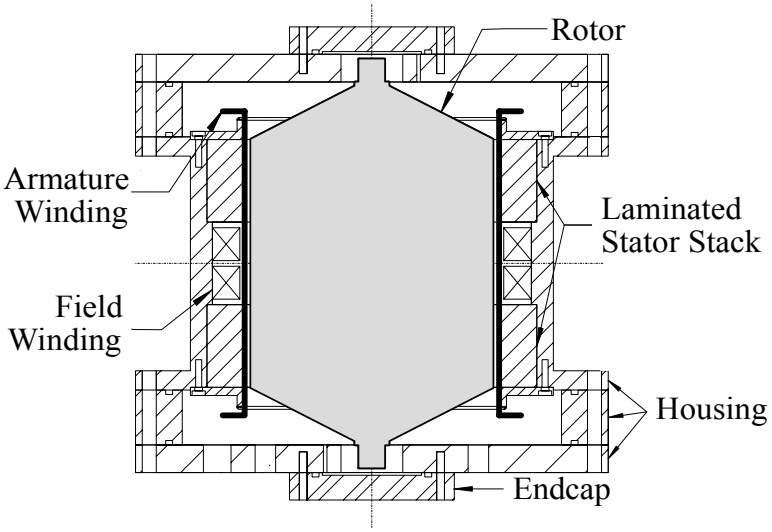


Figure 2.3: Cutaway view of homopolar inductor motor flywheel system.

[17, 38, 34], or “homopolar motors” [31, 21], but “homopolar inductor motor” [14, 35, 33] is also commonly used and will be the term applied in this thesis. The defining feature of these motors is the homopolar d-axis magnetic field created by a field winding [14, 35, 21, 17, 32], permanent magnets, or a combination of permanent magnets and windings [31]. The principle is the same as in a traditional synchronous generator, with which the homopolar inductor motor has similar terminal characteristics. However, in the case of the homopolar inductor motor, the field winding is fixed to the stator and encircles the rotor rather than being placed on the rotor. The field winding and the magnetizing flux path in the present motor design are shown schematically in Fig. 2.4. Note that the rotor pole faces on the upper part of the rotor are offset from the pole faces on the lower part (see Figs. 2.4 and 2.5).

There are several advantages to having the field winding in the stator. Among these are elimination of slip rings and greatly simplified rotor construction, making it practical to construct the rotor from a single piece of high strength steel. This feature makes homopolar motors very

attractive for high-speed operation; a single piece steel rotor is used in the design presented here and in [14, 17, 32]. Other homopolar rotor designs include laminations [21], permanent magnets [31], or other non-magnetic structural elements to increase strength and reduce windage losses [35]. Additional advantages of having the field winding in the stator include ease in cooling the field winding and increased volume available for this winding. The large volume available for the field winding allows high flux levels to be achieved efficiently, making a slotless stator design feasible.

As described previously, the slotless stator is an advantage for solid rotor machines because it eliminates slotting induced rotor losses [20]. A slotless stator also allows for higher gap flux densities because saturation of the stator teeth is no longer a concern. The design principle is similar to a slotless permanent magnet machine, with the advantage that the magnetizing field can be controlled to keep efficiency high at low and zero torque. A possible disadvantage of the slotless stator is the difficulty in constructing the armature winding, which must be bonded to the smooth inner bore of the stator iron. As described in section 7.1, a relatively simple and effective process was developed in this work to construct the winding.

## 2.3 Flywheel Bearings

Flywheels have very demanding requirements for their bearing systems because of the high rotational speeds and operation in a vacuum. Since it is impossible to balance a high-speed rotor so that the center of mass and the bearings' axis of rotation coincide perfectly, it is often preferable to mount the flywheel rotor on compliant bearings. Compliant bearings allow the rotor to translate radially, allowing the axis of rotation to shift, and thus allowing the rotor to spin about the center of mass. This dramatically reduces the forces on the bearings caused by rotor unbalance.

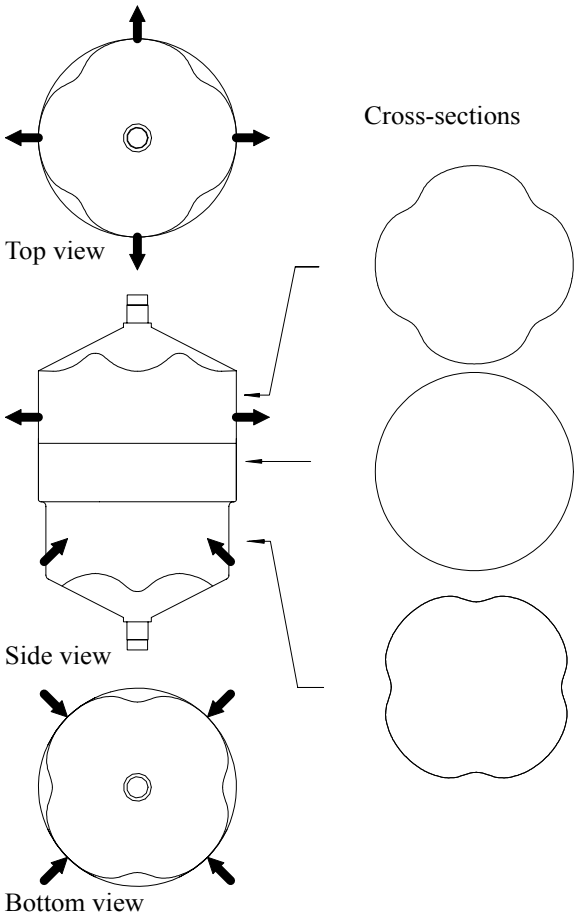


Figure 2.4: Views of rotor. Dark arrows indicate magnetizing flux paths

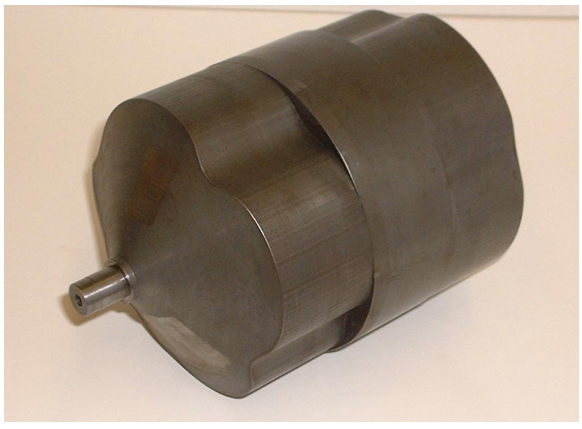

Figure 2.5: Photo of rotor.

Modifying the stiffness of the compliant bearing also alters the speeds at which rotor resonances occur, an important consideration which is discussed in Chapter 4.

Compliant bearings can be achieved either by using a magnetic bearing which levitates the rotor with magnetic fields or conventional ball bearings in a compliant mount. Magnetic bearings have the advantage that they can be controlled electronically, and their stiffness and other performance characteristics can be tuned during operation. They are also vacuum compatible and capable of operating over a very large temperature range. One small disadvantage is that magnetic bearings are larger than conventional bearings, but their primary disadvantages are their cost and complexity.

For this project, a ball bearing system in a compliant mount was chosen over magnetic bearings to minimize the complexity and maintain the focus of the project on the flywheel system design. A compliant mount was constructed by mounting the ball bearing with a tolerance ring wrapped around the outer diameter of the bearing. This construction is detailed in Chapter 7.

Unfortunately, there are several disadvantages inherent to using ball bearings in a flywheel. Although there are standard ball bearings designed for operation at speeds up to 100,000 rpm, their lifetime is reduced by operation in a vacuum. The grease used to lubricate these bearings is not vacuum compatible, and thus it volatizes as the bearings heat up and eventually leads to bearing failure. There are vacuum compatible greases, but they are generally high viscosity or for low temperatures, and unsuitable for this application.

# Chapter 3

# Homopolar Inductor Motors

This chapter presents the model for the homopolar inductor motor used in the design. First the notation and the references frames used are presented, and then a lumped parameter magnetic model of the motor is developed from the motor geometry.

## 3.1 Reference Frames and Notation

Although the field winding in a synchronous generator is located on the rotor and the field winding of a homopolar inductor is located in the stator, both machines share the same terminal characteristics, and therefore can be described with the same lumped parameter inductance model. In addition, even though the goal is to design an 8-pole motor, an equivalent 2-pole motor is modelled by describing the motor in electrical radians. This is done using the relationship:

$$\theta_m = \frac{P}{2}\theta_{ms} \tag{3.1}$$

where $\theta_m$ is the rotor mechanical position in electrical radians, $\theta_{ms}$ is the rotor mechanical position in spatial radians, and the number of poles $P = 8$. The equivalent two-pole synchronous generator used in this design process is diagrammed in Fig. 3.1.

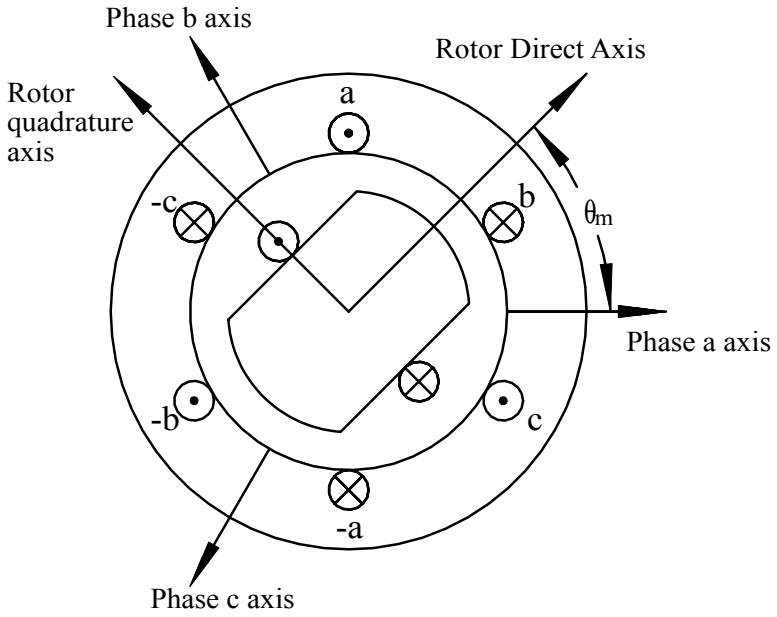


Figure 3.1: Diagram of an equivalent 2-pole synchronous generator in electrical radians.

### 3.1.1 Reference frames

Several reference frames are used in the text. The superscripts $r$, and $v$ indicate variables described by the rotor frame, and voltage frame. The rotor frame rotates synchronously with the rotor at the speed $\omega_m$ and is aligned with the rotor direct axis (d-axis) and quadrature axis (q-axis). The voltage frame rotates synchronously with the stator voltage $\mathbf{V}$ at the speed $\omega_e$ and is aligned with the d-axis and q-axis of the voltage. During steady state the rotor and the voltage frame rotate at the same speed $\omega_e = \omega_m$ and differ by a constant angle $\delta$. In this text, the rotor frame is used in the design of the motor, and the voltage frame is applied in the controller development.

Lack of a superscript indicates variables that are either in the stationary frame oriented with the stator phase $a$ axis, such as $i_a$, or independent of reference frames, such as $i_f$.

| | |
|---|---|
| Angles: | |
| $\theta_m$ | Angle between rotor frame $d$-axis and phase $a$-axis, electrical radians |
| $\theta_{ms}$ | Angle between rotor frame $d$-axis and phase $a$-axis, spatial radians |
| $\theta_e$ | Angle between voltage frame $d$-axis and phase $a$-axis |
| $\omega_m = \dot{\theta}_m$ | Rotor frequency in electrical radians |
| $\omega_e = \dot{\theta}_e$ | Electrical frequency of $v$ in electrical radians |
| $P$ | Number of poles for motor |
| $\mathcal{L}_{aa}$ | Phase inductance of stator phase $a$, |
| $\mathcal{L}_{ab}$ | Mutual inductance between stator phase $a$ and $b$. |
| $v_f, i_f, R_f$ | Voltage, current, and resistance of field winding. |
| $L_{mf}$ | Mutual inductance between field winding and armature phases. |
| $v = [\ v_d \quad v_q\ ]^T$ | Stator voltage vector, 2-phase. |
| $i = [\ i_d \quad i_q\ ]^T$ | Stator current vector, 2-phase. |

Table 3.1: Commonly used variables.

### 3.1.2 Notation

The subscripts d,q, and 0 indicate variables that have been transformed using the Park transform from 3- to 2-phase, as described in Section 3.2.4. The subscripts $a$, $b$, and $c$ indicate 3-phase quantities. The subscript $f$ indicates variables related to the field winding, for which no transformation is applied.

Most of the equations are written with angles expressed in electrical radians. Angles that are written in spatial radians are indicated by a second subscript 's' as in $\theta_{ms}$. Table 3.1 defines the more important variables that will be used throughout the text.

## 3.2 Homopolar Inductor Motor Modeling

This section presents the equations used to evaluate the efficiency of the homopolar inductor motor designs. The equations are developed by first presenting the general lumped parameter model of a 3-phase homopolar inductor motor. Then the inductance parameters for this model are calculated based on the geometry of the motor. Once this relationship between the ge-

ometry of the motor and the lumped parameter model is established, the lumped parameter model is simplified by transforming it from a 3-phase model in the stationary frame to an equivalent 2-phase model in the rotor frame. The motor performance and efficiency equations for this 2-phase model are then presented.

### 3.2.1 Lumped Parameter Model

Following the development in [12], the flux-current relationship in a 3-phase homopolar inductor motor is:

$$\begin{bmatrix} \lambda_a \\ \lambda_b \\ \lambda_c \\ \lambda_f \end{bmatrix} = \begin{bmatrix} \mathcal{L}_{aa} & \mathcal{L}_{ab} & \mathcal{L}_{ac} & \mathcal{L}_{af} \\ \mathcal{L}_{ab} & \mathcal{L}_{bb} & \mathcal{L}_{bc} & \mathcal{L}_{bf} \\ \mathcal{L}_{ac} & \mathcal{L}_{bc} & \mathcal{L}_{cc} & \mathcal{L}_{cf} \\ \mathcal{L}_{af} & \mathcal{L}_{bf} & \mathcal{L}_{cf} & \mathcal{L}_{ff} \end{bmatrix} \begin{bmatrix} i_a \\ i_b \\ i_c \\ i_f \end{bmatrix} \tag{3.2}$$

In this model, the windings are assumed to have sinusoidally distributed winding density. The stator self-inductances are defined with a magnetizing component $L_{aa0}$, a leakage component $L_{al}$, and an angle dependent component $L_{g2}$:

$$\begin{aligned} \mathcal{L}_{aa} &= L_{aa0} + L_{al} + L_{g2}\cos P\theta_{ms} \\ \mathcal{L}_{bb} &= L_{aa0} + L_{al} + L_{g2}\cos P\left(\theta_{ms} - \frac{2\pi}{3}\right) \\ \mathcal{L}_{cc} &= L_{aa0} + L_{al} + L_{g2}\cos P\left(\theta_{ms} + \frac{2\pi}{3}\right) \end{aligned} \tag{3.3}$$

where $\theta_{ms}$ is the rotor angle in spatial radians. The stator-to-stator mutual inductances are defined as:

$$\begin{aligned} \mathcal{L}_{ab} &= -\frac{1}{2}L_{aa0} + L_{g2}\cos P\left(\theta_{ms} - \frac{2\pi}{3}\right) \\ \mathcal{L}_{bc} &= -\frac{1}{2}L_{aa0} + L_{g2}\cos P\theta_{ms} \\ \mathcal{L}_{ac} &= -\frac{1}{2}L_{aa0} + L_{g2}\cos P\left(\theta_{ms} + \frac{2\pi}{3}\right) \end{aligned} \tag{3.4}$$

and the stator-to-field-winding mutual inductances and the field-winding self-inductance are:

$$\begin{aligned}
\mathcal{L}_{af} &= L_{mf}\cos P\theta_{ms} \\
\mathcal{L}_{bf} &= L_{mf}\cos P\left(\theta_{ms}-\frac{2\pi}{3}\right) \\
\mathcal{L}_{cf} &= L_{mf}\cos P\left(\theta_{ms}+\frac{2\pi}{3}\right) \\
\mathcal{L}_{ff} &= L_{ff}
\end{aligned} \tag{3.5}$$

The voltage equations for this motor are then:

$$v_a = Ri_a + \frac{d\lambda_a}{dt} \tag{3.6}$$

$$v_b = Ri_b + \frac{d\lambda_b}{dt} \tag{3.7}$$

$$v_c = Ri_c + \frac{d\lambda_c}{dt} \tag{3.8}$$

$$v_f = R_f i_f + \frac{d\lambda_f}{dt} \tag{3.9}$$

### 3.2.2 Calculating Inductances from Motor Geometry

To use this inductance model in the design of the motor, the relationship between motor geometry and the inductances of Eq. (3.2) must be established. The development in this section follows that of [25], with modifications made to accommodate the differences in stator geometry between a synchronous generator and a homopolar inductor motor. First the self-inductance $\mathcal{L}_{aa}$ will be calculated. The self-inductance of a winding is determined by the amount of flux linked by a winding due to its own current. The turn density of the phase $a$ winding with $N_s$ turns is:

$$N_a(\phi_{ss}) = \frac{N_s}{2}\frac{P}{2}\sin\left(\frac{P}{2}\phi_{ss}\right) \tag{3.10}$$

where $\phi_{ss}$ is the position along the inside of the stator relative to the phase $a$ axis. The $MMF$ due to winding $a$ is the integral of the turn density of phase $a$ and the current $i_a$:

$$MMF_a(\phi_{ss}) = \int_{-\pi/P}^{\phi_{ss}} N_a(\xi) i_a d\xi = -\frac{N_s}{2}\cos\left(\frac{P}{2}\phi_{ss}\right) i_a \tag{3.11}$$

where $\xi$ is a dummy variable of integration. With the rotor MMF defined as zero, and the other currents $i_b$, $i_c$, and $i_f$ also zero, the equation for the flux density $B_a$ in the air gap is:

$$B_a(\phi_{ss}, \phi_{rs}) = -\frac{\mu_0 MMF_a(\phi_{ss})}{g(\phi_{rs})} \tag{3.12}$$

where $g(\phi_{rs})$ is the distance between the inner bore of the stator and the surface of the rotor, as a function of the position along the rotor surface $\phi_{rs}$. This equation for $B_a$ assumes that the flux in the gap is directed radially, ignoring the effects of fringing and leakage flux. The stator and rotor are also assumed to be infinitely permeable. For the initial analysis, it will be assumed that $B_a$ consists of a constant and a sinusoidal component. It turns out that only the fundamental sinusoidal component of flux is linked by the sinusoidal winding. Since the upper and lower stator have the same profile shifted out of phase, the upper and lower gap functions will be of the form:

$$g_u(\phi_{rs}) = \frac{1}{h_1 + h_2 \cos(\frac{P}{2}\phi_{rs})} \tag{3.13}$$

$$g_l(\phi_{rs}) = \frac{1}{h_1 + h_2 \cos(\frac{P}{2}\phi_{rs} + \pi)} \tag{3.14}$$

where $h_1$ and $h_2$ have units of 1/length and are defined as:

$$h_1 = \frac{1}{2g_{min}} + \frac{1}{2g_{max}} \tag{3.15}$$

$$h_2 = \frac{1}{2g_{min}} - \frac{1}{2g_{max}} \tag{3.16}$$

Fig. 3.2 plots the rotor profile for this gap function, and defines $g_{min}$ and $g_{max}$.

We note that the stator angle $\phi_{ss}$ and the rotor surface angle $\phi_{rs}$ are related by the position of the rotor $\theta_{ms}$:

$$\phi_{ss} = \phi_{rs} + \theta_{ms} \tag{3.17}$$

and then plugging in (3.11), (3.13), and (3.17) into (3.12) results in:

$$B_{a,u}(\phi_{ss}, \theta_{ms}) = \mu_0 \frac{N_s}{2} \cos\left(\frac{P}{2}\phi_{ss}\right) \left[h_1 + h_2 \cos\frac{P}{2}(\phi_{ss} - \theta_{ms})\right] i_a \tag{3.18}$$

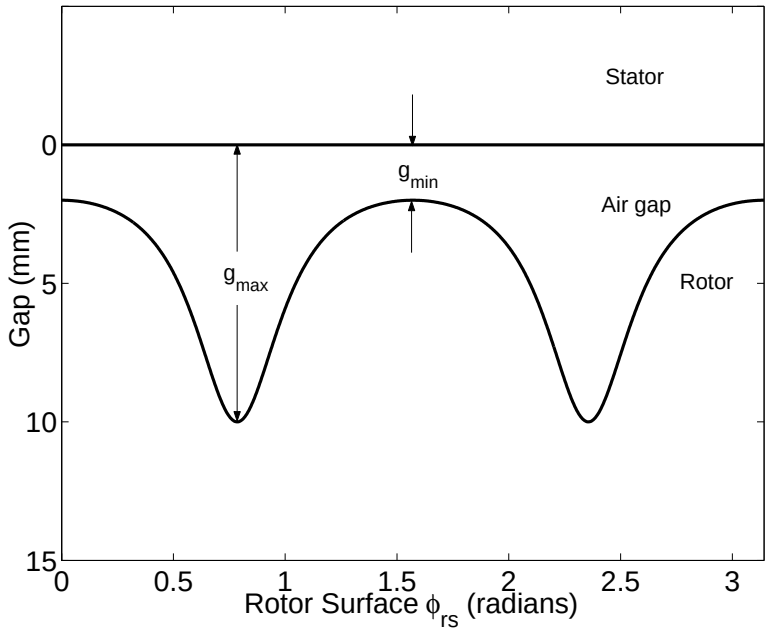


Figure 3.2: Plot of rotor profile with $g_u = \frac{1}{h_1+h_2\cos(\frac{P}{2}\phi_{rs})}$. Here $g_{min} = 2\,\text{mm}$ and $g_{max} = 10\,\text{mm}$. The rotor profile plotted is that of the sinusoidal rotor shown in Fig. 2.4, and is simply the cross-section transformed into a Cartesian coordinate system.

for the upper half of the machine. The lower half of the machine has a similar expression with a phase shift as a result of the phase shifted gap function 3.14. This is the expression for the flux density at position $\phi_{ss}$ along the stator with the rotor turned to position $\theta_{ms}$.

Now, to calculate the flux linkage of the windings, we integrate the winding density and the flux density. First, we define the flux linked by a single turn of the winding. In a $P$-pole motor winding, each turn spans $\frac{2\pi}{P}$ radians. A winding centered about $\phi_{ss}$ spans from $\phi_{ss} - \frac{\pi}{P}$ to $\phi_{ss} + \frac{\pi}{P}$, and the flux that it links when the rotor is turned to position $\theta_{ms}$ and flux density $B_a$ is generated is:

$$\Phi_{a,u}(\phi_{ss}, \theta_{ms}) = rh \int_{\phi_{ss}-\frac{\pi}{P}}^{\phi_{ss}+\frac{\pi}{P}} B_{a,u}(\xi, \theta_{ms}) d\xi \tag{3.19}$$

where $r$ is the inner radius of the stator, and $h$ is the height of the stack.

The flux linkage of the winding $a$ with the flux of the upper stator is then:

$$\lambda_{aa,u}(\theta_{ms}) = \frac{P}{2}\int_{\frac{-\pi}{P}}^{\frac{\pi}{P}} N_a(\phi_{ss}+\frac{\pi}{P})\,\Phi_{a,u}(\phi_{ss},\theta_{ms})d\phi_{ss} \tag{3.20}$$

In the above equation, we are integrating over an interval $\frac{2\pi}{P}$ long, and multiplying by $\frac{P}{2}$ to get the contribution of the entire winding. Setting up the limits of integration in this manner ensures that the flux linkage of each winding is only integrated once. Note that the angle for the winding density $N_a$ is offset from $\phi_{ss}$ by $\frac{\pi}{P}$ because this the winding density for the turns that span an area *centered* about $\phi_{ss}$, not the turns that are located at $\phi_{ss}$.

In the homopolar inductor motor, the stator and rotor are split into upper, middle, and lower parts, while the stator winding is uniform over the length of the stator. Therefore, the *North* flux linked by winding $a$ in the upper stator is partially offset by the *South* flux of the lower stator which also travels through the winding. The total flux linkage is then:

$$\lambda_{aa}(\theta_{ms}) \quad = \quad \lambda_{aa,u}(\theta_{ms}) + \lambda_{aa,l}(\theta_{ms}) \tag{3.21}$$

where $\lambda_{aa,u}$ and $\lambda_{aa,l}$ are the flux linkages of the upper and lower parts of winding $a$. These flux linkages are then calculated by performing a double integral of the turn density $N_a$ with the upper flux density $B_{a,u}$, and substituting equations (3.10) and (3.18).

$$\begin{aligned}
\lambda_{aa,u}(\theta_{ms}) &= \int_{-\pi/P}^{\pi/P} N_a(\phi_{ss}+\frac{\pi}{P})\Phi_{a,u}(\phi_{ss},\theta_{ms})d\phi_{ss} && (3.22)\\
&= \int_{-\pi/P}^{\pi/P} N_a(\phi_{ss}+\frac{\pi}{P})rh\int_{\phi_{ss}-\frac{\pi}{P}}^{\phi_{ss}+\frac{\pi}{P}} B_{a,u}(\xi,\theta_{ms})\,d\xi\,d\phi_{ss} && (3.23)\\
&= \int_{-\pi/P}^{\pi/P} \frac{N_s}{2}\sin\phi_{ss} i_a\cdot && (3.24)\\
&\quad rh\int_{\phi_{ss}-\frac{\pi}{P}}^{\phi_{ss}+\frac{\pi}{P}} \mu_0\frac{N_s}{2}\cos\xi\left[h_1+h_2\cos\frac{P}{2}(\xi-\theta_{ms})\right]d\xi\,d\phi_{ss} && (3.25)
\end{aligned}$$

The double integral sums up the flux linked by all the turns in the winding of phase $a$. Performing

the integral in (3.25) and following the same process for $\lambda_{aa,l}$ results in:

$$\lambda_{aa,u} = \left(\frac{N_s}{2}\right)^2 \pi\mu_o rh\left(h_1 + h_2\cos\frac{P}{2}\theta_m\right) i_a \tag{3.26}$$

$$\lambda_{aa,l} = \left(\frac{N_s}{2}\right)^2 \pi\mu_o rh\left(h_1 - h_2\cos\frac{P}{2}\theta_m\right) i_a \tag{3.27}$$

$$\lambda_{aa} = 2\left(\frac{N_s}{2}\right)^2 \pi\mu_o rhh_1 i_a \tag{3.28}$$

Where $r$ and $h$ are the radius and height of a stator stack. Using $\lambda_{aa} = \mathcal{L}_{aa} i_a$, and dividing by $i_a$ results in:

$$\mathcal{L}_{aa} = L_{aa0} - L_{g2}\cos 2\theta_m \tag{3.29}$$

$$L_{aa0} = 2\left(\frac{N_s}{2}\right)^2 \pi\mu_o rhh_1 \tag{3.30}$$

$$L_{g2} = 0 \tag{3.31}$$

Here, the rotor angle dependent component $L_{g2}$ is zero. This is because the variations in the flux linkage of the upper and lower profiles cancel each other out, resulting in a non-salient rotor. This is not always the case, however, since there are many profiles that result in a salient rotor.

The leakage flux was not considered in the above analysis because of the assumption made in equation 3.12, therefore it does not appear in 3.29. Since the leakage flux is a 3-dimensional effect associated with endturns, $L_{al}$ is difficult to calculate analytically, but is generally estimated to be between 5% and 10% of the total inductance. Since it does not have a large effect on the machine performance, a more accurate calculation is not considered in the initial design. Refinements to the initial design are made later using 2-d finite-element analysis (FEA) which includes some 2-d fringing flux effects for a more accurate calculation of the flux linkages.

With the components $L_{aa0}$ and $L_{g2}$ known, inductances $\mathcal{L}_{aa}$, $\mathcal{L}_{bb}$, $\mathcal{L}_{cc}$, $\mathcal{L}_{ab}$, $\mathcal{L}_{bc}$, and $\mathcal{L}_{ac}$ can all be calculated as specified in Eqs. 3.3 and 3.4. A similar process is used to calculate

the mutual inductance terms $L_{mf}$ and $L_{ff}$, with the main difference being to change the winding densities used in equation (3.25) to match those of the field winding. The results are:

$$L_{mf} = 8\left(\frac{N_s N_f}{4}\right)\mu_o rhh_1 \tag{3.32}$$

$$L_{ff} = 2\left(\frac{N_f}{2}\right)^2 \pi^2 \mu_o rhh_1 \tag{3.33}$$

which can then be used in the calculation of $\mathcal{L}_{af}$, $\mathcal{L}_{bf}$, $\mathcal{L}_{cf}$, and $\mathcal{L}_{ff}$.

### 3.2.3 Square-Cut Rotor Profile

Two different rotor designs with different gap profiles $g(\phi_{rs})$ were considered for our prototype. The first rotor profile shown in Fig. 3.2 created a sinusoidal flux density on the $MMF$ when the field winding is excited, while the second "square-cut" rotor produces more of a square-wave $MMF$ when the field winding is excited. A plot of the functions $g(\phi_{rs})$ for the square-cut rotor is shown in Fig. 3.3. Also indicated in the figure is $\alpha$, which when varied from $\frac{\pi}{4}$ creates a salient rotor.

The inductance components differ for the square-cut rotor geometry, and are:

$$L_{aa0} = \mu_0 \pi \left(\frac{N_s}{2}\right)^2 \left(\frac{\alpha_1}{g_{min}} + \frac{2-\alpha_1}{g_{max}}\right) rh \tag{3.34}$$

$$L_{g2} = \mu_0 \sin(\pi\alpha_1) \left(\frac{N_s}{2}\right)^2 \left(\frac{1}{g_{min}} - \frac{1}{g_{max}}\right) rh \tag{3.35}$$

$$L_{mf} = \mu_0 N_f N_s \sin\left(\frac{\pi}{2}\alpha_1\right) \left(\frac{1}{g_{min}} - \frac{1}{g_{max}}\right) rh \tag{3.36}$$

$$L_{ff} = \frac{\mu_0 N_f^2}{2} \left(\frac{\alpha_1}{g_{min}} + \frac{2-\alpha_1}{g_{max}}\right) rh \tag{3.37}$$

where:

$$\alpha_1 = \alpha \frac{4}{\pi} \tag{3.38}$$

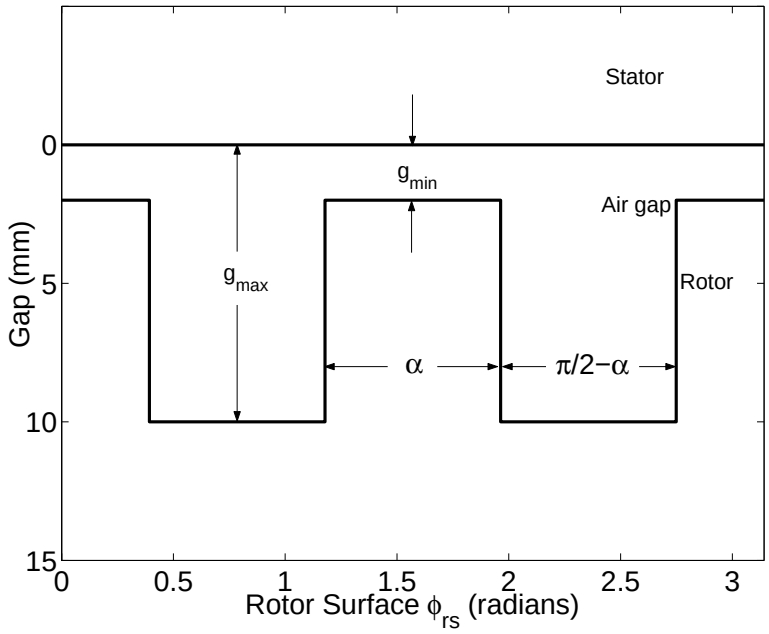


Figure 3.3: Rotor profile for square-cut rotor.

### 3.2.4 2-phase Motor Model

Now that the components of the 3-phase model presented in section 3.2.1 can be calculated from the rotor geometry, the 3-phase model is transformed into a 2-phase motor model in the rotor frame to simplify the expressions. First, the motor model is converted from the 8-pole motor model in spatial radians in Eqns. 3.2 - 3.5 to an equivalent 2-pole motor model in electrical radians by substituting $\theta_{ms}$ with $\frac{2}{P}\theta_m$. The $dq0$ transform then is used to convert 3-phase variables in the stationary reference frame into 2-phase variables. The 2-phase variables may be stationary or in one of the moving rotor or voltage frames, depending on whether a rotating or constant angle $\alpha$ is

used in the transform. As presented in [12, 19], the transform is:

$$\begin{bmatrix} S_d \\ S_q \\ S_0 \end{bmatrix} = \frac{2}{3} \begin{bmatrix} \cos\alpha & \cos(\alpha - \frac{2\pi}{3}) & \cos(\alpha + \frac{2\pi}{3}) \\ -\sin\alpha & -\sin(\alpha - \frac{2\pi}{3}) & -\sin(\alpha + \frac{2\pi}{3}) \\ \frac{1}{2} & \frac{1}{2} & \frac{1}{2} \end{bmatrix} \begin{bmatrix} S_a \\ S_b \\ S_c \end{bmatrix} \tag{3.39}$$

$$S_{dq0} = T(\alpha) S_{abc} \tag{3.40}$$

The inverse is:

$$\begin{bmatrix} S_a \\ S_b \\ S_c \end{bmatrix} = \begin{bmatrix} \cos\alpha & -\sin\alpha & 1 \\ \cos(\alpha - \frac{2\pi}{3}) & -\sin(\alpha - \frac{2\pi}{3}) & 1 \\ \cos(\alpha + \frac{2\pi}{3}) & -\sin(\alpha + \frac{2\pi}{3}) & 1 \end{bmatrix} \begin{bmatrix} S_d \\ S_q \\ S_0 \end{bmatrix} \tag{3.41}$$

$$S_{abc} = T^{-1}(\alpha) S_{dq0} \tag{3.42}$$

In Eqs. 3.39 and 3.41, the subscripted $S$ represents a component of a vector variable such as $v$, $\lambda$ or $i$, and in Eqs. 3.40 and 3.42 the subscripted $S$ represents the vector variable itself.

To transform the 3-phase flux-linkages in the stationary frame into the rotor frame at angle $\theta_m$, the inductances of equation 3.2 are partitioned into:

$$\lambda_{abc} = \mathcal{L}_{abc} i_{abc} + \mathcal{L}_{mf} i_f \tag{3.43}$$

$$\lambda_f = \mathcal{L}_{mf}^T i_{abc} + \mathcal{L}_{ff} i_f \tag{3.44}$$

Using:

$$\lambda_{dq0} = T(\theta_m) \lambda_{abc} \tag{3.45}$$

$$i_{dq0} = T(\theta_m) i_{abc} \tag{3.46}$$

we obtain:

$$\lambda_{dq0} = T(\theta_m)\mathcal{L}_{abc}T(\theta_m)^{-1}i_{dq0} + T(\theta_m)\mathcal{L}_{mf}i_f \tag{3.47}$$

$$\lambda_f = \mathcal{L}_{mf}^T T(\theta_m)^{-1}i_{dq0} + \mathcal{L}_{ff}i_f \tag{3.48}$$

The 2-phase inductances are then:

$$\mathcal{L}_{dq0} = T\mathcal{L}_{abc}T^{-1} \tag{3.49}$$

$$= \begin{bmatrix} L_d & 0 & 0 \\ 0 & L_q & 0 \\ 0 & 0 & L_0 \end{bmatrix} \tag{3.50}$$

$$\mathcal{L}_{mf2a} = T\mathcal{L}_{mf} \tag{3.51}$$

$$= \begin{bmatrix} L_{mf} \\ 0 \\ 0 \end{bmatrix} \tag{3.52}$$

$$\mathcal{L}_{mf2b} = \mathcal{L}_{mf}^T T^{-1} \tag{3.53}$$

$$= \frac{3}{2}\begin{bmatrix} L_{mf} & 0 & 0 \end{bmatrix} \tag{3.54}$$

where:

$$L_d = L_{al} + \frac{3}{2}\left(L_{aa0} + L_{g2}\right) \tag{3.55}$$

$$L_q = L_{al} + \frac{3}{2}\left(L_{aa0} - L_{g2}\right) \tag{3.56}$$

$$L_0 = L_{al} \tag{3.57}$$

In 2-phase variables, the inductances are no longer dependent on rotor position, which greatly simplifies the flux-linkage relationships.

The voltage equations are then:

$$v_d = Ri_d + \frac{d\lambda_d}{dt} - \omega\lambda_q \tag{3.58}$$

$$v_q = Ri_q + \frac{d\lambda_q}{dt} + \omega\lambda_d \tag{3.59}$$

$$v_0 = Ri_0 + \frac{d\lambda_0}{dt} \tag{3.60}$$

$$v_f = R_f i_f + \frac{d\lambda_f}{dt} \tag{3.61}$$

The zero-sequence terms, $i_0$ and $v_0$, are only present when dealing with unbalanced conditions. Since these are not analyzed in this thesis, they will be omitted. For the purposes of the design, the machine was assumed to be operating at steady state, i.e. constant speed, current, and flux linkages $\lambda$, therefore the $\frac{d\lambda}{dt}$ terms are dropped from the voltage equations. The relevant equations then simplify to:

$$v_d = Ri_d - \omega_m(L_q i_q) \tag{3.62}$$

$$v_q = Ri_q + \omega_m(L_d i_d + L_{mf} i_f) \tag{3.63}$$

$$v_f = Ri_f \tag{3.64}$$

The torque and power equations for this 2-phase motor model are:

$$T_{ms} = \frac{3}{2}\frac{poles}{2}\left(\lambda_d i_q - \lambda_q i_d\right) \tag{3.65}$$

$$= \frac{3}{2}\frac{poles}{2}\left[(L_d i_d + L_{mf} i_f) i_q - L_q i_q i_d\right] \tag{3.66}$$

$$P = T_{ms}\omega_{ms} \tag{3.67}$$

Thus, only equations (3.62) through (3.67) are necessary for evaluating the steady-state operating points of a homopolar inductor motor. The output power of a given motor design for a given current $i$ can be evaluated from the inductance parameters $L_d$, $L_q$, and $L_{mf}$, which are calculated directly from the motor geometry, as described in section 3.2.2.

### 3.2.5 Motor Losses

The expression for the stator armature copper losses $P_{cu}$ is:

$$P_{cu} = i_s^2 R \tag{3.68}$$

The losses for the three-phase inverter used to drive the armature windings is modelled as a constant voltage drop $V_{inv}$:

$$P_{inv} = |i_s| V_{inv} \tag{3.69}$$

A dc-dc converter is used to drive the current in the field winding. The total power consumed by the losses in the dc-dc converter and the copper loss in the field winding is:

$$P_{dc-dc} = \frac{i_f^2 R_f}{\eta} \tag{3.70}$$

where the dc-dc converter losses are assumed to be proportional to its output power. The efficiency of the dc-dc converter $\eta$ was assumed to be equal to $0.75$ for the design process.

The core losses are calculated from loss data provided by the manufacturers of the core material. For Arnon 5 laminations, a power law equation [39] model of the form:

$$P_{core} = K_1 |\boldsymbol{\lambda}|^{K_2} f^{K_3} \cdot m_s \tag{3.71}$$

where $m_s$ is the mass of the stator core, was fit to the manufacturers data.

### 3.2.6 Efficiency calculation

For motors, the efficiency is usually measured as the mechanical output power divided by the electrical input power. For generators, it is usually reversed, and calculated as electrical output power divided by mechanical input power. However, in the case of a motor/generator used in a flywheel energy storage system, the mechanical power is not an input or output quantity.

Therefore, a more relevant efficiency measure for our flywheel design is to calculate efficiency as the fraction of the electrical input or output power that is *not* losses:

$$\eta = 1 - \frac{P_{loss}}{|P_e|} \tag{3.72}$$

The advantage of this formulation for efficiency is that it is consistent for both motoring and generating modes, does not require measuring or calculating mechanical power, and is more aligned with what is important for a flywheel energy storage system, namely, the ability to sink and source electrical power with low losses.

With the exception of methods for calculating losses due to harmonics, all the expressions necessary for calculating the efficiency of a homopolar inductor motor from a specified geometry have been presented.

# Chapter 4

# Design Optimization

## 4.1 Flywheel Design Process

This section describes the steps used in the design of the flywheel energy storage system. The rotor design process is discussed, and then the optimization process for the stator and the selection of bearing stiffness are presented.

### 4.1.1 Rotor Design

#### Rotor Material Selection

The first step in the design process was the selection of the material for the rotor. Since an integrated flywheel configuration had been chosen, the desired rotor material would have to be magnetically permeable and have a high strength-to-weight ratio. These two requirements limit the choices to one of a number of high strength steel alloys, such as AerMet 100, AF1410, H11, 300M, Maraging 250, and AISI 4340. These are all different alloys of steel that can be hardened to ultimate strengths in excess of $290ksi$, and they are generally used in very demanding aerospace applications, such as aircraft landing gear. Since the ultimate strength for the alloys is similar, the

chief differentiators are their fatigue properties and fracture toughness, which are documented in [10].

Ultimately, 300M alloy steel was selected for the rotor. The low alloy steel 300M is very similar to AISI 4340 in composition and can be hardened to an ultimate strength of $2.0GPa$ $(290ksi)$ and has a fatigue strength of $1.0GPa$ ($145ksi$) for over 1 million cycles [1]. It was chosen because of its high strength, availability, and relatively low cost.

**Rotor Volume**

The next step was to calculate the necessary rotor volume to achieve the goal of $500kJ$ $(140W \cdot hr)$ of energy storage. Although the rotor has poles cut into the upper and lower parts, the moment-of-inertia is only smaller than that of a cylinder by less than 10%, depending on the exact rotor profile and length of the pole areas. Therefore, in estimating the rotor dimensions it is appropriate to assume that the rotor is cylindrical. The energy storage capacity of a rotating cylinder is determined from the ultimate strength $\sigma_u$ of the rotor material with this expression [13]:

$$E_{stored} = K \cdot \sigma_u \cdot Vol_r \tag{4.1}$$

A safety margin of $0.5$ for the ultimate strength, a shape factor of $0.60$, and a speed range factor of $\frac{3}{4}$ were incorporated into the constant $K$. The speed range factor accounts for the 2:1 speed range from $\frac{1}{2}\omega_{max}$ to $\omega_{max}$, which implies that $\frac{3}{4}$ of the maximum kinetic energy is recovered. Using these factors in Eq. 4.1, the volume of rotor necessary to meet the energy storage goal was determined to be $1,100cm^3$.

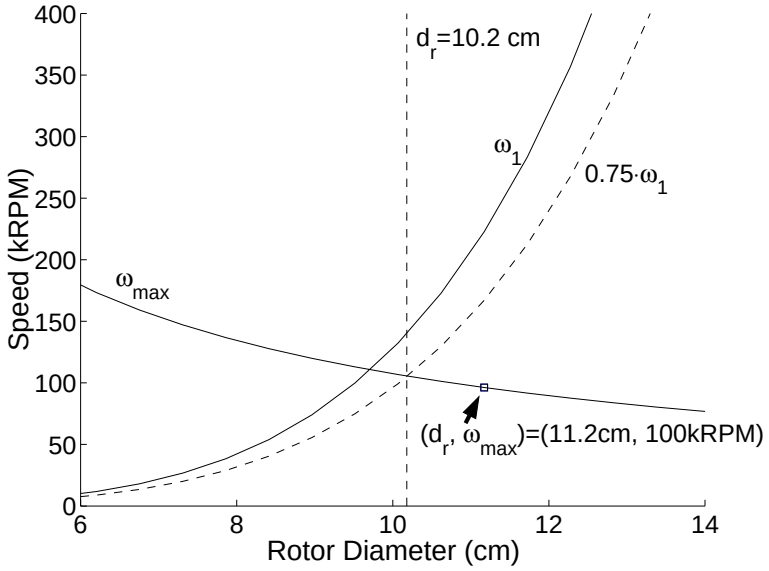


Figure 4.1: Plot of rotor maximum speed and bending modes. The square denotes the diameter of the prototype rotor, and the vertical dashed line indicates the minimum diameter rotor.

**Rotor Shape**

Now that the necessary rotor volume has been determined, the next step was to choose the basic dimensions of the rotor. The choice varies between rotors that are long with a small radius to ones that are short with a large radius. The range of appropriate shapes is narrowed by examining the first bending modes. Fig. 4.1 plots the maximum speed $\omega_{max}$ needed to obtain $500kJ$ of energy storage and the first bending mode $\omega_1$ for a range of rotor diameters. The data is calculated for rotors constructed out of 300M steel with a volume equal to the previously calculated $1,100cm^3$. The dashed line in the figure indicates $0.75\omega_1$, the desired margin of safety for the operating speed. From Fig. 4.1, it can be determined that to achieve $500kJ$ of energy storage in a rotor with a diameter less than $10.2cm$ would require operating near or above the first bending mode, which is undesirable because it could cause large amplitude vibrations, which in turn may require dampers or other devices to control their amplitude.

There is an additional bending mode that occurs in 'pancake' shaped rotors (rotors that have a short axial length and a large diameter). This additional bending mode puts an upper limit on acceptable rotor diameters, however, since it does not affect the outcome of the design optimization, it is omitted from Fig. 4.1.

### 4.1.2 Design Optimization

Using the above criteria, a range of rotors was selected and an optimization was conducted to find the best stator design for each rotor. The goal of the optimization was to find, given a rotor of a particular aspect ratio, the best stator design, rotor design, and operating point to minimize losses at the worst-case full-power operation. The worst-case full-power operating point occurs at peak power at the minimum speed, in this case, 30 kW at a speed of $\frac{1}{2}\omega_{max}$. For a given rotor aspect ratio, the parameters varied are shown in Table 4.1, and include the magnetic gap $g$, armature and field winding dimensions, rotor saliency, and operating point values. The constraints on the optimization included maximum stator volume (set as a multiple of the rotor volume), saturation flux of 1.5 T in the stator, and minimum air gap to ensure adequate mechanical clearances. The efficiency was evaluated using lumped parameter calculations of the magnetic paths and inductances, conduction losses, and core losses. The optimization was implemented in MATLAB using the 'fmincon' constrained gradient minimization algorithm in the MATLAB Optimization toolbox. The optimized parameters and the results are described in Table 4.1.

The results of the optimization are plotted in Fig. 4.2. The shorter, larger radius rotors tended to have lower efficiency primarily because the field winding encircles a wider rotor. The efficiency of the very long, smaller diameter rotors decreases because a flux limit imposed by the saturation of the middle section of the rotor is reached. The optimization suggests that highest efficiency machine that still operates below the first bending mode speed would have a rotor diam-

Table 4.1: Optimization results

| **Parameter** | **Prototype Value** |
|---|---|
| Unoptimized (Given) parameters | |
| Rotor diameter $d_r$ | 11.2 cm |
| Rotor length $l_r$ | 11.5 cm |
| Rotor volume $Vol_r$ | $1,100$ cm$^3$ |
| Rotor mass | 9.5 kg |
| Rotor inertia | $0.0133$ kg/m$^2$ |
| Stator Material | 0.005" SiFe lams |
| Housing Vol. | $10,650$ cm$^3$ |
| Housing Dimensions | 22 cm $\times$ 22 cm $\times$22 cm |
| Optimized parameters | |
| **Stator geometry** | |
| Magnetic gap $g$ | 0.216 cm |
| Armature winding thickness $t_{arm}$ | 0.130 cm |
| Field winding inner dia. $id_{fw}$ | 11.5 cm |
| Outer dia. $od_{fw}$ | 15 cm |
| Height $l_{fw}$ | 3.8 cm |
| **Rotor Geometry** | |
| $L_d/L_q$ ratio | 1 |
| **Operating point** | |
| Field winding current $i_f$ | 11.5 A |
| Armature current $i$ | 96 A |
| Power factor $pf$ | 0.996 |
| Voltage $v$ | 208 V |
| Resulting parameters | |
| $L = L_d = L_q$ | 13 $\mu$H |
| $L_{mf}$ | 1.35 mH |
| Efficiency @ 50 krpm, 30 kW | $95\%$ |

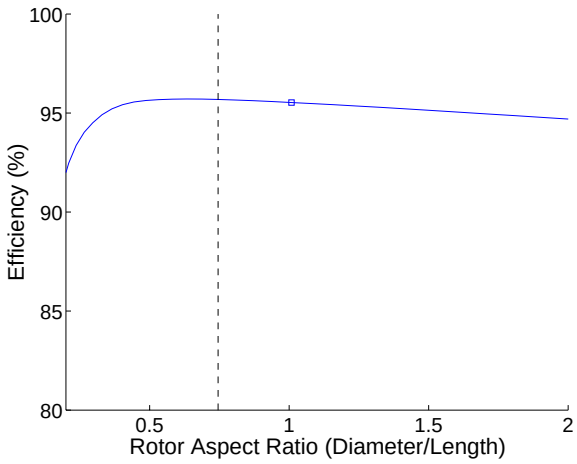


Figure 4.2: Plot of simulated machine efficiency as a function of rotor diameter. The square indicates the rotor diameter of the prototype, and the vertical dashed line matches that of Fig. 4.1.

eter of $10.2cm$. Because of practical considerations related to construction of the prototype, such as available Litz wire sizes, the dimensions of the prototype differed slightly from the optimum as determined by the design process. The values in Table 4.1 are those of the prototype.

The parameter that had the most important effect on performance was the magnetic gap $g$, which is defined as the distance between the outer diameter of the rotor and the inner diameter of the stator laminations. In the efficiency optimization, increasing $g$ had the effect of increasing the volume for the armature windings, thus decreasing stator resistance while increasing the field winding excitation necessary to achieve a certain flux level. In essence, varying $g$ trades off the torque-producing efficiency of the armature for the torque producing efficiency of the field winding.

Fig. 4.3 plots how the optimal gap and the three main loss components vary as a function of the rotor aspect ratio. From the second graph, it can be seen that the field winding loss increases as the rotor diameter increases. This is because the larger rotor diameter increases the length of the field winding and thus its resistance.

The armature loss is the dominant loss, and it is kept relatively constant by the optimization over aspect ratios between 0.45 to 2. At aspect ratios below 0.45, the axial rotor flux constraint is reached, which restricts the field winding excitation from being increased further, and the optimization is forced to increase the armature current (and losses) to reach the given output power.

The core loss remains a relatively small fraction of the loss throughout, and thus it does not have a large impact on the optimization.

Adjustment of the gap dimension also allows for adjustment of the power rating of the machine. Larger gaps admit more armature copper and correspondingly higher armature currents, at the cost of increased field excitation requirements. Thus, the rating of this type of machine can easily be adjusted for a specific target power. The parameters indicated in Tables 2.1 and 4.1 reflect a possible rating for application in hybrid electric vehicles and power quality.

### 4.1.3 Rotor Resonances

The final consideration is to ensure that there are no rotor resonances in the target operating speed range. Since the rotor is to be mounted in a compliant bearing mount, the rotor resonances can be adjusted by modifying the stiffness of the compliant bearing mount. Since by design the rotor will be operating below the first bending mode $\omega_1$, the resonances of concern arise from the rigid-body translational frequencies $\omega_{r1}$ and $\omega_{r2}$ and angular frequencies $\omega_{r1}$ and $\omega_{r4}$ that arise from supporting the rotor on compliant bearings. In this flywheel, the rotor is symmetric about the shaft center, therefore the symmetric rotor model developed in [24] can be used to determine the resonant speeds. Since the stiffness of both bearings mounts are identical and

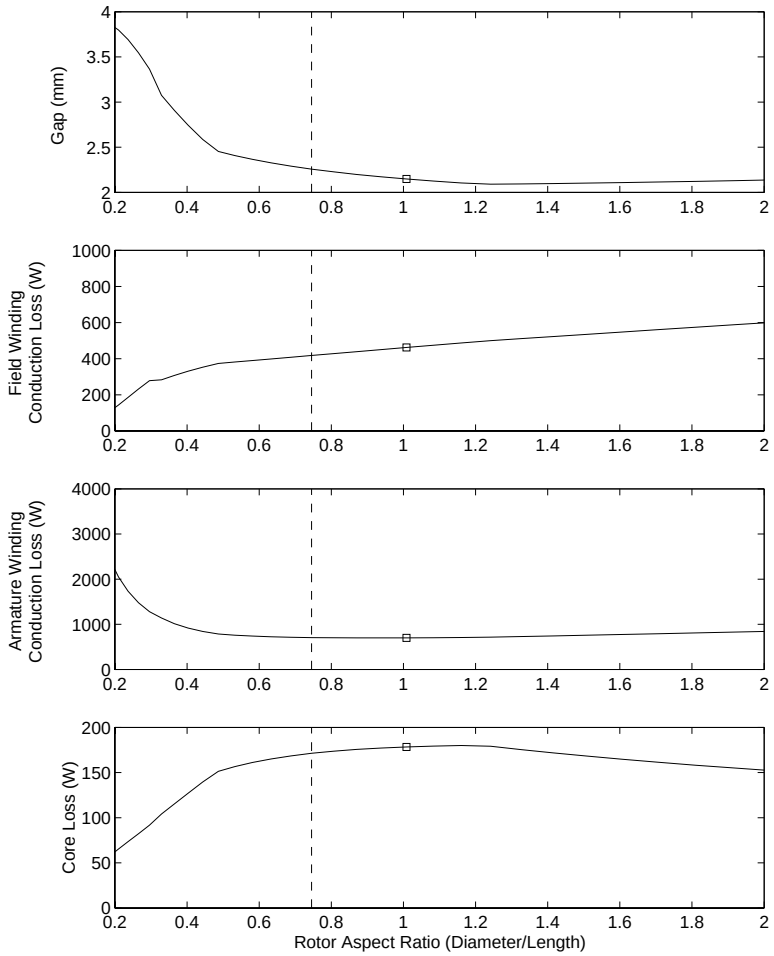


Figure 4.3: Plots of optimized gap, armature conduction loss, field winding conduction loss, and core loss as a function of rotor aspect ratio. The square indicates the rotor diameter of the prototype, and the vertical dashed line indicates the minimum aspect ratio for an appropriate bending mode, as indicated in Fig. 4.1.

isotropic (the same stiffness in the x- and y-axes), $\omega_{r1}$ and $\omega_{r2}$ are equal and determined by:

$$\omega_{r1} = \omega_{r2} = \sqrt{\frac{2k_{bear}}{m_r}} \tag{4.2}$$

where $k_{bear}$ is the stiffness of one bearing mount and $m_r$ the mass of the rotor.

The angular frequencies are a function of the operating speed and the polar and diametral moments of inertia:

$$I_p = \frac{m_r}{2}\frac{d_r^2}{4} \tag{4.3}$$

$$I_d = \frac{m_r}{4}\left(\frac{d_r^2}{4} + \frac{1}{3}l_r^2\right) \tag{4.4}$$

The angular frequencies are then determined by:

$$\omega_{r3}, \omega_{r4} = \frac{1}{2}\frac{I_p}{I_d}\Omega \mp \sqrt{\left(\frac{1}{2}\frac{I_p}{I_d}\Omega\right)^2 + \omega_{30}^2} \tag{4.5}$$

where $\Omega$ is the rotational speed of the rotor, and $\omega_{30}$ is defined as:

$$\omega_{30} = \sqrt{\frac{2k_{bear}l_r^2}{4I_d}} \tag{4.6}$$

Fig. 4.4 plots these natural frequencies as a function of $\Omega$ for $k_{bear} = 75.8 \times 10^6 N/m$ and the resonances which occur when the natural frequencies intersects with $\Omega$. From this plot it can be seen that the all three of these resonance speeds fall outside the target operating speed range of $50krpm - 100krpm$.

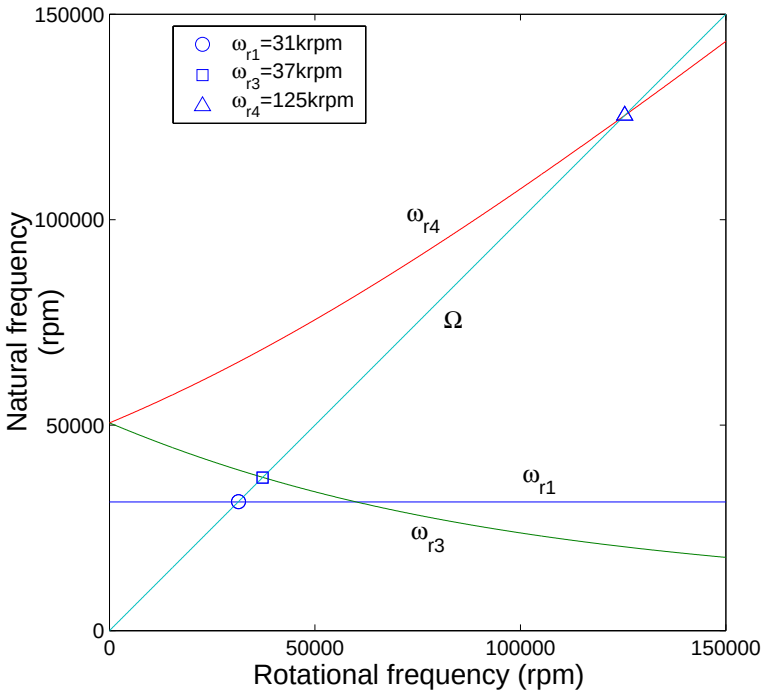


Figure 4.4: Plot of translational and angular resonances for prototype rotor dimensions.

# Chapter 5

# Six-step Drive and Control

## 5.1 Six-step Drive Strategy

The high synchronous electrical frequencies of this motor are partially due to the fact that it is an 8-pole design. Although the high electrical frequency increases the demands on the inverter, having a high pole number also reduces the size of the stator iron and thus the overall weight. In this sense, a high frequency drive enables us to design a more compact flywheel. For this flywheel system, the peak electrical frequency (6.6 kHz at 100 krpm) makes a standard PWM drive scheme with IGBTs impractical. Drive efficiency is also a concern; we wish to minimize switching loss in the inverter, conduction loss in both the inverter and the machine, and core loss in the machine.

In consideration of the above issues, two distinct but related choices were made. The first decision was to use six-step drive operating from a fixed voltage dc bus. The second decision was to drive the inverter at unity power factor. The reasons and consequences for both of these decisions on the inverter and the motor are described in this section.

For the inverter, the obvious benefit of six-step operation is that switching losses are

considerably lower than for PWM, since the maximum switching frequency for any one switching element is the machine's electrical frequency, in this case between 3.3 kHz and 6.6 kHz. This frequency is relatively low for modern IGBT technology. Operation at unity power factor minimizes the inverter current for a given power level, resulting in the most efficient use of the inverter $VA$ rating. In addition, zero-current switching (ZCS) occurs for six-step drives when operating at unity power factor. This is in contrast to PWM which has neither ZCS nor zero-voltage switching (ZVS).

For the motor, it is first noted that high efficiency can be maintained at full power over the entire 2:1 speed range while running with a fixed voltage. This is possible for homopolar inductor motors because of the capability to adjust the back-emf with the field winding. Secondly, operating at unity power factor has little impact on efficiency because in the design presented here it is very close to the optimal operating point. With respect to minimizing motor losses, the optimal angle for the current $i$ as determined from the optimization process described in section 4.1.2 would be aligned with the back-emf $E$ (see right drawing in Fig. 5.1), but $\theta_m$ is less than $5^\circ$ at full power, and even smaller at lower power levels. Therefore, aligning $i$ with $v$ as in the left drawing of Fig. 5.1, represents only a small shift in the operating point, and therefore only a small impact on efficiency.

The last consideration for the motor is losses from harmonics in the six-step waveform. Since the six-step drive precludes all triple-n harmonics with an open neutral connection, the main time harmonics seen by the machine are the fifth and seventh ($6k \pm 1$) harmonics and the core loss should not be significantly higher than that of a sinusoidal drive. As noted in [8, 7], six-step waveforms result in lower core losses than PWM, and only slightly higher core losses than sinusoidal waveforms in induction machine drives, and those results should also carry over to the

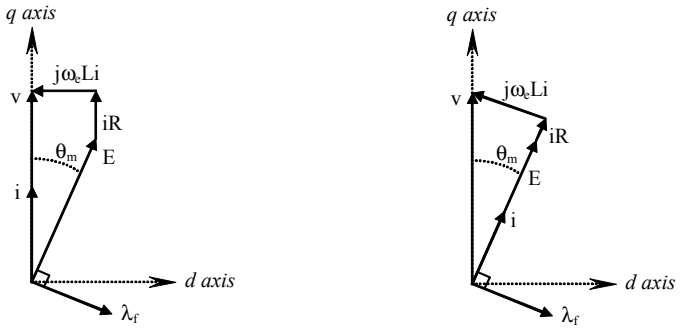


Figure 5.1: Motor vector diagrams with inverter operating at unity power factor (left), and motor operating at its optimal operating point right)

stator core losses in the homopolar inductor machine discussed here. In Chapter 6, it is shown that with proper sizing of the armature phase inductance $L_a$, the harmonic conduction and rotor losses can also be made small. For the 50 krpm-100 krpm speed range with voltage $V = 160V$, an armature inductance of $L_a = 33$ $\mu$H is appropriate.

The efficiency of six-step and unity power factor operation is seen in Fig. 5.2, which plots the calculated efficiencies of the flywheel system with a fixed-voltage six-step drive at unity power factor with a properly sized inductance to reduce harmonic losses. While the efficiency does drop at lower power levels, it still remains adequate even at $5$ kW. Efficient operation at even lower average power levels is possible by running in a pulse mode.

Fig. 5.3 breaks down the three main loss components as a percentage of the total loss for different power levels. At low speeds the field winding loss is higher and the armature loss is lower for a fixed voltage drive. The reason for this is that the back-emf is kept nearly constant with a fixed-voltage drive, which requires more field-winding excitation at lower speeds. In addition, since the back-emf is also nearly independent of the power level, at low power levels the percentage of the total loss due to the field winding and core loss dominate since the armature currents are relatively small.

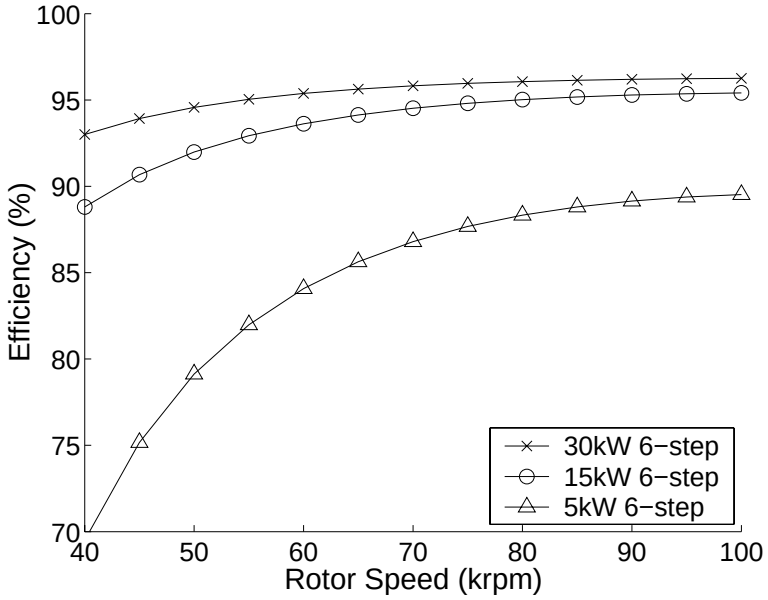


Figure 5.2: Plot of simulated machine efficiency versus speed.

In summary, a six-step inverter drive has many benefits over a PWM drive in this application, and operating at unity power factor has considerable benefits in terms of the $VA$ rating.

## 5.2 Dynamics and Control

This section summarizes the results of work conducted by Matthew Senesky on the development of the controller for the machine. This topic is treated with more detail in [34].

### 5.2.1 Machine Model

The homopolar inductor motor has the same terminal characteristics as a traditional field–wound synchronous machine. Using a two–phase stator model, we have two orthogonal armature windings whose orientations are denoted as axes $a$ and $b$. A field winding along the rotor axis $f$ has mutual inductance with the armature; this inductance varies with the angle $\theta$ between

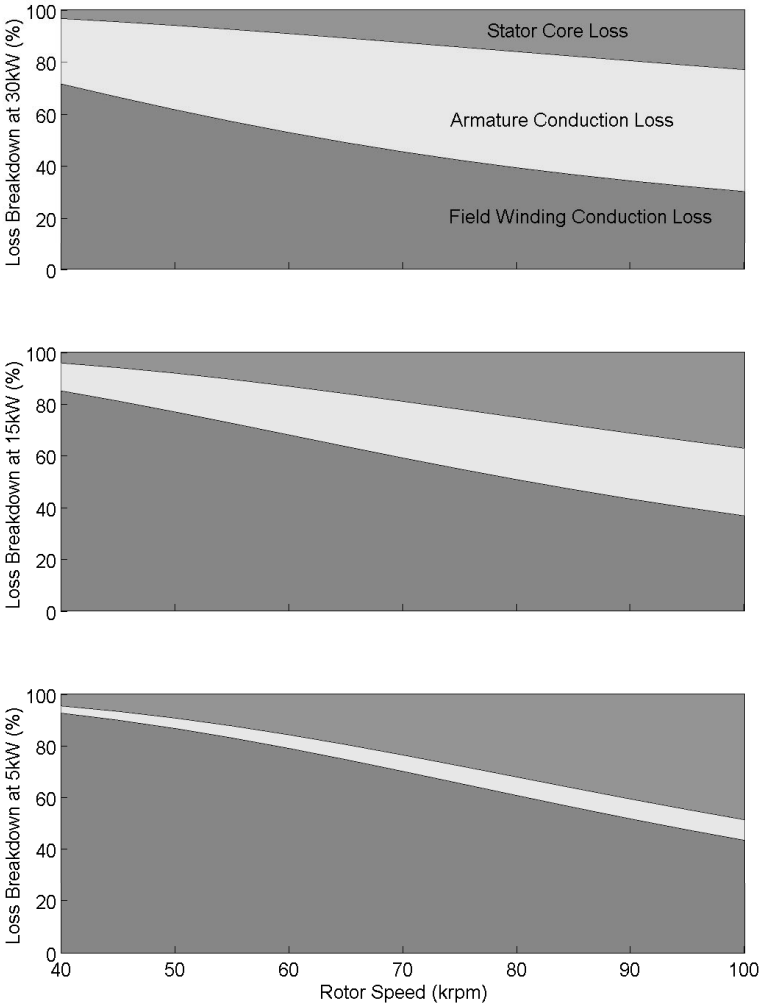


Figure 5.3: Breakdown of calculated losses as a percentage of the total loss versus rotor speed for the prototype machine. Plots are shown for 30 kW, 15 kW, and 5 kW. The labels for the loss components in the 30 kW plot also apply to the other plots.

the $a$ and $f$ axes. Thus in a stationary reference frame we have the two–axis model

$$\frac{d}{dt}\lambda_{abf} = -\mathbf{R}\mathbf{L}^{-1}\lambda_{abf} + V_{abf} \tag{5.1}$$

where

$$\mathbf{R} = \begin{bmatrix} R & 0 & 0 \\ 0 & R & 0 \\ 0 & 0 & R_f \end{bmatrix} \tag{5.2}$$

$$\mathbf{L} = \begin{bmatrix} L & 0 & L_m\cos\theta \\ 0 & L & -L_m\sin\theta \\ L_m\cos\theta & -L_m\sin\theta & L_f \end{bmatrix} \tag{5.3}$$

The mechanical frequency of the rotor is governed by

$$\frac{d}{dt}\omega_m = -\frac{B}{J}\omega_m + \frac{1}{J}\tau_e \tag{5.4}$$

where $J$ is the inertia of the rotor, $B$ represents linear drag, and $\tau_e$ is electrical torque given by

$$\tau_e = \frac{d}{d\theta}\frac{1}{2}\lambda^T\mathbf{L}^{-1}\lambda \tag{5.5}$$

It is advantageous to transform the equations into a synchronous reference frame, which we denote with axes $d$, $q$. The natural choice of input for our six–step drive scheme is the inverter electrical frequency $\omega_e$, and we choose to orient the $q$ axis with the armature voltage vector. As a consequence, $V_q$ is constant, and $V_d$ is identically zero. A high–bandwidth current control loop is implemented to set $i_f$, allowing the dynamics of $\lambda_f$ to drop out of the model. Under these conditions, the electrical dynamics simplify to

$$\frac{d}{dt}\lambda_d = -\frac{R}{L}\lambda_d + \omega_e\lambda_q + \frac{RL_m}{L}i_f\cos\theta \tag{5.6}$$

$$\frac{d}{dt}\lambda_q = -\omega_e\lambda_d - \frac{R}{L}\lambda_q - \frac{RL_m}{L}i_f\sin\theta + V_q \tag{5.7}$$

$$\frac{d}{dt}\theta = \omega_e - 4\omega_m \tag{5.8}$$

where (5.8) describes the evolution of the angle, $\theta$, between the reference frame and the rotor. Finally, we are interested in the outputs $i_d$ and $i_q$:

$$i_d = \tfrac{1}{L}\lambda_d - \tfrac{L_m}{L} i_f \cos\theta \tag{5.9}$$

$$i_q = \tfrac{1}{L}\lambda_q + \tfrac{L_m}{L} i_f \sin\theta \tag{5.10}$$

Since the principle function of the flywheel energy storage system is as an electrical energy reservoir, we wish to control the flow of electrical power into and out of the machine rather than a mechanical quantity such as torque or speed. Our strategy for this is to focus on the electrical variables, developing instantaneous control of electrical power flow, considering the speed to vary slowly. The effect of extracting or supplying power to the machine is to decelerate or accelerate the rotor, respectively. Explicitly, real power is controlled by regulating $i_q$, while reactive power is controlled by regulating $i_d$.

For consideration of the electrical power flow dynamics, we treat the speed as a constant parameter. A more formal analysis would rely on singular perturbation theory with speed and other mechanical variables treated as forming the "slow subsystem". We omit the details here — a general treatment can be found in [23]. Holding $w_m$ constant and performing a small signal linearization of the electrical subsystem about a desired operating point, we obtain a linear state-space model for the electrical subsystem. We then compute the transfer function matrix $H(s)$, partitioned as:

$$\begin{bmatrix} i_d(s) \\ i_q(s) \end{bmatrix} = \begin{bmatrix} H_{11} & H_{12} \\ H_{21} & H_{22} \end{bmatrix} \begin{bmatrix} i_f(s) \\ \omega_e(s) \end{bmatrix} \tag{5.11}$$

where the functions $H_{11}$, $H_{12}$, $H_{21}$, and $H_{22}$ are given by equations (5.12)-(5.15).

Table 5.1: Small–signal operating point.

| | |
|---|---|
| $V$ | 70 V |
| $\theta$ | $15^\circ$ |
| $\omega_e$ | 6283 rad/s |
| $i_d$ | 0 A |
| $i_q$ | 80 A |
| $i_f$ | 9.29 A |
| $\lambda_d$ | $9.9 \times 10^{-3}$ Wb |
| $\lambda_q$ | 0 Wb |

$$H_{11} = -\left(\tfrac{L_m}{L}\cos\theta\right)\frac{s^2 + \tfrac{R}{L}s + \omega_e^2 + \omega_e\tfrac{R}{L}\tan\theta}{D} \tag{5.12}$$

$$H_{21} = \left(\tfrac{L_m}{L}\sin\theta\right)\frac{s^2 + \tfrac{R}{L}s + \omega_e^2 - \omega_e\tfrac{R}{L}\cot\theta}{D} \tag{5.13}$$

$$H_{12} = \{i_q s^2 + \left(\tfrac{R}{L}i_q - \tfrac{1}{L}\omega_e\lambda_d\right)s + \omega_e^2\left(i_q - \tfrac{1}{L}\lambda_q\right) + \omega_e\tfrac{R}{L}\left(i_d - \tfrac{1}{L}\lambda_d\right)\}/\{sD\} \tag{5.14}$$

$$H_{22} = \{-i_d s^2 - \left(\tfrac{R}{L}i_d + \tfrac{1}{L}\omega_e\lambda_q\right)s - \omega_e^2\left(i_d - \tfrac{1}{L}\lambda_d\right) + \omega_e\tfrac{R}{L}\left(i_q - \tfrac{1}{L}\lambda_q\right)\}/\{sD\} \tag{5.15}$$

$$D = s^2 + 2\tfrac{R}{L}s + \left(\tfrac{R}{L}\right)^2 + \omega_e^2 \tag{5.16}$$

Bode plots of these functions are shown in Fig. 5.4. Table 5.1 gives the operating point values used to generate the plots. Note that at low frequencies the magnitude of the diagonal terms is larger than that of the off–diagonal terms. Although for clarity we only plot results for one operating point, the qualitative relationship among the magnitudes of the four terms holds over a wide range of operating points. This carries important consequences for our control, as discussed in section 5.2.2.

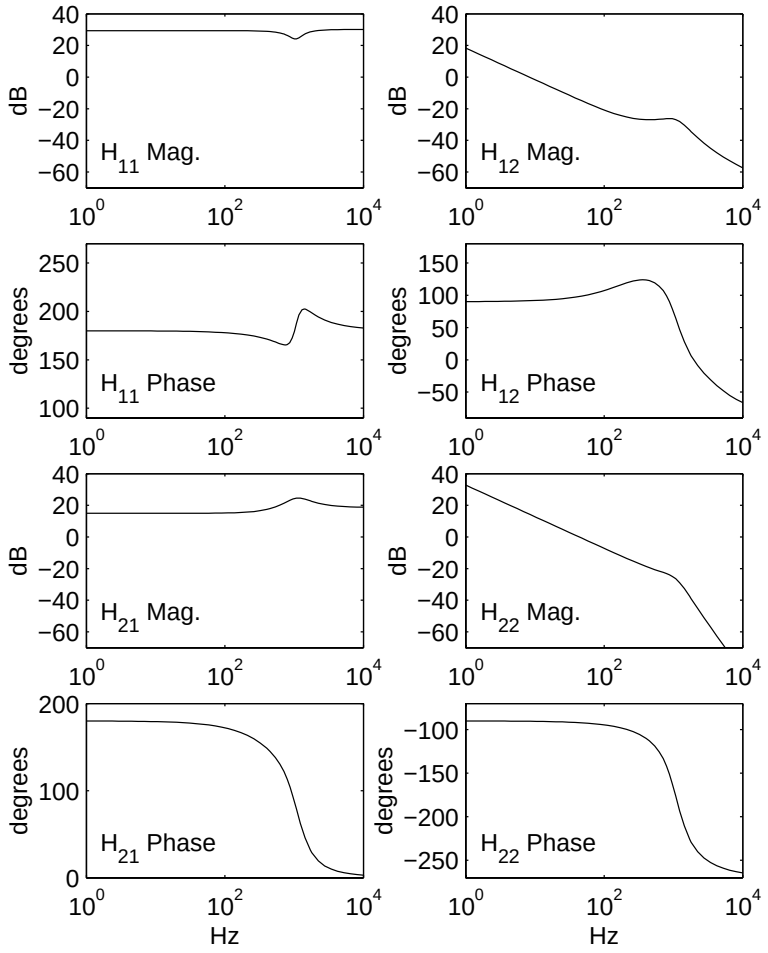


Figure 5.4: Bode plots for the homopolar inductor motor.

### 5.2.2 Control Design

The objective in designing a controller is to stabilize the system for operating points near unity power factor, and to be able to track a command for real power. As the excitation voltage is fixed, this amounts to controlling $i_q$ to a reference value while keeping $i_d$ at zero. Intuition for the operation of the system at or near unity power factor can be gained by examining the phasor diagram in Fig. 5.1. Note that the figure is not drawn to scale; over the desired range of operating points, the angle $\theta$ will be small, and the effect of resistive drop will be negligible. Letting $\sin(\theta) \cong \theta$, $i_q$ varies nearly linearly with $\theta$ (and hence the integral of $\omega_e$) with little effect on $i_d$. Similarly, adjusting the magnitude of the back–emf $E$ controls $i_d$ with little effect on $i_q$. These are the standard relations for a synchronous generator connected to an infinite bus [6].

The Bode plots for the linearized system shown in Fig. 5.4 confirm the intuition of the phasor diagram, and provide insight into the dynamics of the electrical states. It can be shown that for the purposes of the control scheme, the relative magnitudes of the quantities $|H_{11}H_{22}|$ and $|H_{12}H_{21}|$ to a large extent determine whether the system can be treated as a pair of decoupled scalar systems [34]. Adding the log magnitudes from the figure, we see that $|H_{11}H_{22}|$ is greater than $|H_{12}H_{21}|$ by roughly 30 dB at low frequencies.

Given the decoupled nature of the system, we can construct two independent control loops, as shown in the block diagram in Fig. 5.5. An integral control law for the $i_d \rightarrow i_f$ loop ensures that the power factor is driven to unity. A PI control on the $i_q \rightarrow \omega_e$ loop provides the desired response for tracking the commanded active current. Table 5.2, showing the resulting closed–loop poles for the linearized system, confirms that the control indeed stabilizes the system at the desired operating point.

An attractive feature of the control scheme is in its simplicity. Unlike flux–oriented

Table 5.2: Closed–loop poles.

| |
|---|
| $-2709 \pm 6063j$ |
| $-558.3$ |
| $-354.9$ |
| $-76.21$ |
| $-0.145$ |

schemes, this controller does not require an observer to resolve the reference frame. The reference frame angle $\phi$ is defined by the inverter voltage, therefore the angular orientation of the reference frame with respect to the stator is known explicitly from the commanded voltage. The sampling and control loops are triggered synchronously with the inverter switching. Furthermore, because the magnitude of the excitation voltage is fixed, it is only necessary to sample the armature currents. Note that while field current is also sampled to implement a separate current control loop, this sampling is not fundamentally necessary for the overall control scheme — it is a design choice to simplify the experimental setup. The inverter switching and the generation of a sampling interrupt are both handled by an FPGA. Samples of $i_d$ and $i_q$ are taken just before inverter switching occurs, so that the orientation of the current relative to inverter voltage is known. Note that this means sampling occurs at a rate of six times the electrical frequency. These samples, rotated into the synchronous reference frame, are then made available to the control loop, which performs control calculations at a fixed rate of 1.5 kHz.

### 5.2.3 Controller Simulation and Experimental Results

Figure 5.6 shows system response to step commands in $i_d$ from 80 A to -80 A, and -80 A to 80 A, while $i_d$ is commanded to a constant zero. The plots show experimental results and the current commands. Fig. 8.13 shows the inverter frequency corresponding to this power trajectory, and demonstrates the controller's capability to execute constant current accelerations

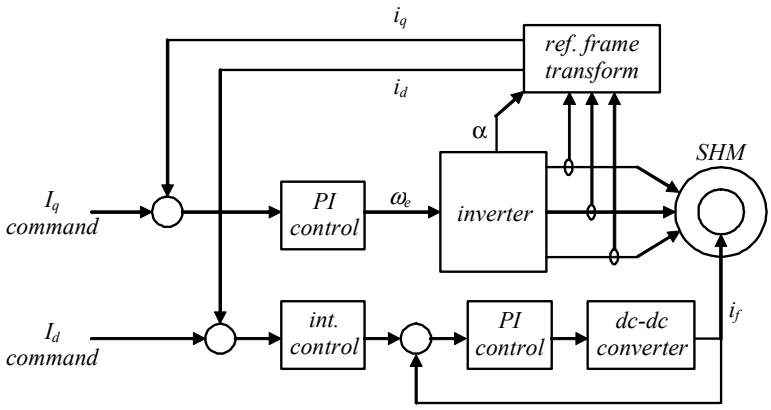


Figure 5.5: Control system block diagram.

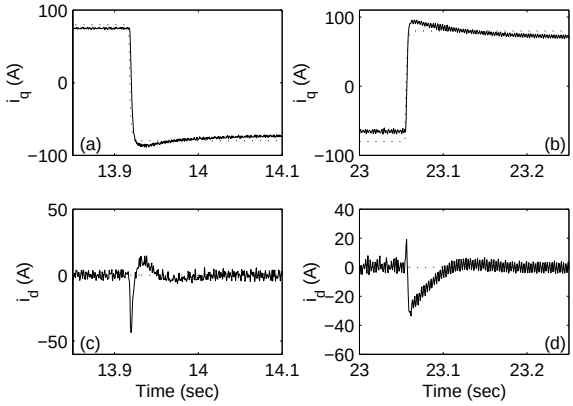


Figure 5.6: Experimental step response, command (dotted) and output (solid). Plots (a) and (c) show $i_q$ and $i_d$ response to a +80 A to –80 A command of $i_q$. Plots (b) and (d) show response to a –80 A to +80 A command.

and decelerations, and the parameters for the simulated results are given in Table 5.3.

Table 5.3: Simulation parameters.

| Description | Design Value | Measured Value |
|---|---|---|
| Armature Inductance $L$ | $33\ \mu$H | $33\ \mu$H |
| Mutual inductance $L_m$ | $1.1$ mH | $1.0$ mH |
| Residual flux $\lambda_r$ | NA | $0.0018$ Wb |
| Armature resistance $R_a$ | $42.0$ m$\Omega$ | $45.4$ m$\Omega$ |
| Field resistance $R_f$ | $3.22\ \Omega$ | $3.44\ \Omega$ |
| Moment of inertia $J$ | $0.123\,\text{kg}\cdot\text{m}^2$ | $0.134\,\text{kg}\cdot\text{m}^2$ |

# Chapter 6

# Harmonic Loss Calculations

This chapter presents the methods used to calculate losses arising from time harmonics generated by a six-step drive and winding spatial harmonics. The harmonic losses that are of the most concern are those due to eddy currents flowing in the solid-steel rotor which are generated when the rotor sees a time-varying flux generated from either harmonic currents or spatial effects.

The time harmonics in this motor arise from the switching of the inverter. Since six-step drive is applied, the harmonics are of a relatively low frequency, occurring at integral multiples of $6\omega_e$ (six times the fundamental electrical frequency) in the rotor frame. The harmonic currents from this switching cause additional armature conduction loss, rotor loss, and stator core loss. Calculations for the armature harmonic conduction and rotor harmonic loss are presented in sections 6.1 and 6.2; the stator core harmonic loss can be analyzed using standard core loss methods based on manufacturers data for the core material.

The magnitude of the harmonic losses from time-varying currents can be controlled by adjusting the armature inductance $L$. Increasing $L$ either by changing the winding design or adding external inductors reduces the harmonic losses, however it also reduces the achievable

Table 6.1: Harmonic losses for prototype design

| **Parameter** | **Prototype Value** |
|---|---|
| **Motor and drive Parameters** | |
| $L$ | 33 $\mu$H |
| Voltage fundamental $V$ | 100 V |
| Phase current $I_a$ | 66 A |
| Speed range $\omega_m$ | 30 krpm-60 krpm |
| Corresponding elec. freq. $\omega_e$ | 2.0 kHz-4.0 kHz |
| **Worst-case harmonic losses** | |
| (at 9.4 kW, 30 krpm) | |
| Stator Harm. Curr. Cond. Loss | 7.9 W |
| Rotor Time Harmonic Loss | 100 W |
| Rotor Spatial Harmonic Loss | $<$ 1.0 W |
| **Average harmonic losses** | |
| (9.4 kW, 30 krpm-60 krpm) | |
| Stator Harm. Curr. Cond. Loss | 3.0 W |
| Rotor Time Harmonic Loss | 50.8 W |
| Rotor Spatial Harmonic Loss | $<$ 1.0 W |

motor power factor when operating at inverter unity power factor, and impacts overall efficiency. Design criteria for sizing $L$ to achieve a minimum machine power factor over a certain operating range is presented in Section 6.3.

The slotless stator in this motor eliminates slot harmonics, therefore the spatial harmonics are from the trapezoidal winding distribution and from the rotor flux MMF profile. The losses from the trapezoidal winding distribution are discussed in section 6.4. Rotor flux MMF profile harmonics are only present in the square-cut rotor. Since they cause losses in the stator, they can also be analyzed using the same methods for calculating stator core loss, and they are not discussed in this chapter.

Table 6.1 summarizes the calculations for the harmonic losses of the prototype during one of the experiments. Indicated in the table are the worst-case losses and average losses for each harmonic loss component for the 9.4 kW, 30 krpm-60 krpm test.

## 6.1 Stator Harmonic Current Conduction Loss

The voltage on phase $a$ of a 3-phase motor driven with a six-step excitation at an electrical frequency $\omega_e$ can be expressed as a sum of its Fourier components:

$$V_a = V \sum_{k=1,5,7,11,13...} A_k \cos(k\omega_e t + \frac{\pi}{2}) \tag{6.1}$$

where $V = \frac{4}{\pi}\frac{V_{bus}}{2}$ is the amplitude of the stator voltage and $A_k = \frac{1}{k}$ is the coefficient for each harmonic component. Triple-n harmonics are excluded by the 3-phase connection of the motor. Phase voltages $V_b$ and $V_c$ have analogous expressions shifted by $+2\pi k/3$ and $-2\pi k/3$, respectively. Neglecting resistance, the expression for the phase currents is then:

$$I_a = V \left( \sum_{k=1,5,7,11,13...} \frac{A_k}{k \cdot \omega_e \cdot L} \cos(k\omega_e t) \right) - \frac{E}{\omega_e \cdot L} \cos(\omega_e t) \tag{6.2}$$

where $L$ is the phase inductance, and $E$ the back emf as a complex vector.

The back-emf only has a fundamental component, therefore the additional conduction in phase $a$ for the harmonic currents is then:

$$\begin{aligned} P_a &= \sum_k \frac{1}{2} I_{ak}^2 R \\ &= \textstyle\sum_k \ \frac{1}{2} V^2 \left( \frac{A_k}{k \cdot \omega_e \cdot L} \cos(k\omega_e t) \right)^2 R \end{aligned} \tag{6.3}$$

for:

$$k = 5, 7, 11, 13...$$

As evident from equation (6.3), increasing $L$ decreases the amplitude of the harmonic currents and thus the associated losses. The additional conduction losses expressed as a fraction of the peak fundamental conduction losses is:

$$\frac{P_a}{P_{fund}} \approx \frac{I_{a5}^2 + I_{a7}^2 + ...}{I_{a1}^2} \tag{6.4}$$

where $I_{an}$ is the amplitude of the *n-th* harmonic current in phase $a$, and $I_{a1}$ is the peak fundamental current in phase $a$. The harmonic currents are present whenever the six-step voltage is applied, and the highest losses occur at the lowest speeds. For the example shown in Table 6.1, the worst-case losses represent less than 2% of the armature losses, and 0.1% of the total output power.

## 6.2 Rotor Time Harmonic Loss Analysis

Since the rotor is constructed out of a single piece of solid steel, any time varying flux imposed by either time or spatial harmonics will cause rotor loss and subsequent heating. Thus, care must be taken to ensure that the choice of six-step drive does not cause high rotor losses. The primary flux imposed on the rotor is the dc flux imposed by the field winding. The only time varying fluxes seen by the rotor rotating at synchronous speed are time harmonics from armature currents and spatial harmonics from armature winding geometry. The analysis in this section suggests that losses imposed by the armature current time harmonics are small, and the analysis in Section 6.4 suggests that the losses imposed by the armature winding spatial harmonics are small.

Expressing the phase currents $I_a$, $I_b$, and $I_c$ in terms of their Fourier components as is done in (6.2), and applying the Park transform [12] into the synchronous frame leads to:

$$\begin{aligned} I_d &= \frac{V}{\omega_e \cdot L}\left(\sum_{i=1,2,3\ldots}\left(\frac{A_{6i-1}}{6i-1}+\frac{A_{6i+1}}{6i+1}\right)\cos(6i\omega_e t)\right) \\ I_q &= \frac{V}{\omega_e \cdot L}\left(\left(1-\frac{E}{V_S}\right)+\right. \\ &\qquad \left.\sum_{i=1,2,3\ldots}\left(-\frac{A_{6i-1}}{6i-1}+\frac{A_{6i+1}}{6i+1}\right)\sin(6i\omega_e t)\right) \end{aligned} \tag{6.5}$$

where $A_k$ are defined as in (6.1). Examination of these results shows that the rotor sees the flux

due to the 5th harmonic current as a backward-rotating flux wave shifted to the 6th harmonic frequency, and the 7th harmonic flux as a forward-rotating flux wave also shifted to the 6th harmonic frequency. The result for the 11th and 13th, and higher order harmonics is similar.

In steel, at lower frequencies ($< 100$ Hz), hysteresis loss and eddy current losses are of the same order of magnitude. However, hysteresis loss grows at a rate lower than eddy current loss, which grows proportionally with the square of frequency. The frequency of the 6th harmonic at the minimum operating speed is $6 * 3$ kHz$= 18$ kHz. As a result, at the frequencies of interest, the rotor core losses are dominated by eddy current losses and we neglect hysteresis loss in this analysis. Considering only eddy current losses, then linearity implies that the losses for each harmonic component can be analyzed individually. The losses can then be estimated by analyzing the case of a travelling wave of the appropriate amplitude impinging on a solid steel sheet.

An analytical expression for the losses has been derived in [19] based on transfer function relations found in [28]. The result is:

$$K_k = \frac{I_k}{W} \tag{6.6}$$

$$P_{loss} = \frac{S|K_k|^2 \, h\omega_e \mu_0^2}{\delta_h \mu[(b\sinh bg + \frac{\mu_0}{\mu}\frac{1}{\delta_h}\cosh bg)^2 + (\frac{\mu_0}{\mu}\frac{1}{\delta_h}\cosh bg)^2]} \tag{6.7}$$

$$b = \frac{m}{r} \tag{6.8}$$

where $K_k$ is the linear current density in $A/m$ along the inner bore of the stator, $I_k$ is the amplitude of the current harmonic, $W$ is the width of the armature wire, $S$ is the surface area, $\delta_h$ is the skin depth for the material at frequency $w_e$, $r$ is the rotor radius, $g$ is the gap, and $m$ is the spatial harmonic. Since the skin depth $\delta_h << r$, the problem can be transformed with good accuracy into rectilinear coordinates. The constant $b$ is a result of the coordinate transformation, and $m = (\#\ of\ poles)/2$.

The results from this expression agree with 2D FEM simulations of the rotor profile

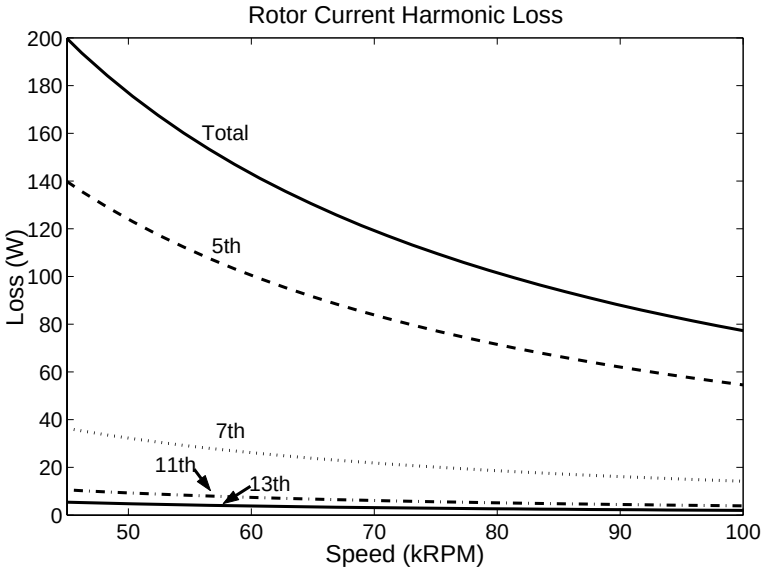


Figure 6.1: Rotor core losses due to armature current time harmonics.

conducted at lower frequencies (1 kHz). Accurate FEM simulations at the frequencies of interest in our design ($\omega_e > 2\pi 18\,\text{kHz}$) are difficult because the skin depths ($26\ \mu$m at $18\,$kHz) are very small compared to the air gap (2.16 mm) and other rotor geometry.

Fig. 6.1 plots the losses calculated for the 5th, 7th, 11th, and 13th harmonics along with the total loss for all harmonics for the target operating speed range with $V = 160\,V$ and $L = 33\ \mu$H. Note that the harmonic losses decrease with increasing speed, and the worst case is 175 W which occurs at 50,000 rpm. The losses decrease with speed because the amplitude of the current harmonic decreases at higher frequencies. The average losses under normal operating cycles would be smaller. A calculation of the rotor's thermal radiation indicates that $175$ W of rotor loss with a stator temperature of $50°C$ would imply a rotor operating temperature of approximately $200°C$, which is reasonable for a solid steel rotor.

## 6.3 Sizing of Armature Inductance $L_a$

As noted in the previous two sections, increasing armature inductance $L$ decreases losses due to the harmonics generated from a six-step drive. However, if running at unity inverter power factor, increasing the armature inductance decreases the machine power factor and the overall efficiency of the machine. One approach to constraining $L$ is to choose a maximum acceptable amplitude for one of the harmonic currents and a minimum machine power factor.

Define $I_{a1}$ to be the amplitude of the fundamental current and $I_{a5}$ to be the amplitude of the fifth harmonic current (the primary source of harmonic losses), and $\theta_{pf}$ to be the angle to achieve the machine power factor $\cos\theta_{pf}$. Then choose $\beta$ such that satisfying the inequality:

$$I_{a5} < \beta \cdot I_{a1} \tag{6.9}$$

leads to small enough harmonic currents such that the harmonic conduction and rotor losses are acceptable. Then substituting in the expression for the amplitude of the fifth harmonic component of the current from (6.2) for $I_{a5}$ leads to the expression:

$$\frac{1}{\beta \cdot 5^2} < \frac{\omega_e L I_{a1}}{V} \tag{6.10}$$

Now a constraint for the minimum machine power factor will be developed. From the phasor diagram in Fig. 5.1, where the inverter is running at unity power factor and the machine power factor angle is $\theta$, the machine power factor will be greater than $\cos\theta_{pf}$ if:

$$\frac{|j\omega_e L I_{a1}|}{V} < \tan\theta_{pf} \tag{6.11}$$

Combining (6.10), (6.11), and $P = \frac{3}{2} I_{a1} V$ results in:

$$\frac{1}{\beta \cdot 5^2} < \frac{2\omega_e L P}{3V^2} < \tan\theta_{pf} \tag{6.12}$$

This expression helps to guide the choice of $L$ so that the harmonic losses can be limited to some maximum value while a minimum machine power factor at peak power is also maintained. Note that in a six-step drive where $V$ is fixed, the ratio of the maximum speed over minimum speed is constrained by:

$$\frac{\omega_{e,\max}}{\omega_{e,\min}} < \beta \cdot 5^2 \cdot \tan\theta_{pf} \tag{6.13}$$

Given the desired 2:1 speed range, and using $\beta = 0.12$ (the value used for the example in Table 6.1), then (6.13) implies a minimum machine power factor of 0.83. This minimum machine power factor occurs at full power at $w_{e,max}$. At full power at $w_{e,min}$ the machine power factor would be 0.94. Both cases assume that the inverter is running at unity power factor.

## 6.4 Rotor Spatial Harmonic Loss Analysis

Calculations for the losses associated with spatial winding harmonics ('belt harmonics') can be calculated in a similar fashion to the current harmonic losses. The prototype motor has a trapezoidal winding MMF, and the surface current $K_a$ of phase $a$ with current $I_a$ flowing can also be expressed in terms of its Fourier components as:

$$K_a = \frac{I_a}{W}\cos(\omega_e t) \sum_{m=1,3,5\ldots} K_m \cos(m\,\theta_s) \tag{6.14}$$

where $\theta_s$ is the spatial angle along the bore of the motor, $W$ the width of one turn, and $K_m$ the amplitude of the m*th* harmonic. The sum of the surface currents for the three phases is the resultant MMF:

$$K_{tot} = K_a + K_b + K_c \tag{6.15}$$

It can be shown that when balanced three phase sinusoidal currents $I_a$, $I_b$, and $I_c$, of equal amplitude $|I|$ are applied and $K_{tot}$ is expressed in the rotor frame, $K_{tot}$ can be expressed as a sum of $6i$ time harmonics [19]:

$$\begin{aligned} K_{tot} = \frac{3}{2}\frac{|I|}{W}[K_1 \cos\theta_s \\ + \sum_{i=1,2,3...} K_{6i-1}\cos((6i-1)\theta_s + 6i\omega_e t)) \\ + \sum_{i=1,2,3...} K_{6i+1}\cos((6i+1)\theta_s + 6i\omega_e t))] \end{aligned} \tag{6.16}$$

Since these losses also appear as traveling waves at the 6th harmonic frequency, the losses can be analyzed using (6.7), with the modification of b such that:

$$b = \frac{m \cdot l}{r},\ l = 5, 7, 11, 13... \tag{6.17}$$

to reflect the change in the spatial wavelength of the harmonic.

The rotor losses from the winding harmonics are much smaller than the losses from the current harmonics. There are two reasons for this. First, the spatial MMF patterns are trapezoidal for each phase, significantly reducing the 5th and 7th harmonic amplitudes relative to a square-wave MMF pattern. Second, the spatial wavelength for the first winding harmonic induced MMF impinging on the rotor is one-fifth that which corresponds to the fundamental wavelength, resulting in reduced flux penetration into the rotor volume. In the worst case, these losses are estimated at less than 1W. The above spatial harmonic analysis only considers the losses from spatial harmonics driven by the fundamental current. The losses from spatial harmonics due to temporal harmonic currents (e.g. 5th spatial harmonic with 7th current harmonic) have a negligibly small contribution to the total loss.

# Chapter 7

# Prototype Construction

This chapter summarizes how the prototype flywheel energy storage system was built and how the inverter and controller were implemented. Detailed mechanical drawings of the parts are included in Appendix A, and the CAD files for all the drawings are provided on a CD-ROM. The code for the Altera FPGA and dSPACE controller and instructions on operating the flywheel are also provided on the CD-ROM, the contents of which are described in Appendix B.

## 7.1 Motor and Flywheel Construction

The construction of the rotor, stator, housing, and bearing system is described in this section. A photo of the complete stator and the sinusoidal rotor is shown in Fig. 7.1. The dimensions, and other important parameters for the prototype are shown in Tables 2.1 and 4.1.

### 7.1.1 Rotor

The rotor for the machine consists of a single piece of high strength steel. As shown in Fig. 2.4 and Fig. 7.2, four poles are cut into both the upper and lower parts of the rotor with the

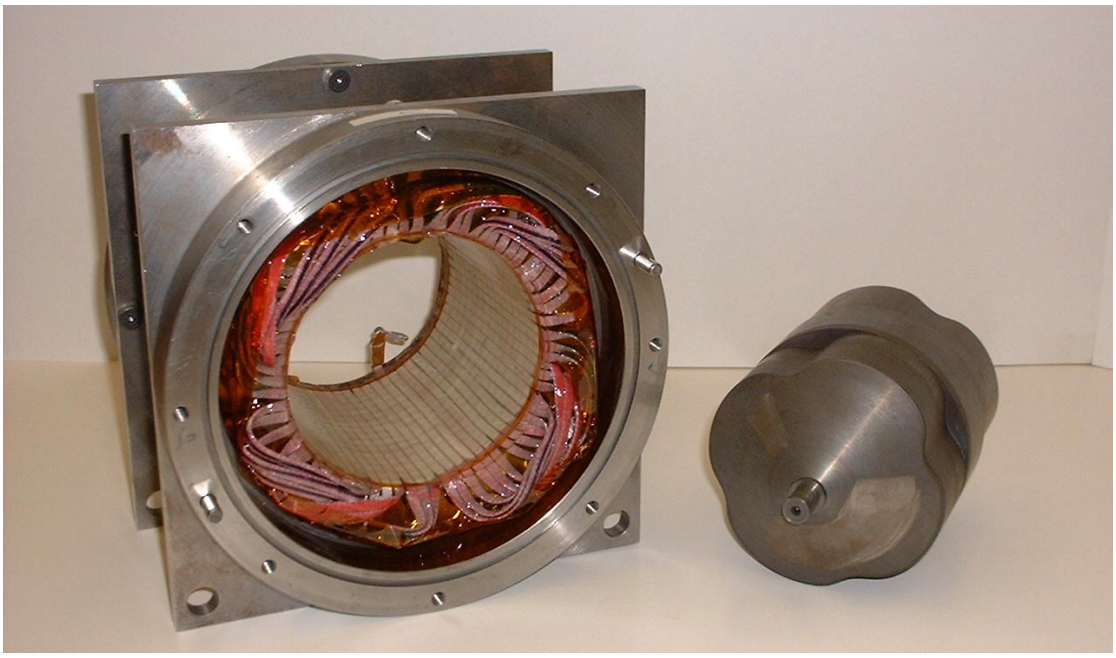

Figure 7.1: Photo of completed stator and sinusoidal rotor.

lower poles rotated 45 degrees with respect to the upper poles. The center portion of the rotor is cylindrical, and the field winding encircles this portion of the rotor. The four upper poles are all the same magnetic polarity (N), and the flux returns down through the backiron to the lower set of poles (S). The machine has 8-poles, and no saliency, i.e. $Ld/Lq = 1$.

Two different rotors were built, as shown in Fig. 7.2. The profile for each rotor was analyzed using FEM, and a shape optimization was applied to achieve the desired rotor MMF profile. For the sinusoidal rotor, the goal was design a rotor to achieve a sinusoidal MMF waveform with no harmonics. A minimum and maximum magnetic gap were specified, and a 2D FEM analysis was conducted to determine the MMF waveform for a given rotor profile. The rotor profile was modified iteratively to minimize the harmonics. Fig. 7.3 shows the sinusoidal rotor profile and the resulting MMF profile.

For the square-cut rotor, a finite element method (FEM) analysis was used to adjust the

Figure 7.2: Photo of squarecut and sinusoidal rotors. Although they have different pole profiles and MMF waveforms, both rotors have 8-poles and have no saliency ($L_d/L_q$=1).

size of the pole-face arc with parameter $\alpha$ (as defined in Fig. 3.3) so that the rotor would have an $L_d/L_q = 1$. Since the FEM analysis takes into account the effects of fringing flux, the pole faces were adjusted so that they spanned $42^\circ$ instead of the full $45^\circ$ if fringing flux were ignored.

The two rotor shapes were built with the intent of comparing their performance. The sinusoidal rotor has no rotor MMF harmonics so its associated stator core loss would presumably be smaller. However it also has a lower $L_{mf}$ which would then require more field winding excitation to achieve the same flux level. Unfortunately, the square-cut rotor was damaged during a bearing failure before complete experimental results could be obtained, and a comparison was not possible.

### 7.1.2 Housing

The housing consisted of a carbon steel tube that contained the stator stacks and field winding, and endplates made out of stainless steel. Fig. 7.5 displays the parts of the housing before assembly.

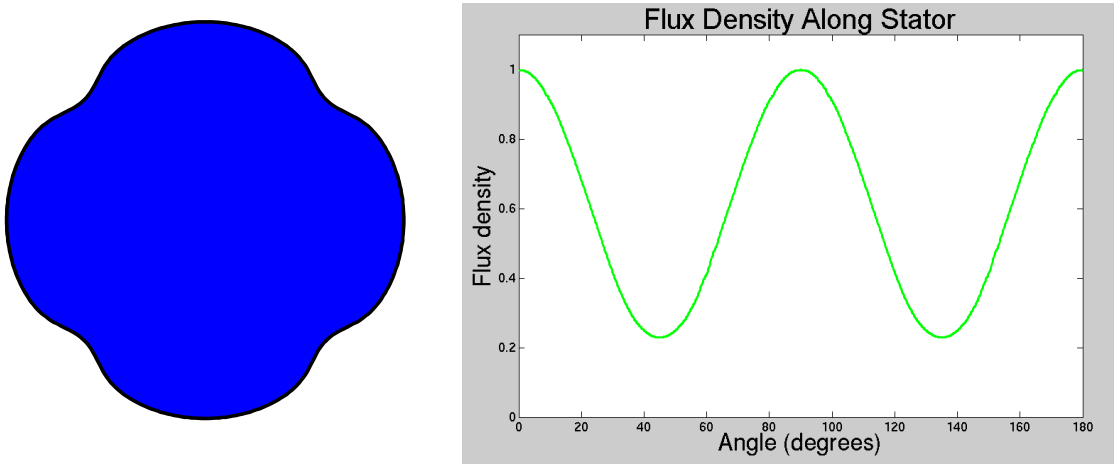


Figure 7.3: Profile of sinusoidal rotor, and results of FEM analysis showing the sinusoidal MMF waveform imposed by the rotor on the stator.

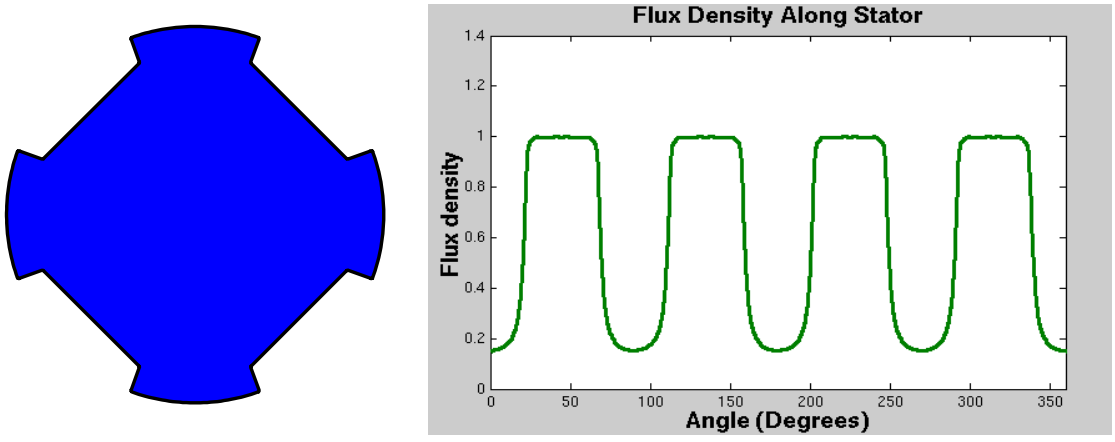


Figure 7.4: Profile of square-cut rotor, and results of FEM analysis showing the MMF waveform imposed by the rotor on the stator.

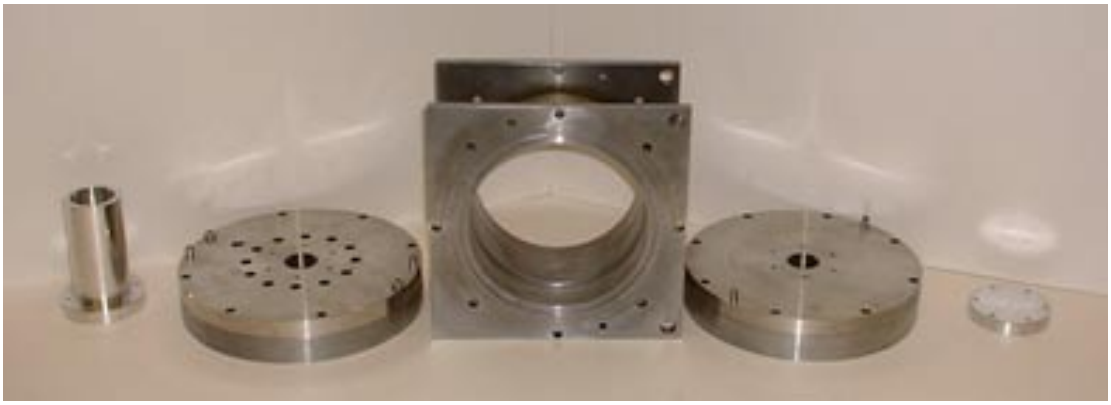

Figure 7.5: View of housing parts. From left to right: the thermocouple mount endcap, the endplate with feedthrough holes, main housing, endplate, and endcap.

One of the endcaps was modified to accommodate an infrared thermocouple which was used to measure the temperature of the rotor. All the wiring was connected through vacuum-sealed feedthroughs, which were all located on one endplate. The same endplate also contained a vacuum connection to connect to the vacuum pump.

### 7.1.3 Stator

The stator was made from 0.005” thick laminations, stacked and press-fit into a steel tube that serves as both the back iron and housing for the machine. Only the field winding flux and not the alternating flux of the armature travels through the back iron, so core loss in the back iron is not an issue.

The field winding was wound around a bobbin and also pressed into the backiron. Fig. 7.6 shows the field winding and the split bobbin that it was wound around. The bobbin was made out of aluminum and split into two sections to improve heat transfer to the stator stacks and the housing.

The most challenging part of the prototype construction was the winding of the stator

Figure 7.6: Field winding with aluminum bobbin.

armature. The armature was formed from rectangular Litz wire bonded to the inner bore using thin sheets of FR4 prepreg. FR4 prepreg is the partially-cured form of the yellow-green epoxy-fiberglass laminate commonly used as printed circuit board substrate. The type of FR4 employed here was very thin (roughly $63.5\mu m$ or $0.0025$"). A diagram of the construction assembly is shown in Fig. 7.7. First, a layer of FR4 was placed against the inner bore, followed by the windings, and then an additional layer of FR4 on the inside of the windings. Then an air bladder was inserted and inflated to 1 atm. (15 psi.) to compress the FR4-Litz wire-FR4 assembly against the inner bore. The stator assembly was then baked in an oven to reflow and fully cure the epoxy in the FR4. After baking, the air bladder was removed, and the result was a smooth and solid winding structure bonded tightly to the inner bore of the motor. After the windings are bonded to the inner bore, the endturns are potted using 3M DP-105 epoxy. Photos of the completed armature are shown in Fig. 7.8 and 7.9.

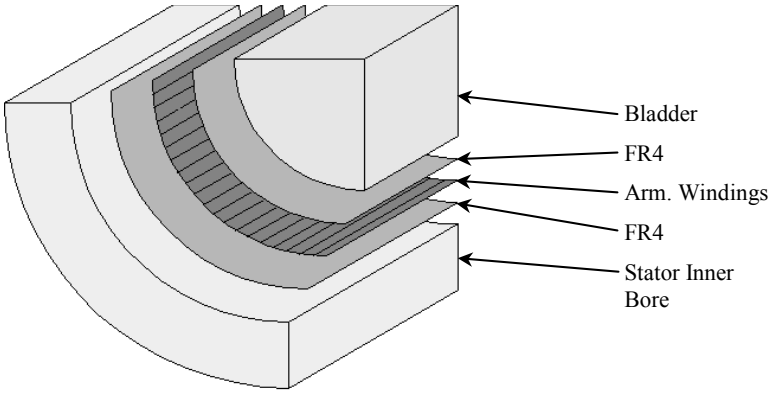


Figure 7.7: Diagram of process for bonding winding to the slotless stator. Drawing is a cutaway view of $\frac{1}{4}$ of stator. A layer of partially cured FR4 is placed against the inner bore of the stator, followed by the windings, and then another layer of FR4. An inflatable bladder is used to compress the assembly, and then the assembly is baked to reflow the epoxy in the FR4 and fully cure it.

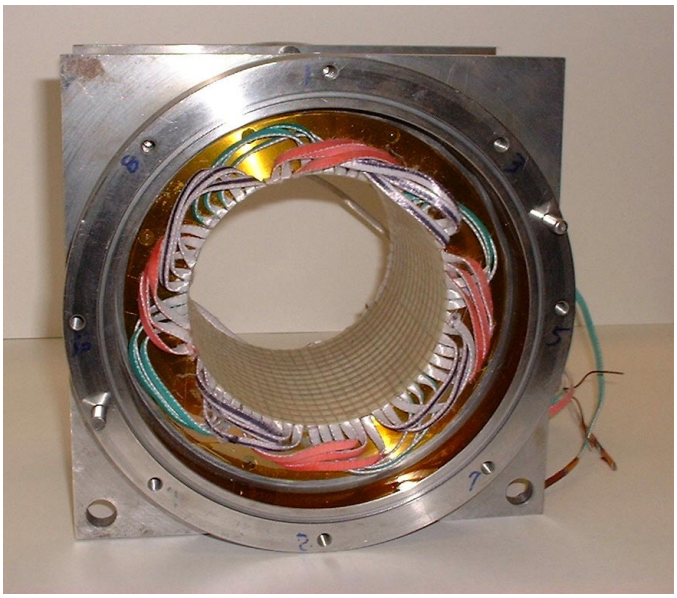

Figure 7.8: View of completed stator and armature winding.

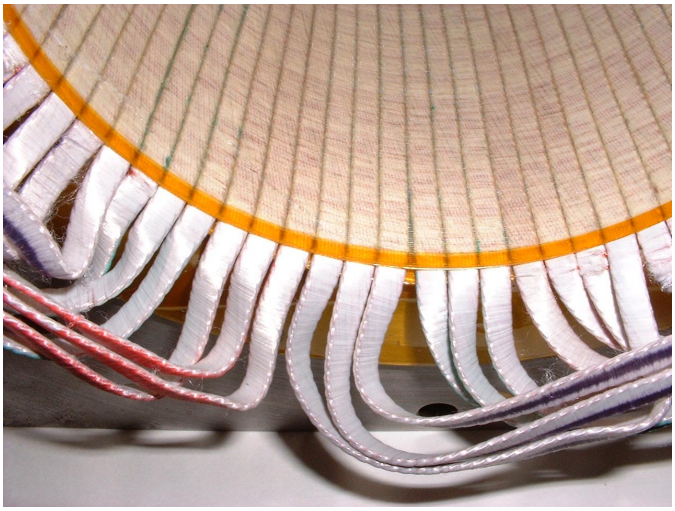

Figure 7.9: Close-up view of armature winding.

### 7.1.4 Compliant Bearing Mount

A compliant bearing mount was designed and built to allow the rotor to operate at high speeds, as described in 4.1.3. The mount consisted of a 'tolerance ring' [36] clamped around the outside of the bearing, and compressed into a bore. The tolerance ring, shown in Fig. 7.10 is a band of spring steel with ridges that flex to provide compliance.

Angular contact ball bearings with ceramic nitride balls were used (Barden model number CZSB101JSSDL). An axial preload is necessary for angular contact bearings to operate properly. In this design, a 20 lbf. preload was provided by an axially loaded wavespring mounted in one of the endplates.

## 7.2 Inverter, Sensing, and Controller Electronics

Fig. 7.11 diagrams the principle components of the inverter, sensing, and control electronics. The 3-phase inverter consisted of three 600V, 200A IGBT half-bridge packages (Powerex

Figure 7.10: Tolerance ring.

PM200DSA060). The IGBTs were driven by opto-isolated gate driver chips, which were driven by logic level signals generated by the Altera FPGA. The inverter was connect to a dc bus fed by a six-pulse diode rectifier, which was supplied by a 3-phase variac or directly from the line. When discharging the flywheel, a dump resistor (not shown in the diagram) was used to dissipate the excess power from the bus. The field winding for the inverter was powered by a dc-dc converter supplied by a separate 200V power supply. A description of the dc-dc converter can be found in [34].

Current sensors were put in place to measure each of the three motor phases $i_a$, $i_b$, $i_c$, the field winding current $i_f$, and the dc bus current into the inverter $i_{bus}$. Voltage measurements of phase voltages $v_a$, $v_b$, and $v_c$, and $v_{bus}$ were also available. The analog sensing signals were filtered through an analog filtering box which performed a 3-phase to 2-phase conversion on the armature current and armature voltage measurements. The analog filter box is described in [19].

The analog outputs of the analog filter box are sampled by A/D converters on the dSPACE DSP card. The dSPACE processor executes the control algorithm, and calculates updated $\omega_e$-command and $i_f$-command. The $\omega_e$-command is passed to the Altera FPGA, which uses it to generate the gate drive signals. The $i_f$-command is converted into a PWM gate drive signal, which is then passed to the dc-dc converter.

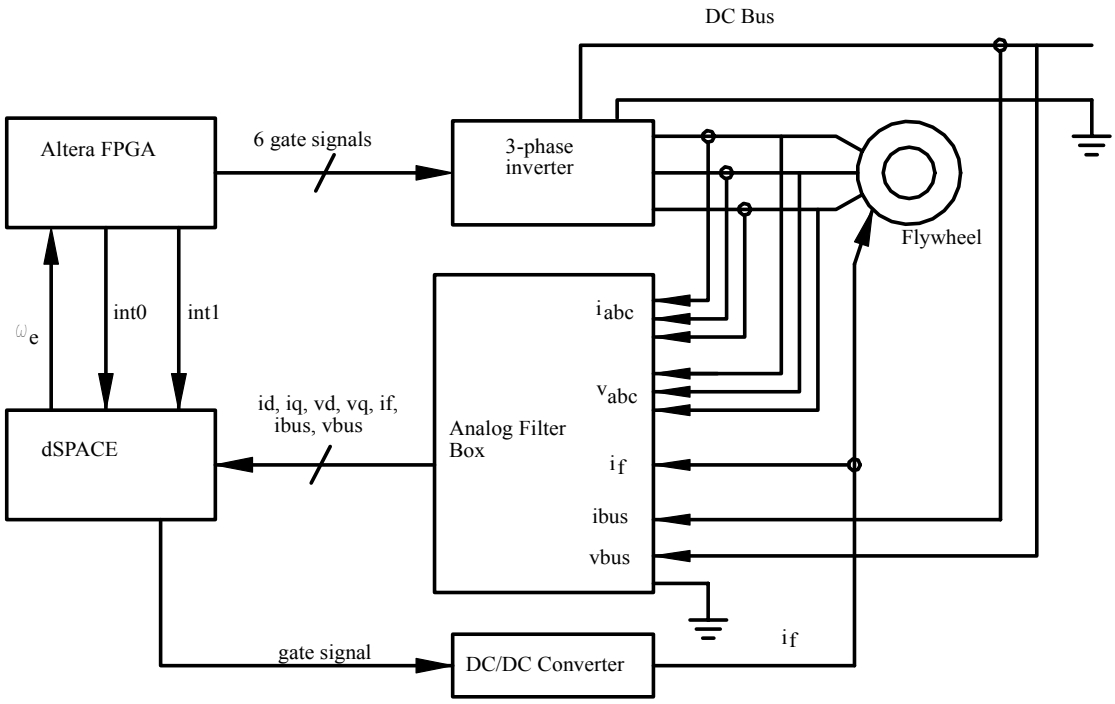


Figure 7.11: Diagram of inverter, sensing, and controller electronics.

## 7.3 dSPACE Controller Software

Fig. 7.12 diagrams the three main processes running in the dSPACE controller. The inverter switching and the generation of a sampling interrupt are both handled by the Altera FPGA, which coordinates the timing with the dSPACE card with control interrupt *int0* and sampling interrupt *int1*.

Sampling interrupt *int1* triggers the sampling process *sample_fcn* in the dSPACE card at a rate of $6\omega_e$. Samples of armature currents and voltages are taken by the A/D converters just before inverter switching occurs, so the orientation of the measurements relative to the inverter voltage is known. These samples (which are measured in the stationary frame) are then rotated into the synchronous reference frame, filtered, and then made available to the motor control process *io_fcn*. Since the sampling process *sample_fcn* runs at a rate of $6\omega_e$, it is typically running 4 to 16 times faster than the control process *io_fcn*. Thus, the filtering has only a small effect on the delay of the controller.

The control process *io_fcn* calculates updated commands for $\omega_e$ and $i_f$ based on the sampled currents $i_d$ and $i_q$. This process is triggered by *int0* at a fixed rate of $1.5kHz$. The interrupt *int0* also synchronizes the communication of the $\omega_e$ command back to the FPGA. The $i_f$ command calculated in *io_fcn* is passed directly to *pwm_fcn*, the dc-dc converter control process. This process is triggered off an internally generated 50 kHz clock, and in each cycle, *pwm_fcn* samples $i_f$, calculates a new duty cycle for the dc-dc converter, and generates the appropriate gate drive signal.

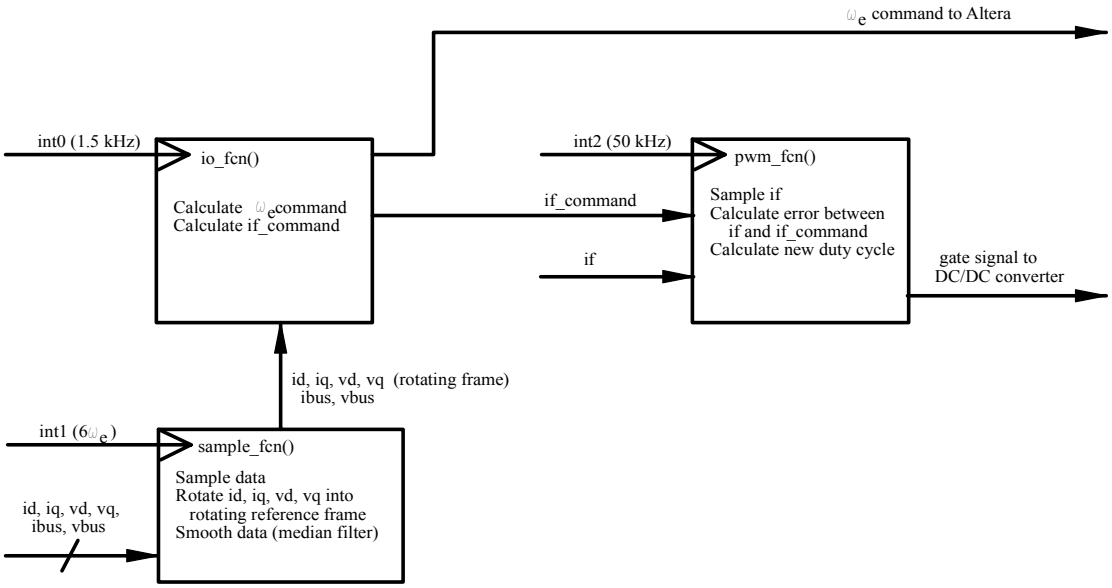


Figure 7.12: Diagram of the processes in the dSPACE controller.

## 7.4 Containment

For safety reasons, the high-speed testing of the flywheel system was conducted in a containment chamber mounted in a pit beneath the surface of the floor. The pit was approximately 3 feet deep and 4 feet by 4 feet in area. The motor was mounted on a steel plate bolted directly to the concrete floor of the pit, and a 3 inch thick steel pipe encircled the flywheel system. Sandbags were placed between the outside wall of the pipe and the concrete wall of the pit. Two 1 inch thick steel plates and sandbags were placed on top of the assembly with a hydraulic lift and bolted down with eight 1 inch diameter steel rods. When completely assembled, the top plates are just below the level of the floor. Cabling for the motor is run through a feedthrough at the bottom of the steel pipe and around the top plates. Photos of the motor in the containment pit are shown in Fig. 7.13.

Figure 7.13: Photo of motor inside the containment pit (top) and photo of containment pit lift and top plates (bottom). When conducting high-speed tests, the top plates (bottom photo, right) are put into place using the hydraulic lift (bottom photo, top).

# Chapter 8

# Experimental Results

This chapter presents the results of the experiments conducted on the prototype flywheel system. The first section describes the methods used to measure the machine parameters, some of which could not be measured directly and had to be calculated or fitted from other data. Section 8.2 describes how the core loss and rotor harmonic losses were measured. The efficiency tests are described in Section 8.3, and Section 8.4 discusses the overall results from the experiments.

## 8.1 Prototype Machine Parameters

The first experimental goal was to determine the machine parameters of the prototype and compare them to the design values. For the purposes of the controller, it can be seen that the primary motor parameters needed for the machine model described in section 5.2.1 are the armature inductance $L$, the mutual inductance $L_m$, armature resistance $R_a$, and rotor inertia $J$. Additional parameters needed to model the losses in the motor include field winding resistance $R_f$, bearing loss coefficients, and core loss coefficients. The dc resistances were measured directly, but most of these parameters were determined by fitting models to experimental measurements.

Table 8.1: Prototype parameters.

| Description | Design Value | Measured Value |
|---|---|---|
| Phase Inductance $L$ | $33\ \mu$H | $33\ \mu$H |
| Armature Inductance | $17\ \mu$H | $22\ \mu$H |
| External Inductor | $11\ \mu$H | $11\ \mu$H |
| Mutual inductance $L_{mf}$ | 1.1 mH | varied from 1.1 mH @ 5.5 A to 0.74 mH @ 14 A |
| Residual flux $\lambda_r$ | NA | $0.0018$ Wb |
| Armature resistance $R_a$ | $42.0$ m$\Omega$ | $45.4$ m$\Omega$ |
| Field resistance $R_f$ | $3.22\ \Omega$ | $3.44\ \Omega$ |
| Moment of inertia $J$ | $0.123\,\text{kg}\cdot\text{m}^2$ | $0.134\,\text{kg}\cdot\text{m}^2$ |

A summary of the designed and measured values for these parameters is shown in Table 8.1. All experimental data was obtained using discrete inductors in series with the motor phases to increase the phase inductance $L$ to the desired value of $33\,\mu$H. All tests were conducted under a moderate vacuum of roughly $500$ Pa.

### 8.1.1 Measuring $L_{mf}$

The mutual inductance $L_{mf}$ is one of the key parameters needed for determining the efficiency of the machine, and it was measured using two different methods. The first method was to put dc current through the armature and field winding, and then use a torque meter to measure the resulting static torque on the rotor. The armature dc current was provided by a power supply with its positive output connected to phase $a$, and phase $b$ and $c$ tied to the negative output. This current creates a stator flux aligned with the stator phase $a$-axis. Injecting dc current into the field winding then creates a rotor flux aligned with the rotor $d$-axis, which results in a torque that attempts to align the rotor flux with the stator flux.

The peak torque occurs when the rotor and stator fluxes are at $90^\circ$ electrical angle to each other. By using the torque meter to rotate the rotor, the peak torque could be measured, and

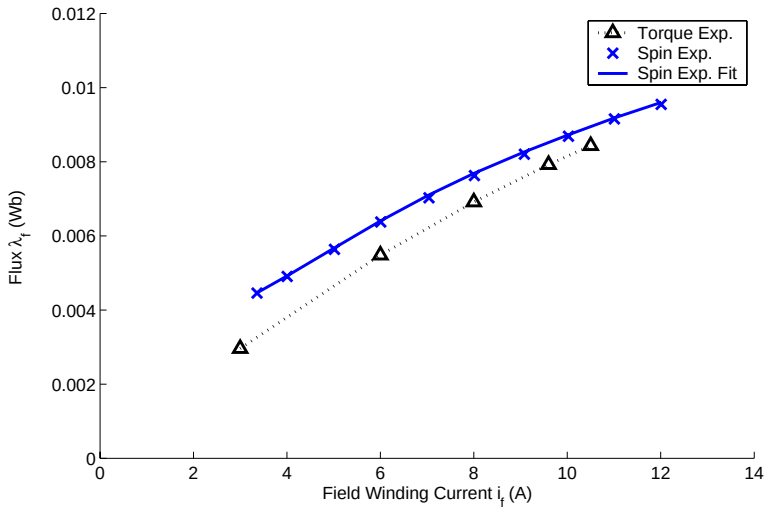


Figure 8.1: Plot of $\lambda_f$ as a function of $i_f$. Curves are shown for both the spin-test and the static torque test. The incremental mutual inductance $L_{mf}$ for a given $i_f$ is the slope of $\lambda_f$. The chorded mutual inductance is $\frac{\lambda_f}{i_f}$

the rotor flux level $\lambda_f$ could then be calculated from the peak torque $T$ using:

$$T = \frac{3}{2}\frac{poles}{2}\lambda_f i_q \tag{8.1}$$

where $i_q$ equals the dc current flowing through the armature. By definition, we know that the $i_d$ = 0 and $i_q$ equals the armature dc current because the stator flux and rotor flux are at a $90^\circ$ electrical angle when the peak torque occurs.

The data for $\lambda_f$ is plotted in Fig. 8.1. From looking at the data in Fig. 8.1, it is apparent that $L_{mf}$ (the slope of $\lambda_f$) decreases at higher $i_f$. This indicated that saturation was occurring at lower flux levels than anticipated. The exact cause is unclear, though it may be that the midsection of the stator near the field winding began to saturate and increased the reluctance of the magnetizing flux path.

The second method of measuring $L_{mf}$ was to spin the motor at constant speed, vary the flux level by changing $i_f$, and measure the resulting back-emf. Since the current is very small when running at constant speed, the drive voltage $V$ and the back-emf $E$ are nearly identical, and

$\lambda_f$ can be calculated from:

$$V \approx E = \omega_e \lambda_f \tag{8.2}$$

The results of the spinning measurement of $\lambda_f$ are also plotted in Fig. 8.1. There is good agreement between the two tests, and the slopes of the two curves are similar. Part of the difference between the results may be due to changes in the residual flux of the rotor. The residual flux is caused by remnant magnetization of the steel rotor, and present even when $i_f = 0$. These tests were conducted at different times, and it is possible that the residual flux of the motor was different during the two tests.

Both curves demonstrated a decrease in the mutual inductance as $i_f$ increased, and this has a negative impact on the efficiency because it increases the field winding excitation necessary to achieve a given flux level. A polynomial fit $\lambda_f(i_f)$ was made to the spin test data, and the resulting parameters were used in the core loss and efficiency calculations in this chapter. The chorded mutual inductance is calculated from this polynomial fit as:

$$L_{mf} = \frac{\lambda_f(i_f)}{i_f} \tag{8.3}$$

Fig. 8.2 plots the chorded mutual inductance as a function of $i_f$, and shows how at higher currents $L_{mf}$ decreases below the predicted value. At lower currents the chorded inductance is higher because of the residual flux (the chorded inductance goes to infinity at $i_f = 0$), however, the residual flux becomes a small percentage of the total flux at higher currents. For the efficiency tests described later on in this chapter, $i_f$ generally varied between 5 A and 14 A, so the decreased mutual inductance definitely had an impact on the results.

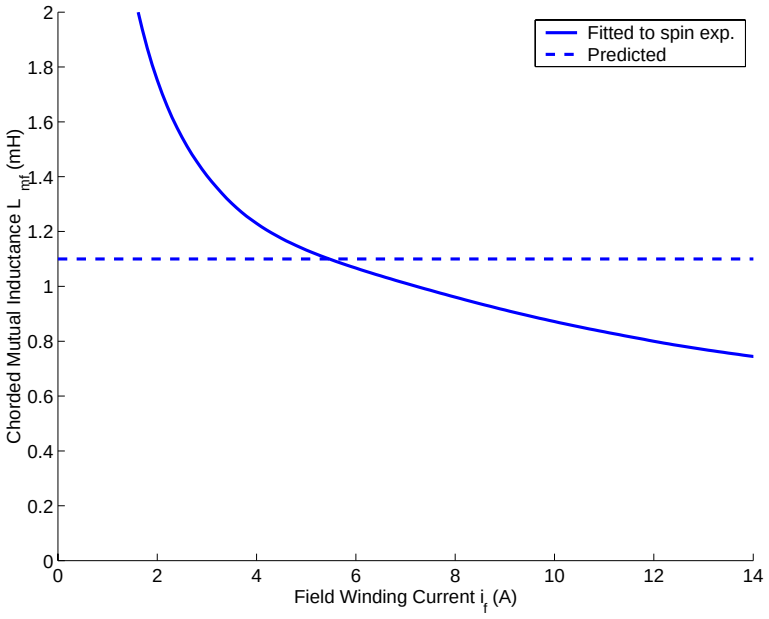


Figure 8.2: Plot of chorded mutual inductance as a function of $i_f$. The fitted curve is calculated from the spin-test data, and the predicted is calculated from the inductance equations presented in Chapter 3.

### 8.1.2 Effect of Temperature on Armature Resistance

During the efficiency testing, which is described in detail in Section 8.3, it was noted that the losses from the armature conduction loss were much higher than anticipated. Since the measured dc resistance at room temperature was close to the design value, and the Litz wire minimized the effects of current crowding from the ac currents and magnetic fields, it was suspected that the increased resistance was due to temperature rise in the conductors. Thermal tests were conducted with the motor at standstill to verify this hypothesis.

#### Measurement of Thermal Parameters

Figure 8.3 shows the thermal circuit used to model the system, and the circuit elements are described in Table 8.2. It should be noted that since radiation is negligible at the measured temperatures, the main conduction path between the rotor and the stator is through the bearings.

Therefore, thermal resistance $R\_s\_rotor$ is connected directly to $T\_stator$ and no path is made between the rotor and armature.

The thermal capacitances were calculated from the mass and material properties of the components. The thermal resistances were calculated from experimental measurements of stator temperature, armature resistance, and rotor temperature while the system was given varying thermal inputs $Q\_field$ and $Q\_arm$. Since the system was at standstill and dc current was used to generate the thermal inputs, there was no stator core, rotor core, or bearing losses. The stator temperature was measured with a thermocouple on the exterior of the housing, and rotor temperature was measured directly with an infrared thermocouple. The armature temperature was calculated from armature resistance measurements using the relationship:

$$R_a = R_o(1 + 0.00381(T\_arm - T\_air)) \tag{8.4}$$

where $R_o$ is the armature resistance at room temperature $T\_air$.

The thermal resistances were calculated one at a time. This was possible because the thermal capacitances were known and the thermal circuit had distinct time constants. Thermal resistance $R\_s\_air$ was calculated from the known total thermal capacitance and by measuring the rate at which the system would cool down. Since the rate of cool down was very slow and $T\_stator$, $T\_arm$ and $T\_rotor$ are at very similar temperatures, $R\_s\_air$ could be calculated independently.

Thermal resistance $R\_s\_arm$ was calculated by injecting heat $Q\_arm$ (by driving current through the armature) and raising the temperature $T\_arm$. Then the current was turned off, and the time constant at which $T\_arm$ decayed to $T\_stator$ was measured and used to deduce $R\_s\_arm$.

The stator to rotor thermal resistance was calculated by heating the stator with $Q\_field$

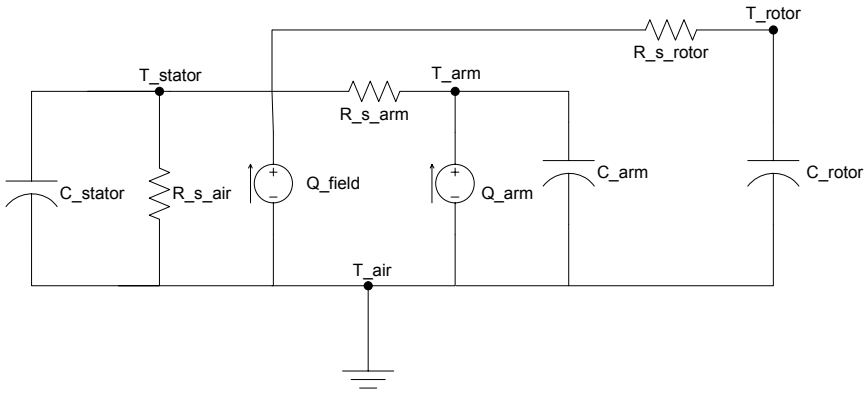


Figure 8.3: The equivalent circuit used to model the flywheel's thermal properties.

rapidly. Temperature $T\_stator$ would rise more rapidly than $T\_rotor$, and a temperature difference would be created. Then $Q\_field$ was turned off, and the time constant for the rise of $T\_rotor$ to $T\_stator$ was measured. Then $R\_s\_rotor$ could be calculated given the known thermal capacitances of $C\_stator$ and $C\_rotor$ in parallel.

From the parameters, we can see that the time constant of the armature (24 s) is much faster than that of the rotor (51 min.) or the stator (85 min.), and that $R\_s\_arm$ is smaller than the other two resistances. Thus, a good estimate of the armature temperature is:

$$T\_arm = Q\_armR\_s\_arm + T\_stator \tag{8.5}$$

During the 10 kW test where armature losses were 1 kW (see the loss breakdown in Figure 8.14), the equation implies that the armature temperature was $180°K$ higher than the stator, approaching $240℃$. With a thermal coefficient of resistance for copper of $0.00386\,\%/°K$, a $180°K$ rise in temperature corresponds to a 70% increase in armature conduction resistance.

Table 8.2: Thermal Circuit Elements

| **Circuit Element** | **Value** | **Description** |
|---|---|---|
| $C\_stator$ | $16524\,J/°K$ | Total thermal capacity of stator, field winding, and housing |
| $C\_arm$ | $130\,J/°K$ | Armature thermal capacitance |
| $C\_rotor$ | $4860\,J/°K$ | Rotor thermal capacitance |
| $R\_s\_air$ | $0.305\,°K/W$ | Thermal resistance between ambient air and the stator |
| $R\_s\_arm$ | $0.181\,°K/W$ | Thermal resistance between stator and the armature |
| $R\_s\_rotor$ | $0.630\,°K/W$ | Thermal resistance between stator and rotor |
| $Q\_field$ | — | Thermal input from field winding conduction losses |
| $Q\_arm$ | — | Thermal input from armature conduction losses |

**Analytical Calculation of $R\_s\_arm$**

The value for $R\_s\_arm$ can also be calculated analytically from a 1-dimensional thermal model. Fig. 8.4 diagrams a close-up cross-sectional view of the armature winding and stator, Fig. 8.5 shows the 1-dimensional model, and the parameters are described in Table 8.3. As shown in Fig. 8.4, each winding consists of 16 bundles of 7 Litz wound strands of AWG 33 magnet wire. The nominal dimensions of this rectangular compacted Litz wire is 0.188 inches wide by 0.045 inches tall, and has an copper circular mil area of 5900, equivalent to AWG 13 wire. The Dacron serve is a fiber wound around the bundle to improve its abrasion resistance, and it adds approximately 0.003 inches to the width and height of the bundle. It can be seen that there is quite a bit of space inside the rectangular cross-section of the wire that is void of copper and insulation, indicating a relatively low fill factor. From the circular mil area of the wire, it is calculated that the winding space is 51% copper, 3% insulation, and 46% void. These percentages include the voids in the gaps between adjacent wire bundles.

Although it is not evident from the 2-D diagram in Fig. 8.4, in calculating the thermal resistance for Litz wire it is necessary to remember that Litz wire is wound in a spiral pattern. For example, in the figure, the wire bundle that has all seven of its base strands drawn is located in the outer layer of bundles, away from the stator. However, if this cross-section is taken approximately 0.5" further along the wire, the same wire bundle will be on the inner layer of bundles nearest to the stator. Since the thermal conductivity of copper is 1000 times higher than the insulation, this means that the shortest thermal path for heat in the copper is to travel along the wire until it reaches a point where it is contacting the Dacron on the inner layer of wires. Then it only has to travel through one layer of polyimide insulation before it reaches the inner surface of the Dacron serve. In contrast, if the wires had *not* been wound in a spiral pattern, heat generated in the outer layer of

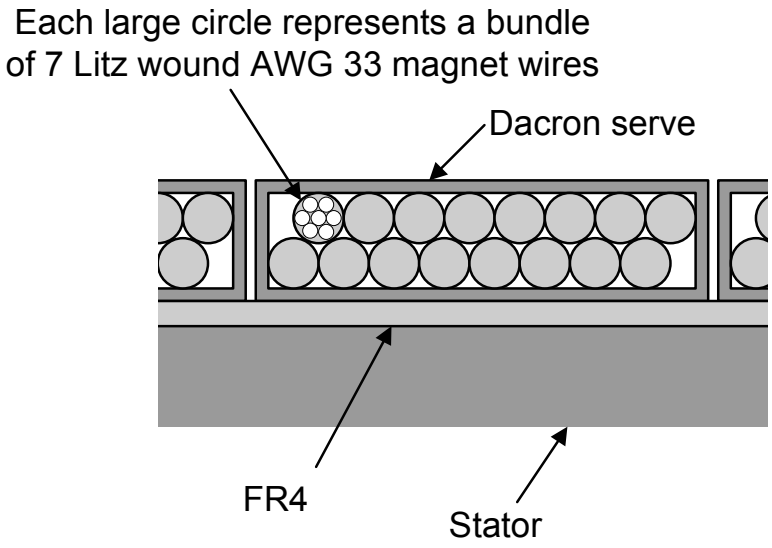


Figure 8.4: Close-up cross-sectional view of stator and Litz wire in armature.

wires would have to travel through at least 7 layers of polyimide insulation before it reached the Dacron serve.

The disadvantage of Litz wire's structure of many small wires is that the uneven outer surface reduces the overall contact area between the polyimide insulation and the Dacron serve. In the calculations of $R\_polyimide$, it was estimated that it reduced the surface area for thermal conduction by 1/10 as compared to a flat surface of the same width.

The calculation for the resistance $R\_Dacron$ was straightforward, however the calculation of resistance for $R\_FR4$ was complicated by the uneven surface of the laminations. This effect became evident during the removal of one of the earlier attempts at bonding the Litz wire to the stator. Some portions of the armature peeled off much more cleanly than others, indicating that the bond was uneven, probably due to uneven contact between the materials. For the purposes of calculating $R\_FR4$, it was estimated that the uneven surface area of the laminations reduced the surface area for thermal conduction by a factor 1/2 as compared to a smooth surface.

The analytically calculated value for $R\_s\_arm$ is 25% of the experimentally determined

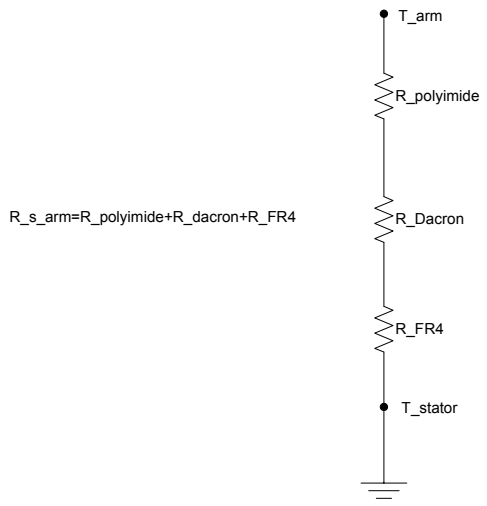


Figure 8.5: The 1-D model used to calculate R_s_arm.

Table 8.3: 1-Dimensional Thermal Model Parameters

| **Parameter** | **Value** | **Description** |
|---|---|---|
| | $0.00386\,\%/°K$ | Temperature coefficient of resistance for copper |
| | $0.12\frac{W}{m\,°K}$ | Thermal conductivity of polyimide magnet wire insulation) |
| | $0.25\frac{W}{m\,°K}$ | Thermal conductivity of Dacron nylon serve |
| | $0.3\frac{W}{m\,°K}$ | Thermal conductivity of FR4 |
| $R\_polyimide$ | $0.018\,°K/W$ | Thermal resistance from copper to Dacron serve inner surface |
| $R\_Dacron$ | $0.007\,°K/W$ | Thermal resistance from Dacron serve inner surface to FR4 inner surface |
| $R\_FR4$ | $0.021\,°K/W$ | Thermal resistance from FR4 inner surface to stator |
| $R\_s\_arm$ | $0.046\,°K/W$ | Thermal resistance from copper to inner surface of stator |

value. The difference can be attributed to uncertainty in the estimates of the thermal contact surface areas between the Litz wire and the Dacron serve and between the FR4 and the laminations.

## 8.2 Core Loss and Harmonic Loss

Measuring an individual loss component is a demanding task, and this is even more so for losses that occur on the rotor. To measure the rotor losses caused by armature current time harmonics, it was necessary to conduct two different types of core loss tests and to calculate the difference in the results.

The first test for measuring the core loss was to maintain a constant flux level with the field winding, and then let the flywheel spin down with the inverter disabled. By using the rotor's moment of inertia, the losses can be calculated by measuring the rate at which the rotor spins down. In these spin-down tests, no current flows through the armature and the inverter is not switched, therefore the only losses are:

1. Bearing drag
2. Stator core loss

The results for the spin-down tests are in presented in Section 8.2.1.

The second method of measuring core loss was to spin the flywheel at a constant speed and to measure the input power needed to keep the flywheel spinning at various flux levels. Since there is no net mechanical change in energy, the input power is equal to the losses in the system. In these constant-speed tests, the losses are the sum of:

1. Bearing drag
2. Stator core loss
3. Conduction loss of the fundamental current
4. Inverter switching loss

5. Rotor time harmonic loss
6. Stator harmonic current conduction loss

Of these loss components, the stator core loss and rotor time harmonic losses dominate. Since there is very little current flowing in the armature, the conduction loss of the fundamental, inverter switching loss, and stator harmonic conduction loss are all small. The results for the constant speed tests are presented in Section 8.2.2.

Subtracting the spin-down data from the constant-speed data results in the sum of loss components of the constant-speed test that are *not* present in the spin-down test, namely:

1. Conduction loss of the fundamental current
2. Inverter switching loss
3. Rotor time harmonic loss
4. Stator harmonic current conduction loss

Again, the rotor time harmonic loss is the dominant term. Since the spin-down test and the constant-speed tests are done at different speeds and flux levels, it is necessary to fit a model to the test data before it is possible to 'subtract' one set of results from another. The details of the model fitting and calculations are described in the next three sub-sections.

### 8.2.1 Spin-down Tests

The results of the spin-down tests are plotted in Fig. 8.6. A bearing and core loss model of the form:

$$P_{bear} = b_1\omega_e + b_2\omega_e^2 \tag{8.6}$$

$$P_{hys} = B^2\omega_e c_1 \tag{8.7}$$

$$P_{eddy} = B^2\omega_e^2 c_2 \tag{8.8}$$

$$P_{spinloss} = P_{bear} + P_{hys} + P_{eddy} \tag{8.9}$$

Table 8.4: Loss Coefficients for Spindown Test Fit

| **Loss Coefficient** | **Value** |
|---|---|
| $b_1$ | $1.19 \times 10^{-3} \frac{\text{W}}{\text{rad/s}}$ |
| $b_2$ | $24.8 \times 10^{-6} \frac{\text{W}}{(\text{rad/s})^2}$ |
| $c_1$ | $26.6 \times 10^{-3} \frac{\text{W}}{\text{T}^2 \cdot \text{ rad/s}}$ |
| $c_2$ | $7.60 \times 10^{-6} \frac{\text{W}}{\text{T}^2 \cdot (\text{rad/s})^2}$ |

was fit to the spin-down data, where $B$ is the peak ac flux density, $\omega_e$ is the rotor speed in electrical radians, and $b_1$, $b_2$, $c_1$, and $c_2$ are bearing and core loss coefficients. The peak ac flux density is the amplitude of the maximum flux variation in the stator. For example, a peak flux density of $0.8$ T with a minimum flux density of $0.2$ T would imply a peak ac flux density of $0.3$ T. The term $P_{bear}$ represents the bearing loss, and $P_{hys}$ and $P_{eddy}$ represent the hysteresis and eddy current loss components of the stator core loss. The resulting fitted parameters are shown in Table 8.4.

A breakdown of the losses from the fitted model for the 0.22 T spin-down test is shown in Fig. 8.7. Comparing the measured stator core loss to the predicted reveals that the measured losses are larger by a constant factor of four. This is illustrated by Fig. 8.8 which plots the measured losses and the predicted losses multiplied by four. The difference between the measured and predicted suggests that there may be an additional aspect of the stator core loss that was not modelled in the design. It is noted that the design is not core loss dominated, so the impact on efficiency is not extreme.

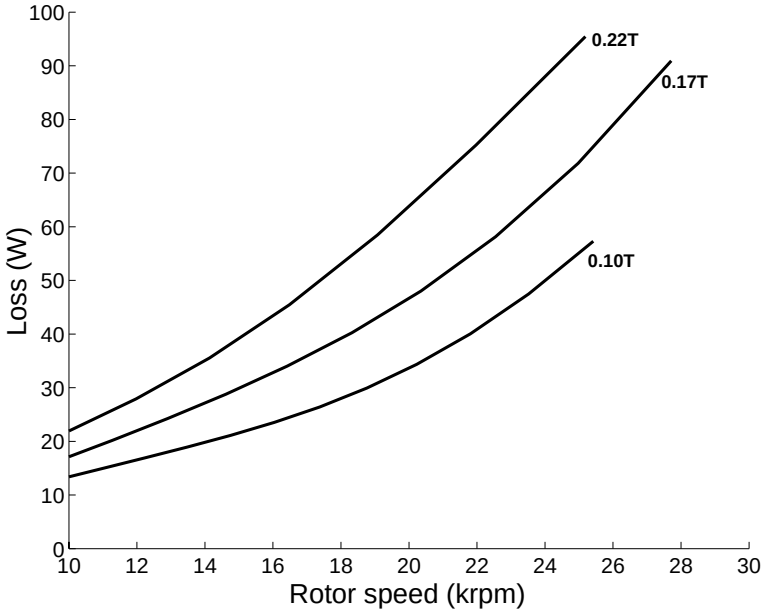


Figure 8.6: Plot of spin-down core loss test results versus speed for three peak ac flux density levels.

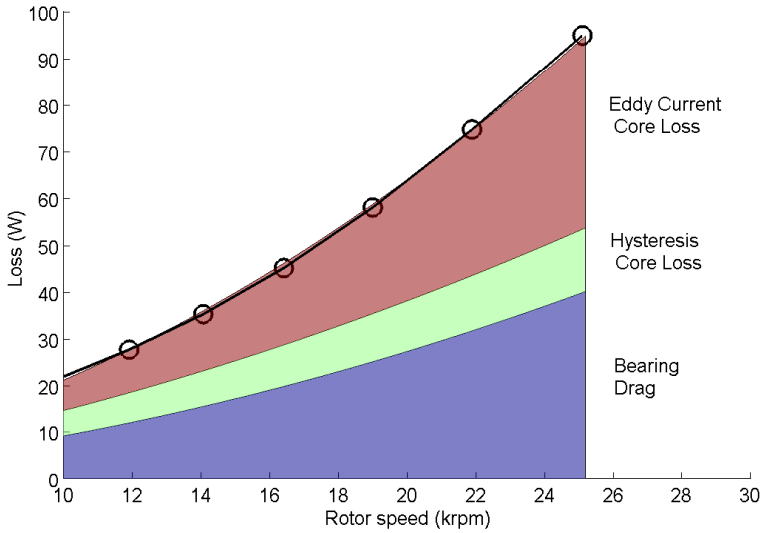


Figure 8.7: Breakdown of loss for 0.22 T spin-down test. The loss components are determined from the fitted model. The measured data is shown by the solid line with circles.

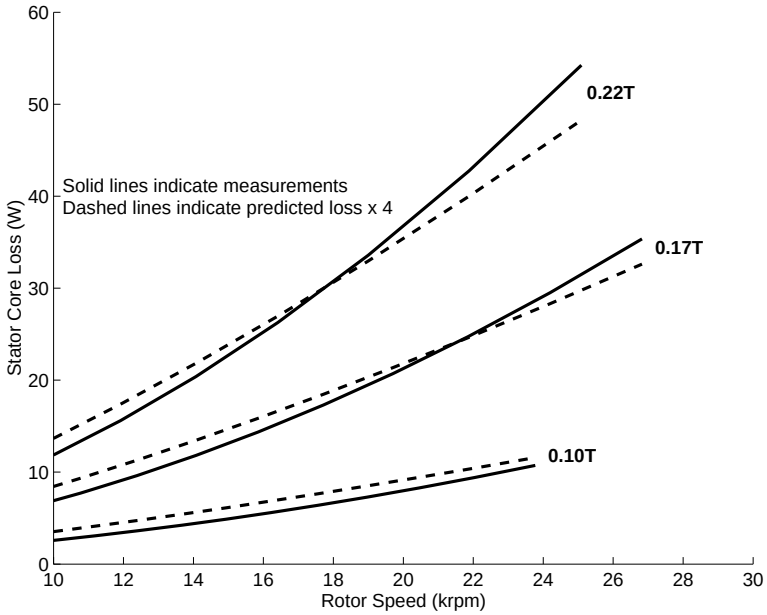


Figure 8.8: Comparison of measured stator core loss to predicted stator core loss. The solid line indicates the stator core loss component of the spin-down test data, and the dashed line indicates the predicted losses multiplied by 4.0.

### 8.2.2 Constant-Speed Tests

The results of the constant-speed tests are shown in Fig. 8.9, and a reasonable fit to the data can be made using the following model.

$$P_{bear} = b_1\omega_e + b_2\omega_e^2 \tag{8.10}$$

$$P_1 = B^2\omega_e d_1 \tag{8.11}$$

$$P_2 = B^2\omega_e^2 d_2 \tag{8.12}$$

$$P_3 = Bw_e d_3 \tag{8.13}$$

$$P_{constloss} = P_{bear} + P_1 + P_2 + P_3 \tag{8.14}$$

The same bearing coefficient values $b_1$ and $b_2$ determined by the fit to the spindown test data (shown in Table 8.4) are also used here. The terms $d_1$, $d_2$, and $d_3$ are loss coefficients. Since

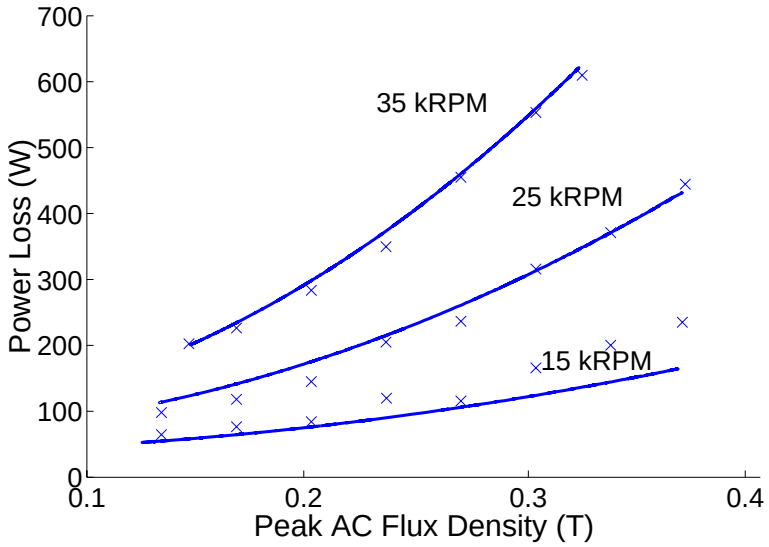


Figure 8.9: Plot of constant-speed core loss tests versus peak ac flux density for various speeds. A subset of the measurements used to generate the parameters for the model is indicated by the x's, and the solid line represents the fitted model.

multiple loss components have the same growth rates with respect to $B$ and $\omega_e$, the loss terms $P_1$, $P_2$, and $P_3$ do not correspond to individual loss components. The term $P_1$ corresponds to stator hysteresis core loss and conduction loss of the fundamental, $P_2$ corresponds to the stator eddy current core loss and the rotor time harmonic loss, and $P_3$ corresponds to switching loss and stator harmonic current conduction loss. Figure 8.9 shows the results from this test along with the fitted model, and the values of the fitted coefficients are shown in Table 8.5.

### 8.2.3 Harmonic Loss Measurements

As outlined at the beginning of Section 8.2, the harmonic loss measurements are calculated from the difference in results of the constant-speed and spin-down tests. These four loss components are repeated here from the beginning of this section:

1. Conduction loss of the fundamental current
2. Inverter switching loss
3. Rotor time harmonic loss

Table 8.5: Loss Coefficients for Constant Speed Test Fit

| **Loss Coefficient** | **Value** |
|---|---|
| $b_1$ | $1.19 \times 10^{-3} \frac{\text{W}}{\text{rad/s}}$ |
| $b_2$ | $24.8 \times 10^{-6} \frac{\text{W}}{(\text{rad/s})^2}$ |
| $d_1$ | $1.40 \times 10^{-3} \frac{\text{W}}{\text{T}^2 \cdot \text{ rad/s}}$ |
| $d_2$ | $11.2 \times 10^{-6} \frac{\text{W}}{\text{T}^2 \cdot (\text{rad/s})^2}$ |
| $d_3$ | $8.97 \times 10^{-3} \frac{\text{W}}{\text{T} \cdot (\text{rad/s})}$ |

4. Stator harmonic current conduction loss

These losses are dominated by the rotor time harmonic losses. The total loss $P_{harm}$ of these four components is plotted in the two graphs of Fig. 8.10.

The upper graph plots the harmonic loss as a function of speed, for constant flux levels. The harmonic loss $P_{harm}$ was calculated using:

$$P_{harm}(\omega_e) = P_{constloss,mod}(\omega_e) - P_{spin,exp}(\omega_e) \tag{8.15}$$

where $P_{constloss,mod}$ is the model fitted to the constant-speed tests in equations (8.10)-(8.14), and $P_{spin,exp}(\omega_e)$ is the measured data for the spin-down experiments. Note that $B$ is held constant and $\omega_e$ varies.

The lower graph plots the harmonic loss as a function of flux level, for constant speeds. The harmonic loss $P_{harm}$ was calculated using:

$$P_{harm}(B) = P_{constloss,exp}(B) - P_{spin,mod}(B) \tag{8.16}$$

where $P_{constloss,exp}$ is the measured data from the constant-speed experiments, and $P_{spin,mod}$ is the model fitted to the spin-down tests in equations (8.6)-(8.9). Note that now $\omega_e$ is held constant and $B$ varies.

The validity of these calculations for the harmonic loss components must be considered carefully since they are calculated from fitted data. From the two graphs, we can see that the predicted and measured harmonic losses have reasonably good agreement for both calculation methods. This means that it did not matter whether a fitted model was used in place of spin-down test data, or if a fitted model was used in place of constant-speed test data. This is as expected, since the spin-down and constant-speed tests were performed over overlapping speed and flux ranges and the fitted models were for the most part used to interpolate the data. Since the data is being interpolated, any reasonable fitted loss model that produces a good match would lead to comparable results for the harmonic losses. Thus the results are independent of the loss model chosen for equations (8.6-8.9) and (8.10-8.14), as they should be.

A breakdown of the losses for the $0.22$ T test in the upper graph of Fig. 8.10 is shown in Fig. 8.11, which compares the measured to the predicted losses. The predicted inverter switching losses are based on manufacturer data, and the harmonic current and rotor harmonic losses are calculated using the methods described in the Sections 6.1 and 6.2. The figure shows that the dominant harmonic loss component is the rotor harmonic losses.

Figures 8.10 and 8.11 demonstrate that there is good agreement between the losses predicted by the analysis in Chapter 6 and the measured losses. The measured and predicted losses grew at a similar rate with respect to both speed and flux level. Moreover, agreement between the measured and predicted rotor harmonic losses also confirms that low rotor losses have been achieved. Interpolations of the measured data indicates that at the $30$ krpm, $9.4$ kW, $0.19T$ oper-

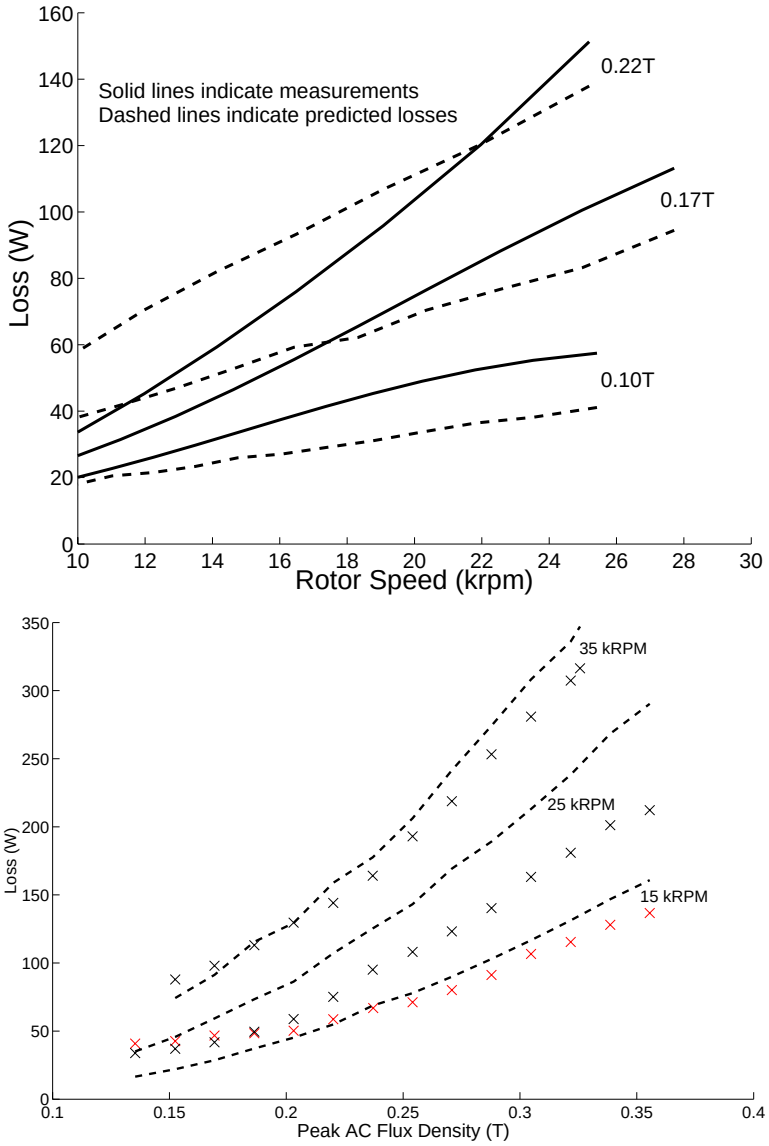


Figure 8.10: Plots of inverter and harmonic losses. In the upper graph, measured losses (solid lines) are calculated from the spindown test data and the fitted model for the constant speed test. Predicted losses calculated analytically are indicated with the dashed lines. The flux levels correspond to the flux levels in Fig. 8.6. In the lower graph, measured losses (x's) are calculated from the results of the constant speed tests and the fitted model for the spindown tests. The dashed lines indicate the predicted losses.

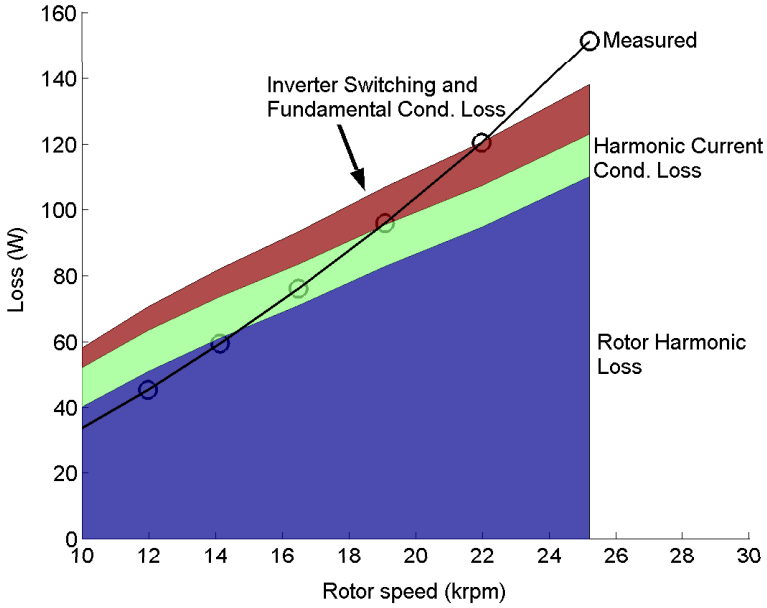


Figure 8.11: Breakdown of predicted harmonic and inverter losses compared to measurements. The solid line is the same as the $0.22$ T line in the upper graph of Fig. 8.10, and the shaded areas represent the components of the predicted loss for this test.

ating point, rotor losses are $112W$, compared to a designed value of $100W$ calculated in Table 6.1. This operating point corresponds to the worst-case operating point of the $30$ krpm - $60$ krpm experiments discussed in the next section, and represents only 1.2% of the output power. As mentioned in section 2.2, low rotor loss is one of the most important and difficult requirements to meet in a flywheel energy storage system. Meeting this design goal demonstrates that a high-speed homopolar inductor motor with a solid-steel rotor can have low rotor losses even while running under six-step excitation.

## 8.3 Efficiency Measurements

The system efficiency was measured by cycling power into and out of the flywheel over a 2:1 speed range. Fig. 8.12 shows an example of the phase current and voltage during one of these tests. Data from an efficiency test consisting of accelerations and decelerations between

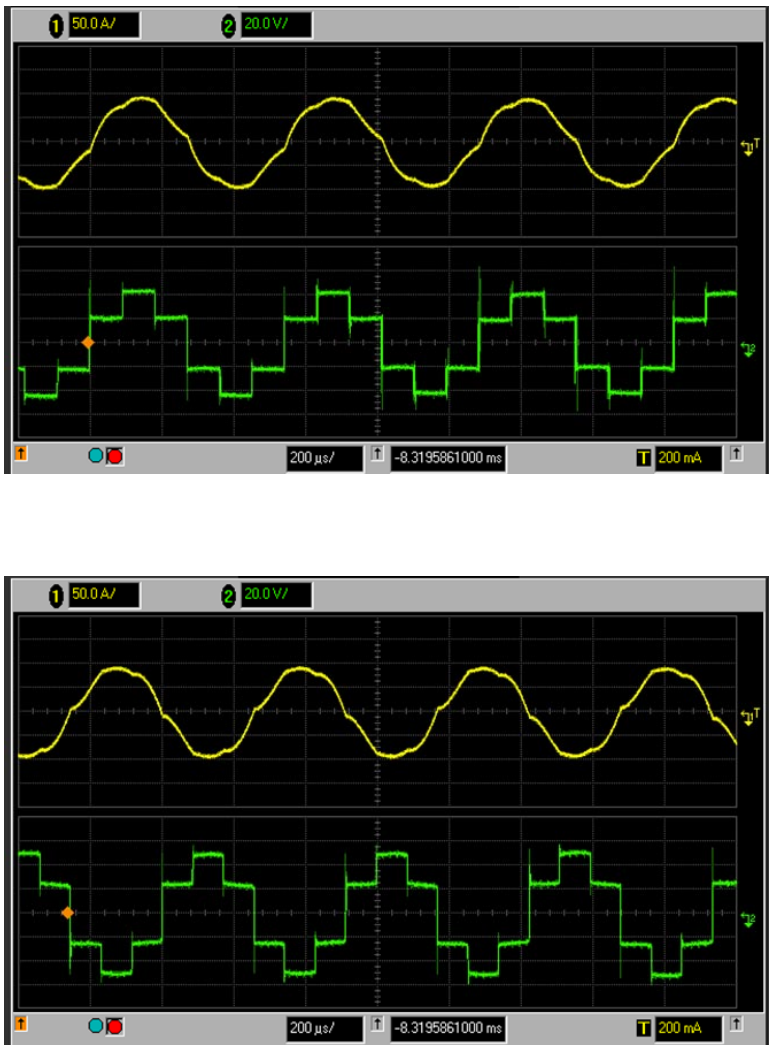


Figure 8.12: Oscilloscope traces of phase current (upper traces) and line-to-neutral voltage (lower traces) at 28 krpm during a 90 A, 45 V, 6 kW charge (upper photo) and discharge (lower photo).

30,000 rpm and 60,000 rpm while charging and subsequently discharging electrical power at a 9.4 kW power level is shown in Fig. 8.13. The electrical power is shown in the top graph, the rotor speed profile in the second, and the measured efficiency in the bottom graph. Since the starting and ending rotor speeds for the test are identical, the net mechanical power during the test is zero. Therefore the integral of electrical power $P_e$ over the test is equal to the loss, and the average efficiency over the entire test can be calculated as:

$$\eta_{avg} = 1 - \frac{\int_0^T P_e \, \mathrm{d}t}{\int_0^T |P_e| \, \mathrm{d}t} \tag{8.17}$$

The advantage of using the above expression for $\eta_{avg}$ is that it can be calculated directly and accurately from voltage and current measurements of the dc bus, and it includes all the losses that occur in the entire system, i.e. the inverter, the field winding dc-dc converter, and the motor/generator. The average efficiency for this particular test and other tests run between 15 krpm-30 krpm and 30 krpm-60 krpm is shown in Fig. 8.15.

Although the above measurements reveal the average efficiency of the flywheel during the test, they do not reveal the efficiency at any single operating point. To calculate the efficiency for a trajectory as shown in the bottom graph of Fig. 8.13, it was necessary to use the rotor inertia $J$ and these expressions for mechanical power and efficiency:

$$P_m = J\omega_m\dot{\omega}_m \tag{8.18}$$

$$\eta = 1 - \frac{|P_e - P_m|}{|P_e|} \tag{8.19}$$

to calculate the efficiency for each point in time of the test. A 0.3 s long moving time average was applied to generate the efficiency data in the bottom plot of Fig. 8.13.

A breakdown of the loss components was calculated using the core loss model developed from the core loss tests and the harmonic loss equations. A plot of the loss breakdown for one

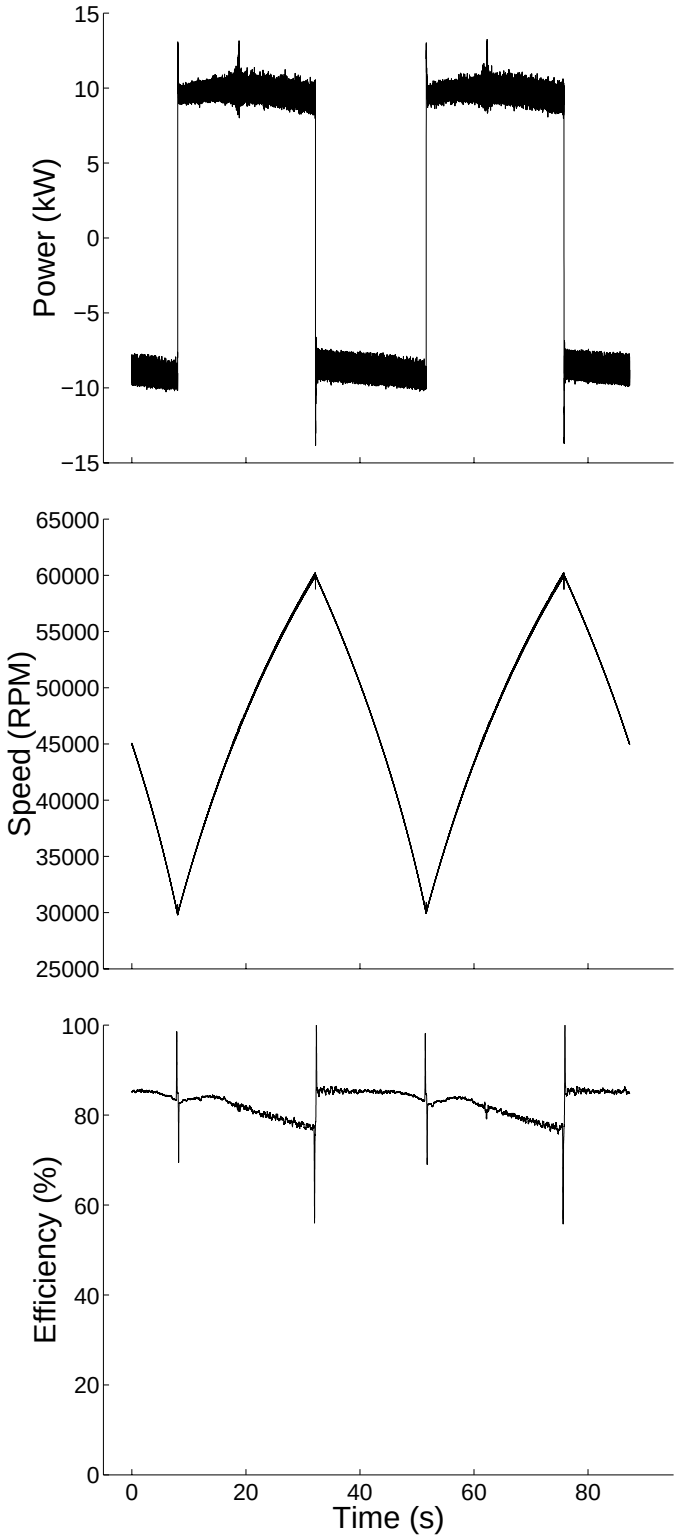


Figure 8.13: Plots of flywheel system input power, rotor speed, and system efficiency versus time during a 9.4 kW, 15 krpm - 30 krpm efficiency test.

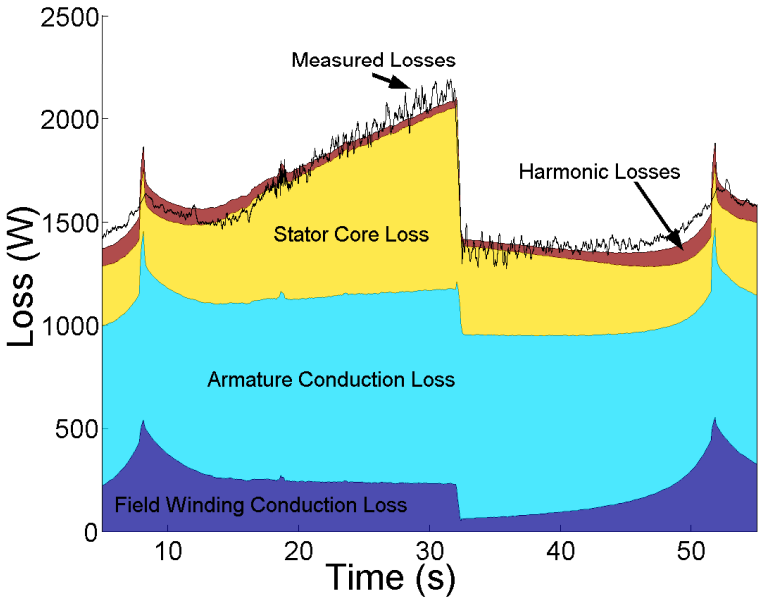


Figure 8.14: Loss breakdown for $9.4\,kW$, 30 krpm - 60 krpm efficiency test. The solid line indicates the total measured loss, and the shaded areas indicate the various loss components (rotor harmonic and current harmonic conduction losses are grouped together as 'harmonic losses.')

cycle of the efficiency test is shown in Fig. 8.14, and Table 8.6 summarizes the data for this particular test. From the figure, it can be seen that the loss model provides a good fit to the data. The armature conduction loss is the largest portion of the loss at $53.3\%$, followed by the core loss at $30.0\%$, and the field winding conduction loss at $13.4\%$. Notably, the rotor losses are less than 50 W, and the total harmonic losses contribute less than $4\%$ of the total loss.

Fig. 8.15 plots the measured efficiency for several power levels over the 15 krpm-30 krpm and 30 krpm-60 krpm speed ranges, conducted with voltages $V$ of $50\,V$ and $100\,V$, respectively. Also plotted are results from the loss model fitted to the data. An average complete system efficiency of 83% was achieved at $9.4$ kW over the 30 krpm-60 krpm speed range. This included inverter losses, dc-dc converter losses, and motor/generator losses.

Table 8.6: Efficiency Test Data

| | |
|---|---|
| Average Power $\lvert P_e \rvert$ | $9.4\,\text{kW}$ |
| Speed Range | $30\,\text{krpm}$-$60\,\text{krpm}$ |
| Average Eff. | $82.8\%$ |

| Loss Breakdown from Fitted Model (as percentage of total measured loss) | |
|---|---|
| Armature Cond. | $53.3\%$ |
| Field Wind. Cond. | $13.4\%$ |
| Stator Core Loss | $30.0\%$ |
| Rotor Harm. Loss | $3.1\%$ |
| Harm. Curr. Cond. | $0.2\%$ |
| Total | $99.8\%$ |

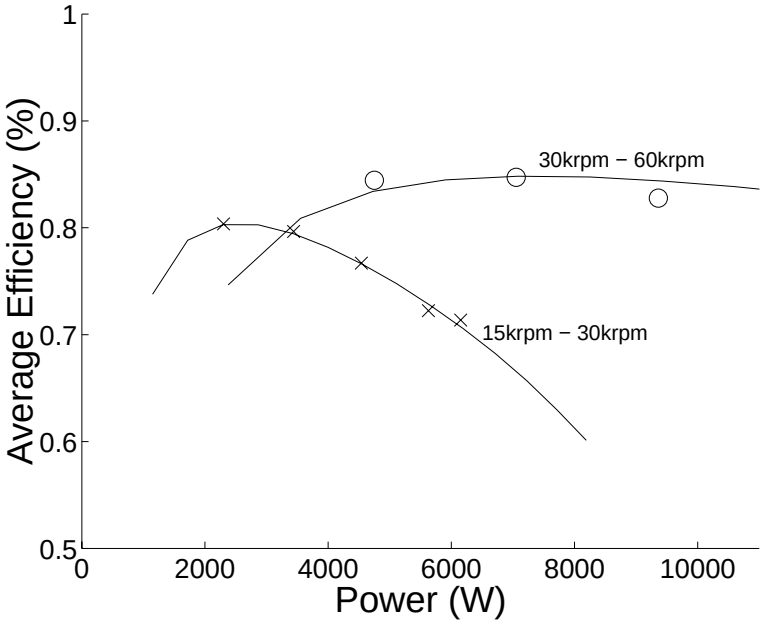


Figure 8.15: Measured average efficiencies $\eta_{avg}$ for $15\,\text{krpm}$-$30\,\text{krpm}$ tests (x's) and $30\,\text{krpm}$-$60\,\text{krpm}$ tests (o's). Solid lines indicate results from the fitted model.

## 8.4 Analysis of Results

Comparing the fitted loss model to the design model presented in Section 3.2.5 reveals why the measured efficiencies are lower than those predicted by the design optimization. In order of importance, the reasons are:

1. Armature resistance 80% higher than the measured dc value at room temperature. This was due to an unexpectedly high temperature rise in the windings, and was confirmed by the thermal model.

2. The motor was not running at its designed operating point at higher speeds. The efficiency graph at the bottom of Fig. 8.13 reveals that the efficiency dropped during charging as the flywheel speeds up. This was unexpected, because the design calculations predicted that efficiency would stay relatively constant over the entire speed range. The cause was a phase delay in the sampling from the analog filter used to process the current measurements. The result of the phase delay was such that at speeds above 40 krpm, instead of running at unity power factor, the flywheel would run at a leading power factor while charging, and a lagging power factor while discharging. This caused extra core loss, field winding conduction loss, and reduced the power output for a given armature current during charging. The phase delay was confirmed by viewing the armature voltage and currents on the oscilloscope.

3. The mutual inductance $L_m$ gradually dropped by as much as 30% as the field winding current increased, as described in section 8.1.1. The effect of this was to increase the field winding losses.

4. The core loss grew at a higher rate with respect to frequency than predicted, as de-

scribed in section 8.2.

To improve the performance in future designs, the optimization process should incorporate the conduction, core loss, and harmonic loss models generated from the experimental data.

# Chapter 9

# Conclusion

The design and experimental results from an integrated flywheel energy storage system have been presented in this thesis. An integrated flywheel system has advantages over other flywheel designs, and the homopolar inductor motor/generator is particulary well-suited to this flywheel configuration.

A prototype integrated flywheel system was built, and experimental results of the system efficiency were presented. Significantly, a breakdown of losses was made and it was shown that the losses due to six-step harmonics were in good agreement the analytical calculations.

Measurements of system efficiency, which included losses in the inverter, dc-dc converter, and motor generator were made. An average system efficiency of 83% was achieved at 9.4 kW over the 30 krpm-60 krpm speed range. Extrapolating the loss model fit to this data predicts that $88\%$ efficiency could be achieved for a 30 kW, 50 krpm-100 krpm test.

# Bibliography

[1] *Metallic Materials and Elements for Aerospace Vehicle Structures*. Number MIL-HDBK-5H. Department of Defense, 1998.

[2] S.M. Aceves and J.R. Smith. ‘optimum flywheel sizing for parallel and series hybrid vehicles’. In *Lawrence Livermore National Laboratory Preprint UCRL-JC126259*, 1996.

[3] M. Ahrens, L. Kucera, and R. Larsonneur. ‘performance of a magnetically suspended flywheel’. *IEEE Transactions on Control Systems Technology*, 4:495–501, 1996.

[4] R.C. Balch, A. Burke, and A.A. Frank. ‘the affect of battery pack technology and size choices on hybrid electric vehicle performance and fuel economy’. In *Sixteenth Annual Battery Conference on Applications and Advances. Proceedings of the Conference*, pages 31–6, 2001.

[5] D.A. Bender and P.K. Snyder. Dc power management with a high performance flywheel. In *Electrical Energy Storage Systems Applications and Technologies (EESAT) Conference Proceedings*, 2002. See also www.afstrinity.com.

[6] A.R. Bergen and V. Vittal. *Power Systems Analysis*. Prentice-Hall, 1999.

[7] A. Boglietti, P. Ferraris, M. Lazzari, and F. Profumo. Energetic behavior of induction motors

fed by inverter supply. In *Conference Record of the IEEE IAS Annual Meeting*, pages 331–335, 1993.

[8] A. Boglietti, P. Ferraris, M. Lazzari, and F. Profumo. Energetic behavior of soft magnetic materials in the case of inverter supply. *IEEE Transactions on Industry Applications*, 30:1580–1587, Nov. 1994.

[9] A. Burke. 'ultracapacitors: why, how, and where is the technology'. *Journal of Power Sources*, 91:37–50, 2000.

[10] J.H. Beno et al. 'end-of-life design for composite rotors'. *IEEE Transactions on Magnetics*, 37:2843–289, 2001.

[11] P.P. Acarnley et al. An integrated flywheel/machine energy store for road vehicles. In *Colloquium on New Topologies for Permanent Magnet Machines*, volume No. 1997/090, pages 9/1–6. IEE, 1997.

[12] A.E. Fitzgerald, C. Kingsley, and S.D. Umans. *Electric Machinery*. New York: McGraw-Hill, Inc., 1990.

[13] G. Genta. *Kinetic Energy Storage*. Boston: Butterworths, 1985.

[14] Jin He and Feng Lin. A high frequency high power igbt inverter drive for a 45hp/16,000 rpm brushless homopolar inductor motor. In *Conference Record of the IEEE IAS Annual Meeting*, pages 9–15, 1995.

[15] R. Hebner, J. Beno, and A. Walls. Flywheel batteries come around again. *IEEE Spectrum*, 39(4):46–51, April 2002.

[16] J.D. Herbst, R.F. Thelen, and W.A. Walls. ‘status of the advance locomotive propulsion system (alps) project’. In *High Speed Ground Transportation Association*, May 2000.

[17] M. Hippner and R.G. Harley. High speed synchronous homopolar and permanent magnet machines comparative study. In *Conference Record of the IEEE IAS Annual Meeting*, pages 74–78, 1992.

[18] R. Hockney and C. Driscoll. Powering of standby power supplies using flywheel energy storage. In *International-Telecommunications-Energy-Conference (INTELEC)*, pages 105–109. See also www.beaconpower.com, 1997.

[19] H. Hofmann. *High-Speed Synchronous Reluctance Machine for Flywheel Applications*. PhD thesis, University of California, Berkeley, 1998.

[20] H. Hofmann and S.R. Sanders. High-speed synchronous reluctance machine with minimized rotor losses. *IEEE Transactions on Industry Applications*, 36:531–539, 2000.

[21] O. Ichikawa, A. Chiba, and T. Fukao. Development of homo-polar type bearingless motors. In *Conference Record of the IEEE IAS Annual Meeting*, pages 1223–1228, 1999.

[22] D.R. Kelsall. ‘pulsed power provision by high speed composite flywheel’. In *Proceedings of the IEE Pulsed Power Symposium*, 2000.

[23] P. Kokotovic, H.K. Khalil, and J. O’Reilly. *Singular Perturbation Methods in Control*. London: Academic Press, 1986.

[24] E. Kramer. *Dynamics of Rotors and Foundations*. New York: Springer-Verlag, 1993.

[25] P.C. Krause, O. Wasynczuk, and S.D. Sudhoff. *Analysis of Electric Machinery and Drive Systems*, pages 48–53. Wiley-Interscience.

[26] L.B. Lave and H.L. Maclean. ‘an environmental-economic evaluation of hybrid electric vehicles: Toyota’s prius vs. its conventional internal combustion engine corolla’. *Transportation Research Part D*, 7:155–162, 2002.

[27] M. Lazarewicz. A description of the beacon power high energy and high power composite flywheel energy storage systems. In *Electrical Energy Storage Systems Applications and Technologies (EESAT) Conference Proceedings*, 2002. See also www.afstrinity.com.

[28] J.R. Melcher. *Continuum Electromechanics*. Cambridge, MA: MIT Press, 1981.

[29] R.F. Nelson. ‘power requirements for batteries in hybrid electric vehicles’. *Journal of Power Sources*, 91:2–26, 2000.

[30] A. Ohnsman. ‘toyota prius turns a profit’. Bloomberg News, December 20, 2001.

[31] G.P. Rao, Jr. J.L. Kirtley, D.C. Meeker, and K.J. Donegan. Hybrid permanent magnet/homopolar generator and motor. U.S. Patent 6,097,124, Aug. 2000.

[32] S. Richey. Cleansource2 battery-free energy storage: Theory of operation. In *Electrical Energy Storage Systems Applications and Technologies (EESAT) Conference Proceedings*, 2002. See also www.activepower.com.

[33] M.S. Sarma. *Electric Machines: Steady-State Theory and Dynamic Performance*. New York: West Publishing Company, 1994.

[34] M.K. Senesky. Control of a synchronous homopolar machine for flywheel applications. M.S. thesis, University of California, Berkeley, 2003.

[35] M. Siegl and V. Kotrba. Losses and cooling of a high-speed and high-output power homopo-

lar inductor alternator. In *IEE International Conference on Electrical Machines and Drives*, pages 295–299, Sept. 1991.

[36] J.W. Smith. Tolerance rings. *Industry Applications Magazine*, 8(5):74–82, Sept-Oct 2002.

[37] D. Townley. Introducing pentadyne power flywheel energy storage system. In *Electrical Energy Storage Systems Applications and Technologies (EESAT) Conference Proceedings*, 2002. See also www.pentadyne.com.

[38] P. Tsao, M. Senesky, and S.R. Sanders. A synchronous homopolar machine for high-speed applications. In *Conference Record of the IEEE IAS Annual Meeting*, pages 406–416, 2002.

[39] K. Venkatachalam, C.R. Sullivan, T. Abdallah, and H. Tacca. Accurate prediction of ferrite core loss with nonsinusoidal waveforms using only steinmetz parameters. In *IEEE Workshop on Computers in Power Electronics,Mayaguez, Puerto Rico*, 2002.

[40] R. Wagner and R. Jansen. Flywheel technology development at the nasa glenn research center. In *Electrical Energy Storage Systems Applications and Technologies (EESAT) Conference Proceedings*, 2002.

[41] R.A. Weinstock, P.T. Krein, and R.A. White. ‘optimal sizing and selection of hybrid electric vehicle components’. In *Record of the 24th Annual IEEE Power Electronics Specialists Conference*, pages 251–6, 1993.

# Appendix A

# Prototype Drawings

Most of the mechanical drawings made for the flywheel system have been included in this appendix. The computer file for each drawing is indicated on the drawing and included on the CD-ROM described in Appendix B. The drawings were made in Autosketch 6.0, which is available from the Autodesk company.

Please note that the drawing scales indicated are not accurate because the drawings have been scaled to 75% of the original size to fit the format of the thesis. The dimensions indicated are still accurate.

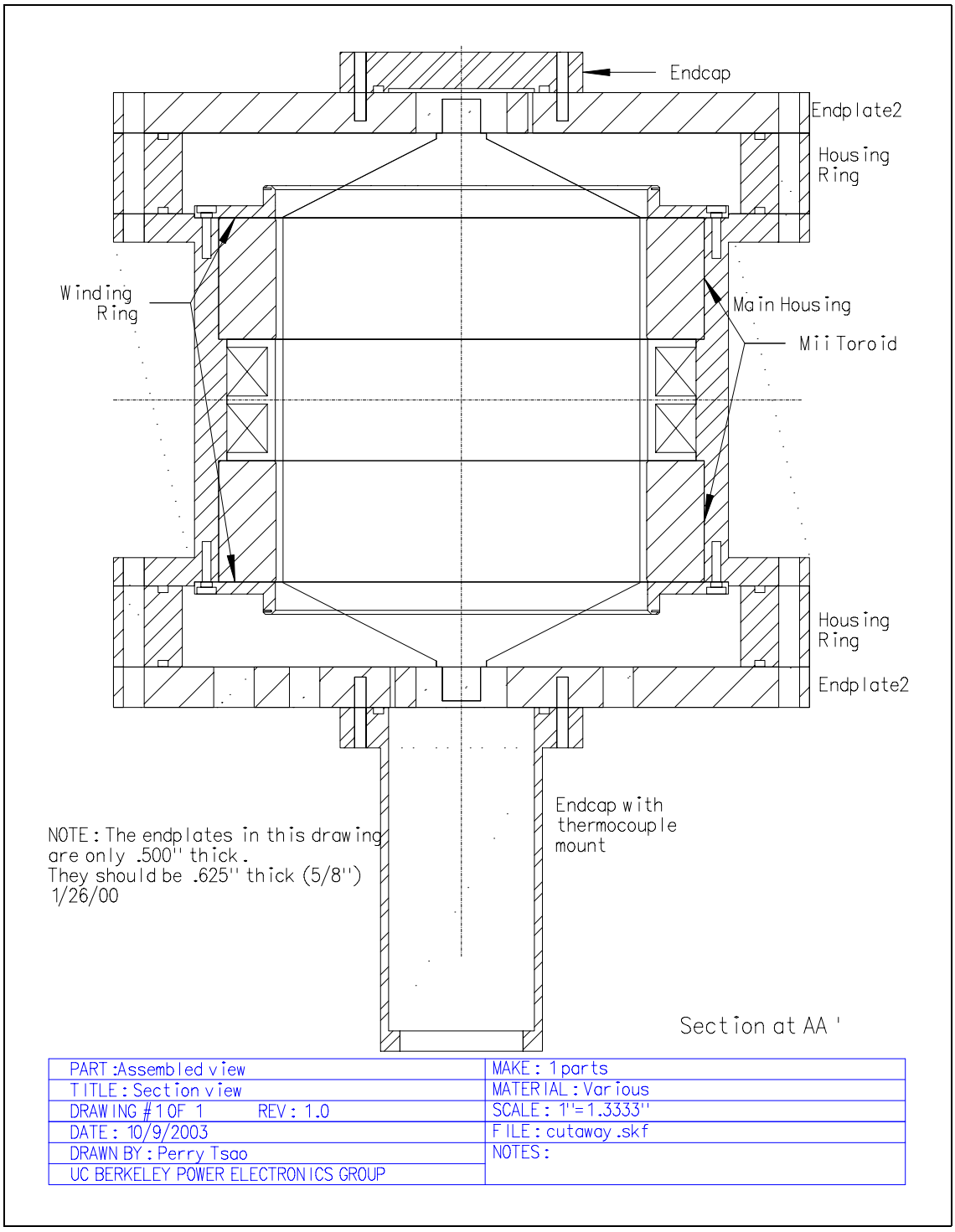


Figure A.1: Cutaway view of assembled flywheel system.

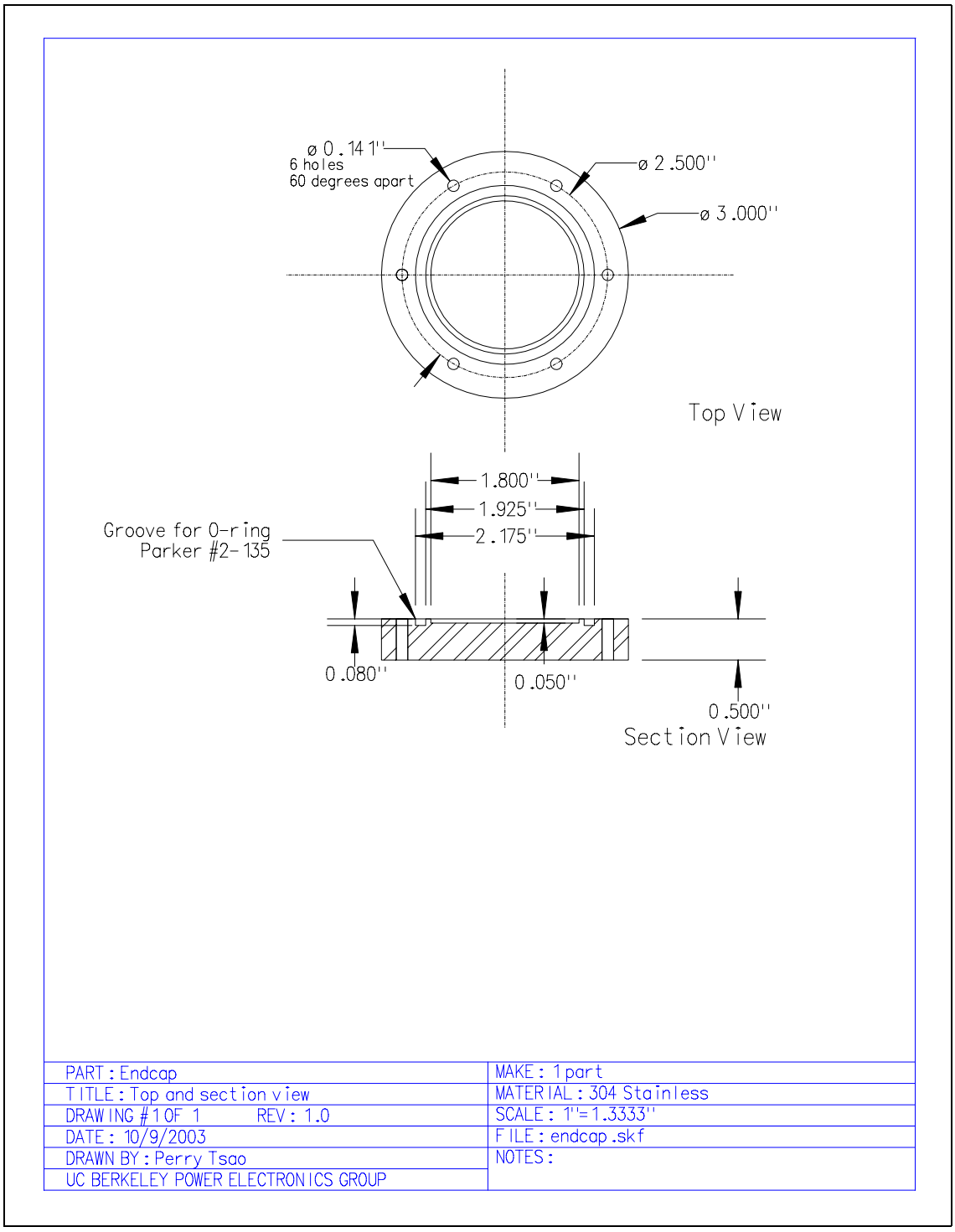


Figure A.2: Drawing of endcap.

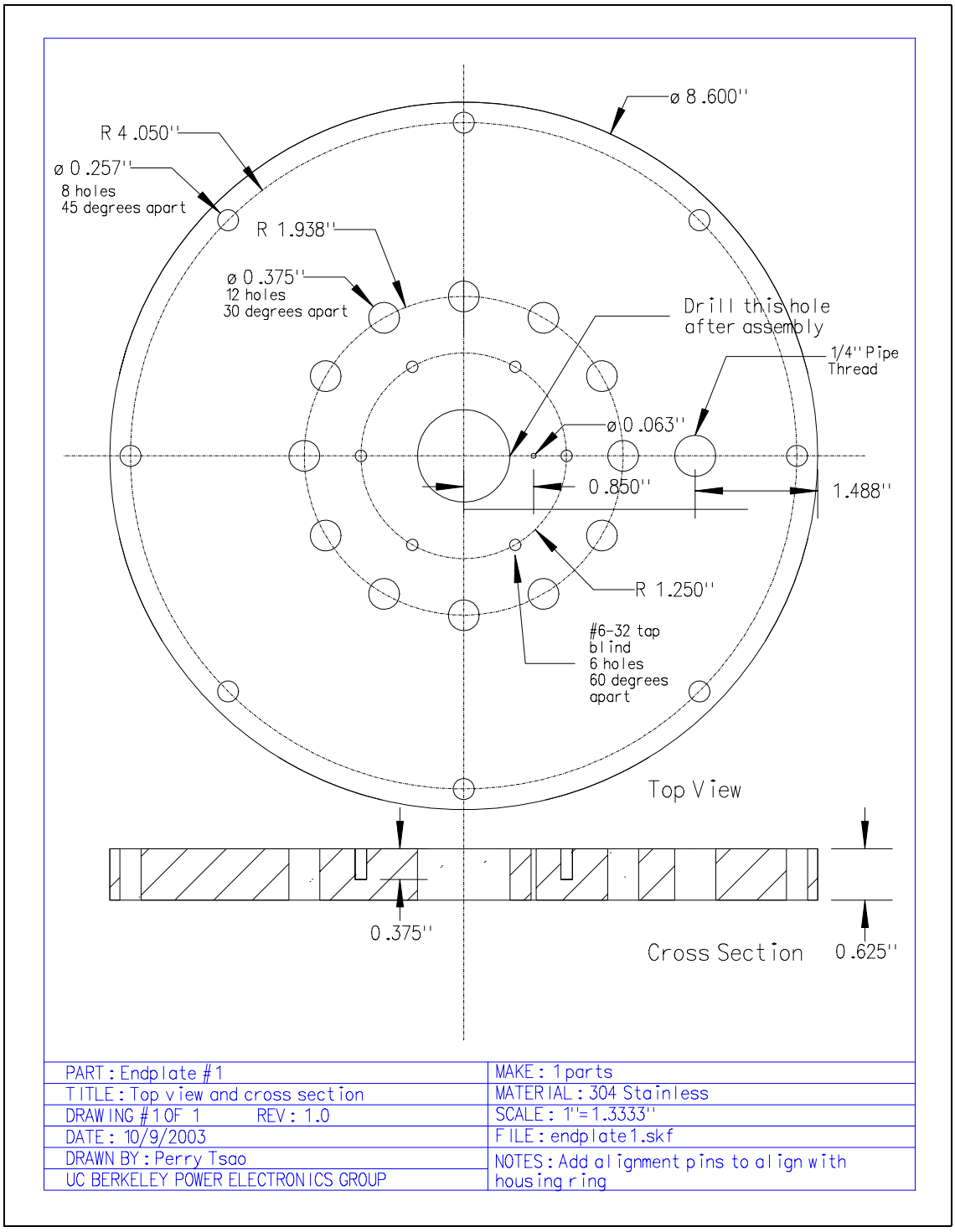


Figure A.3: Drawing of endplate #1.

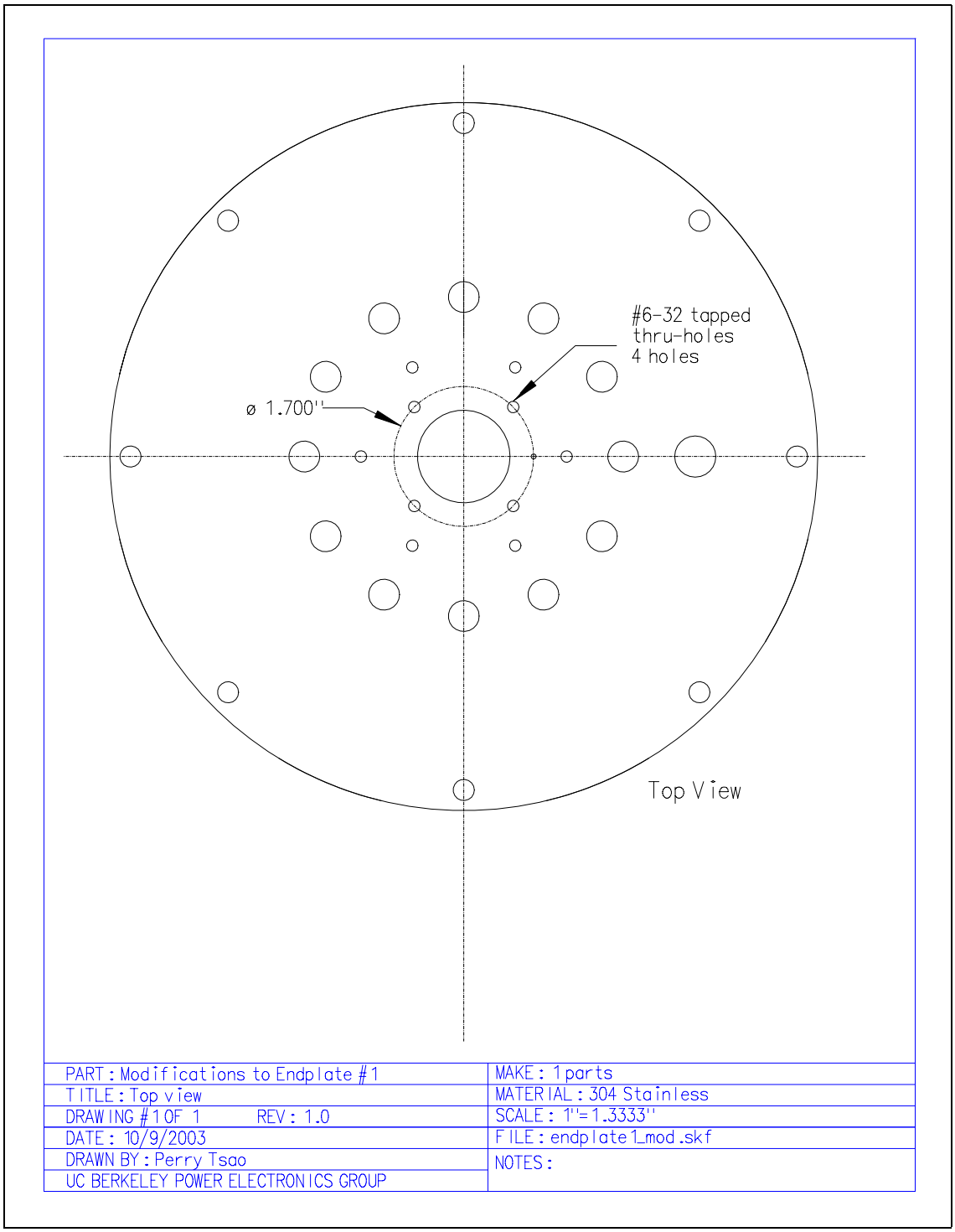


Figure A.4: Drawing of modifications made to endplate #1. These modifications were made to allow the mounting of a retainer for the tolerance ring.

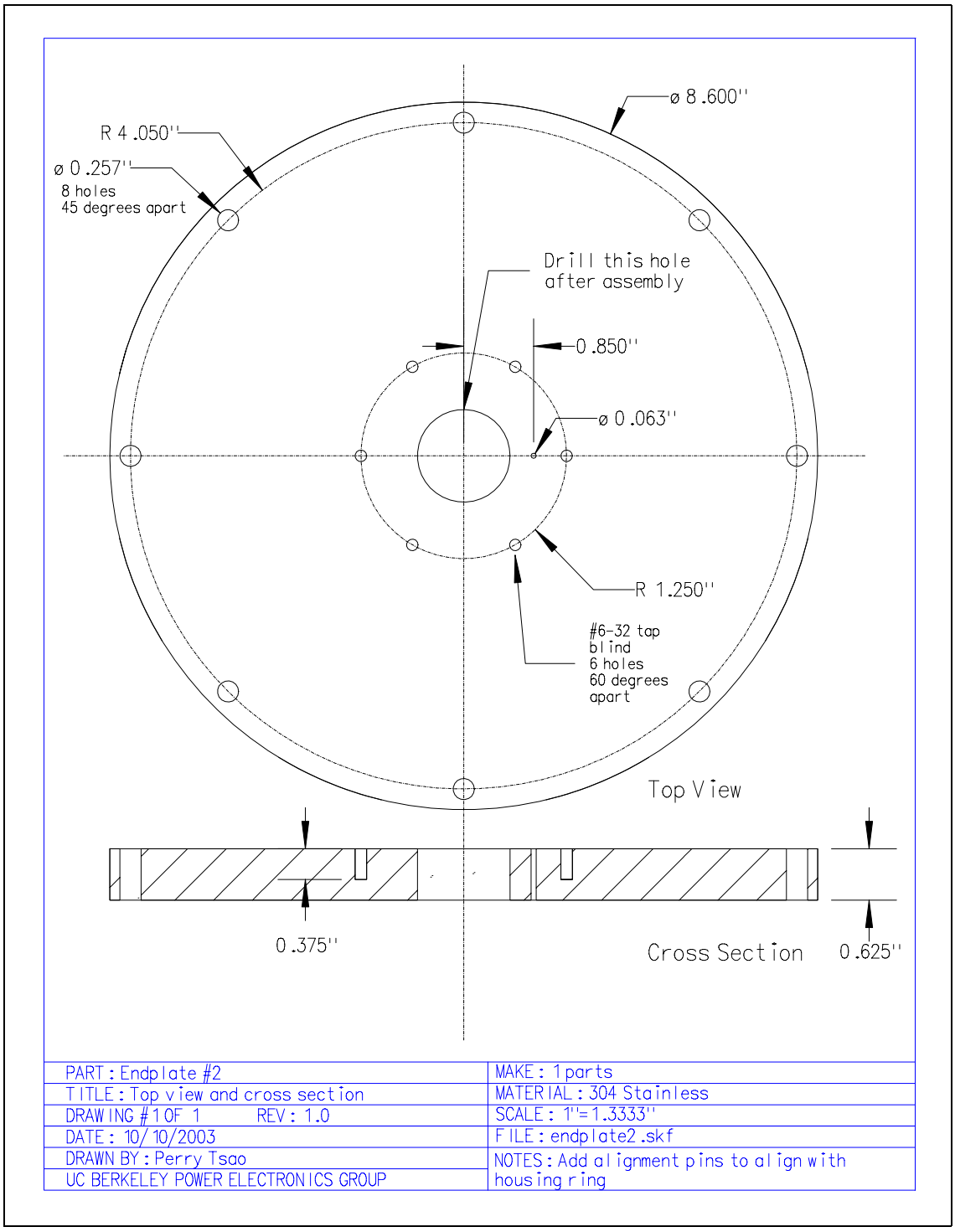


Figure A.5: Drawing of endplate #2.

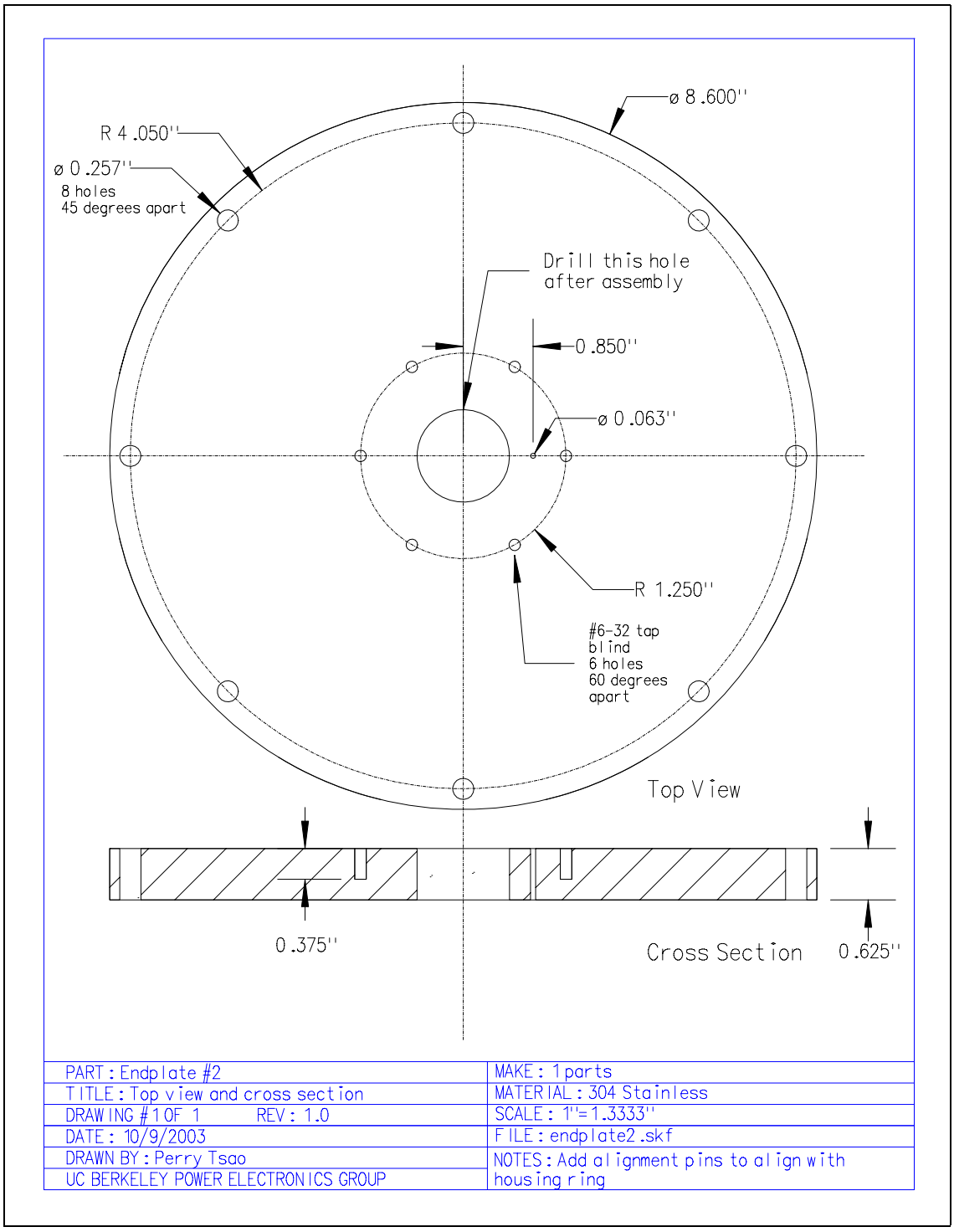


Figure A.6: Drawing of modifications made to endplate #2. These modifications were made to allow the mounting of a retainer for the tolerance ring.

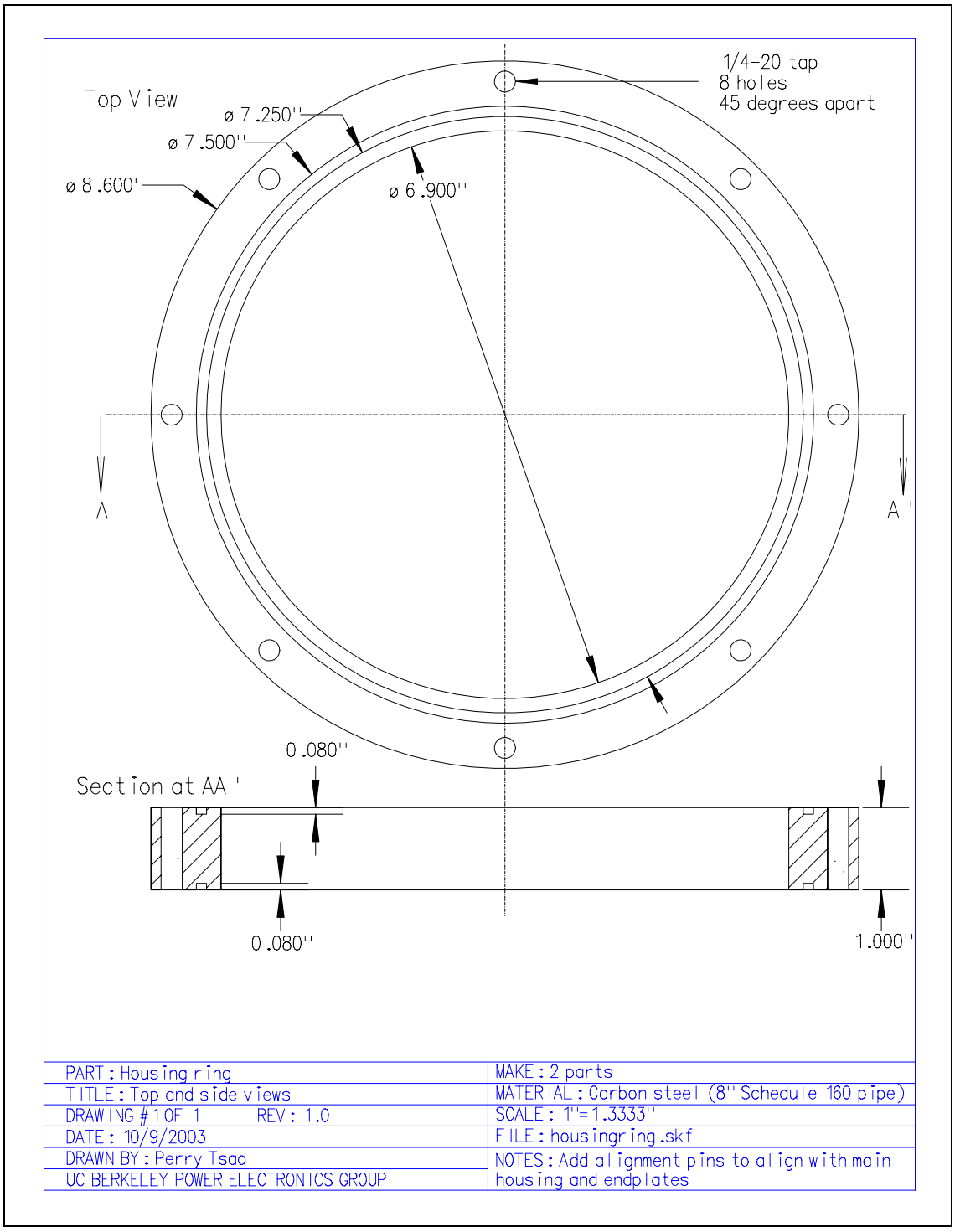


Figure A.7: Drawing of housing ring.

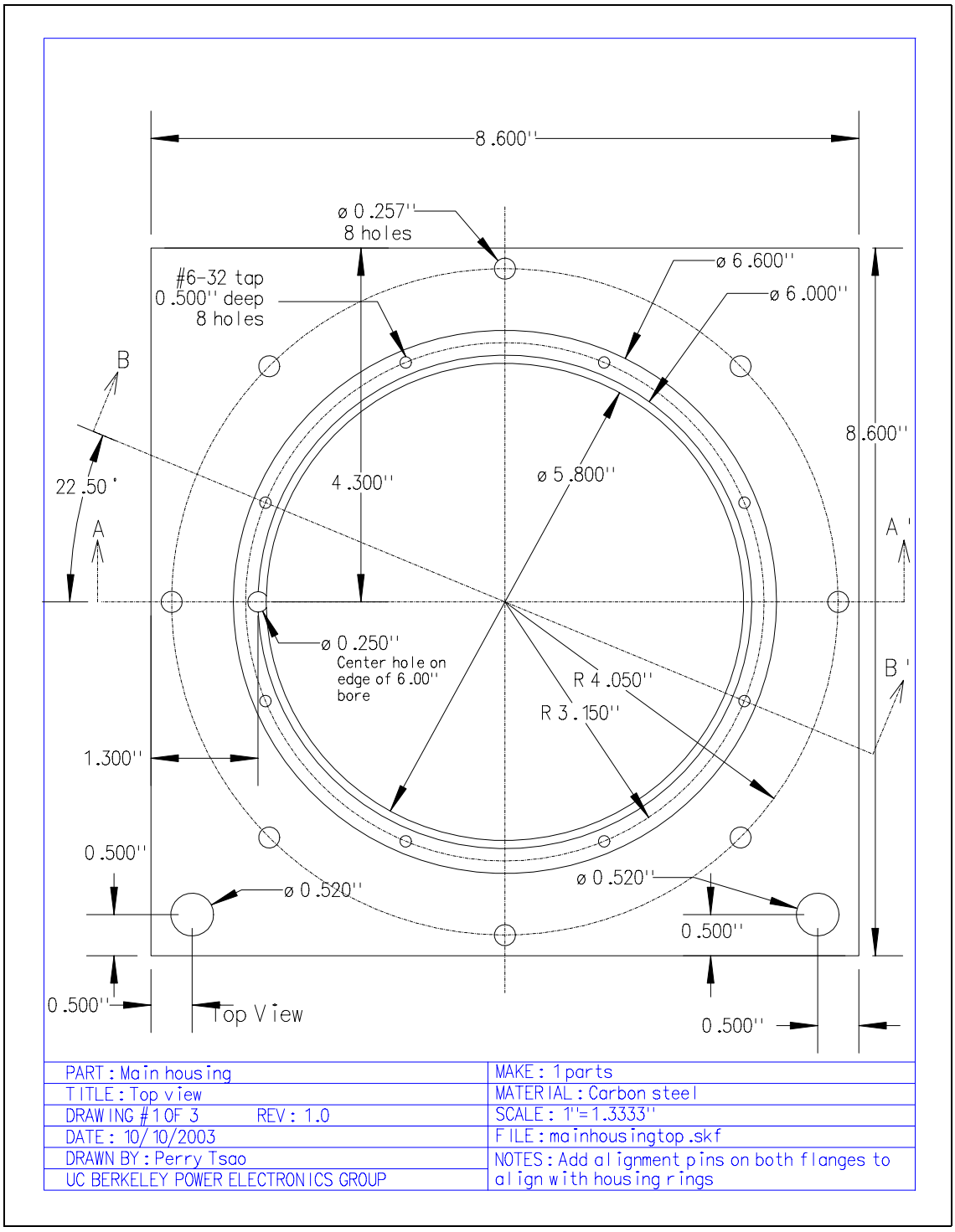


Figure A.8: Top view of main housing.

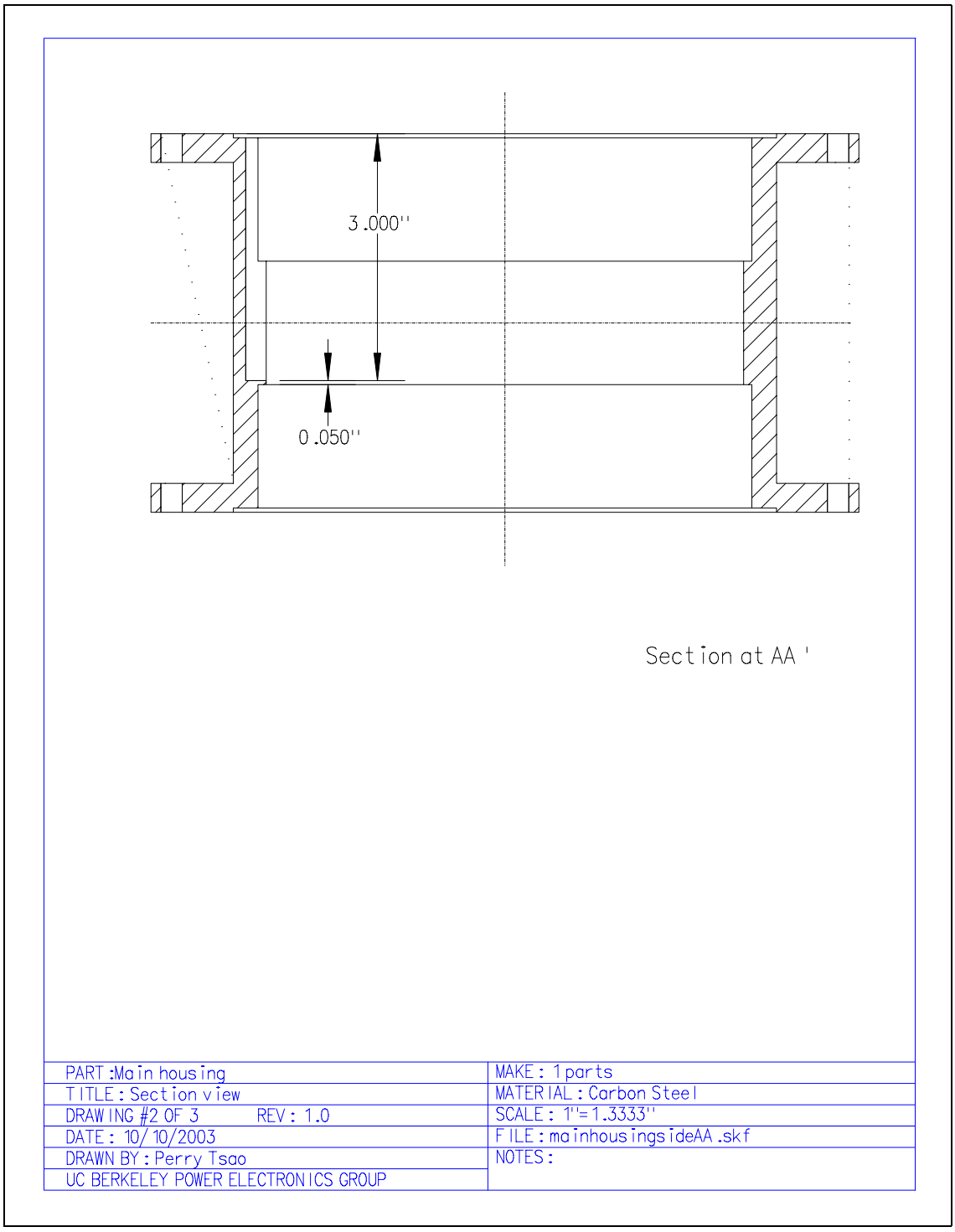


Figure A.9: Section view of main housing at AA' (as labeled in Fig. A.8).

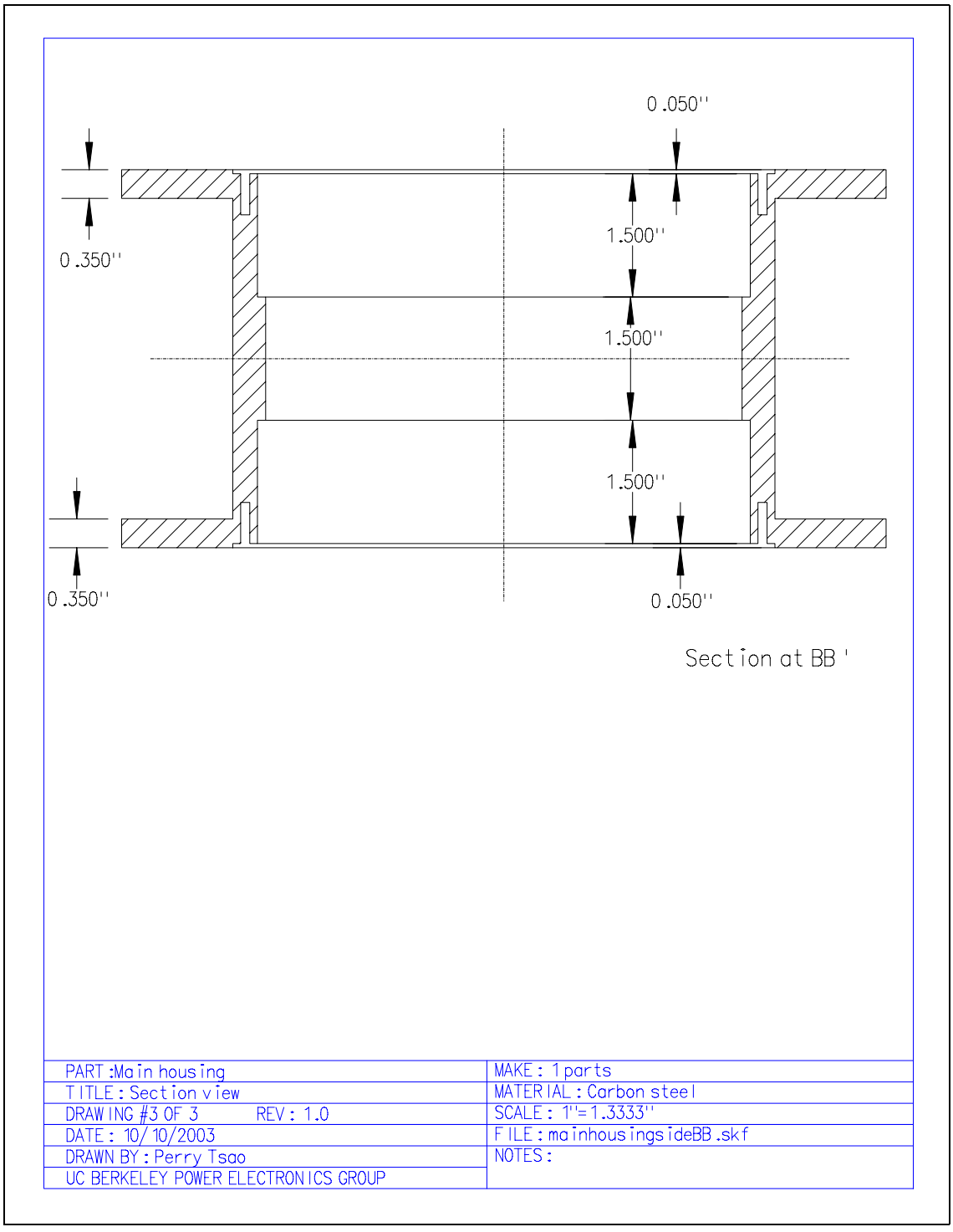


Figure A.10: Section view of main housing at BB' (as labeled in Fig. A.8).

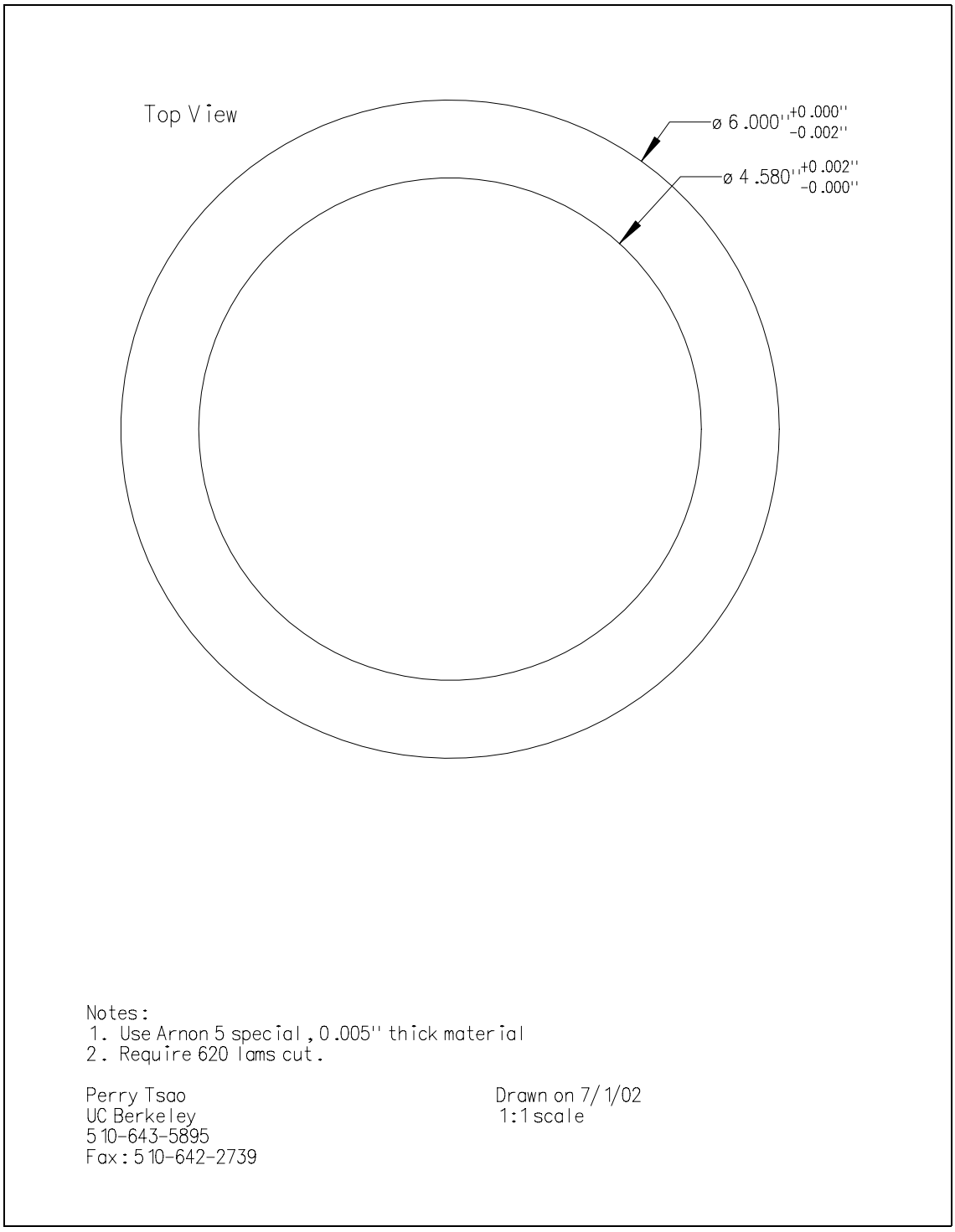


Figure A.11: Pattern for stator laminations.

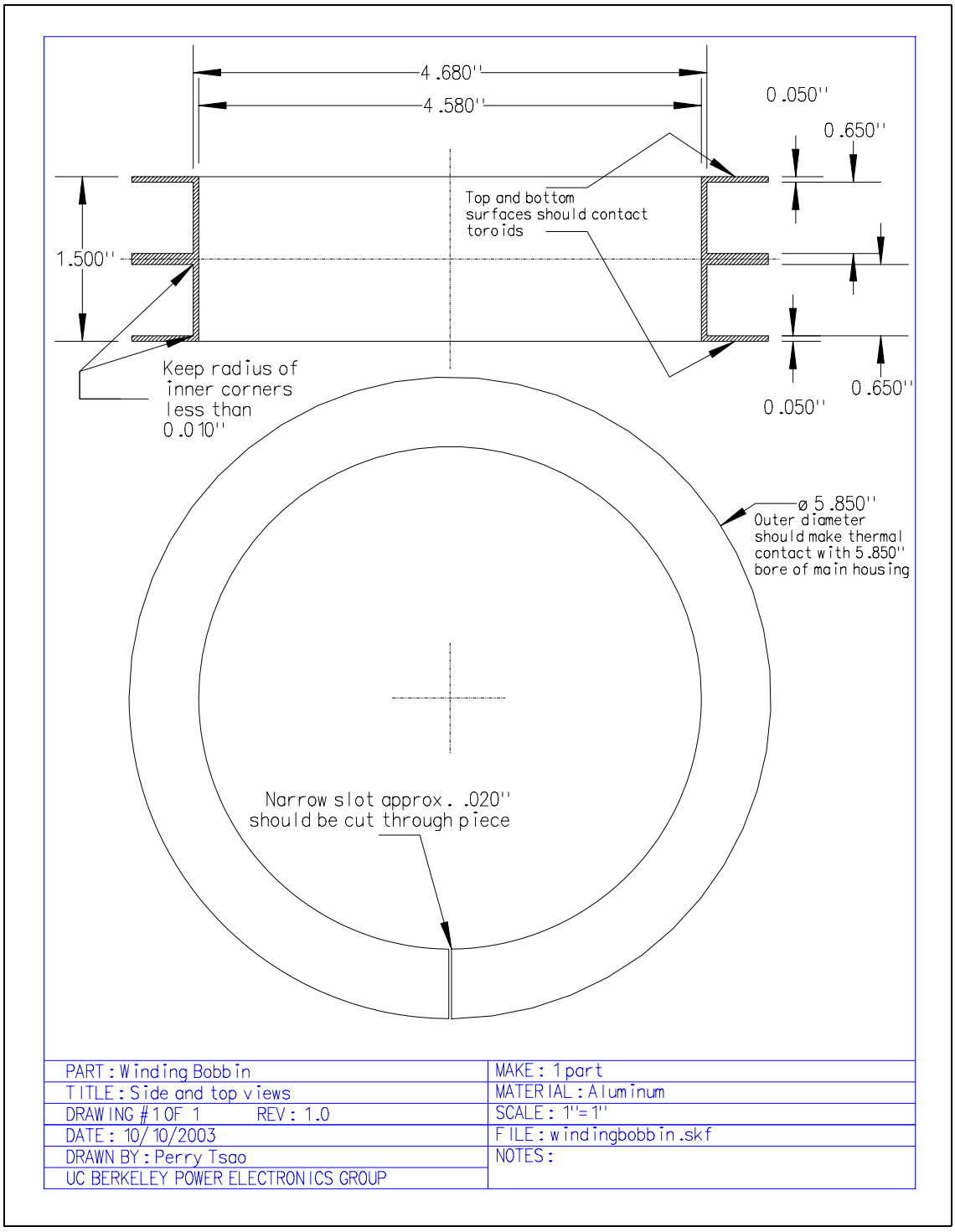


Figure A.12: Drawing of winding bobbin.

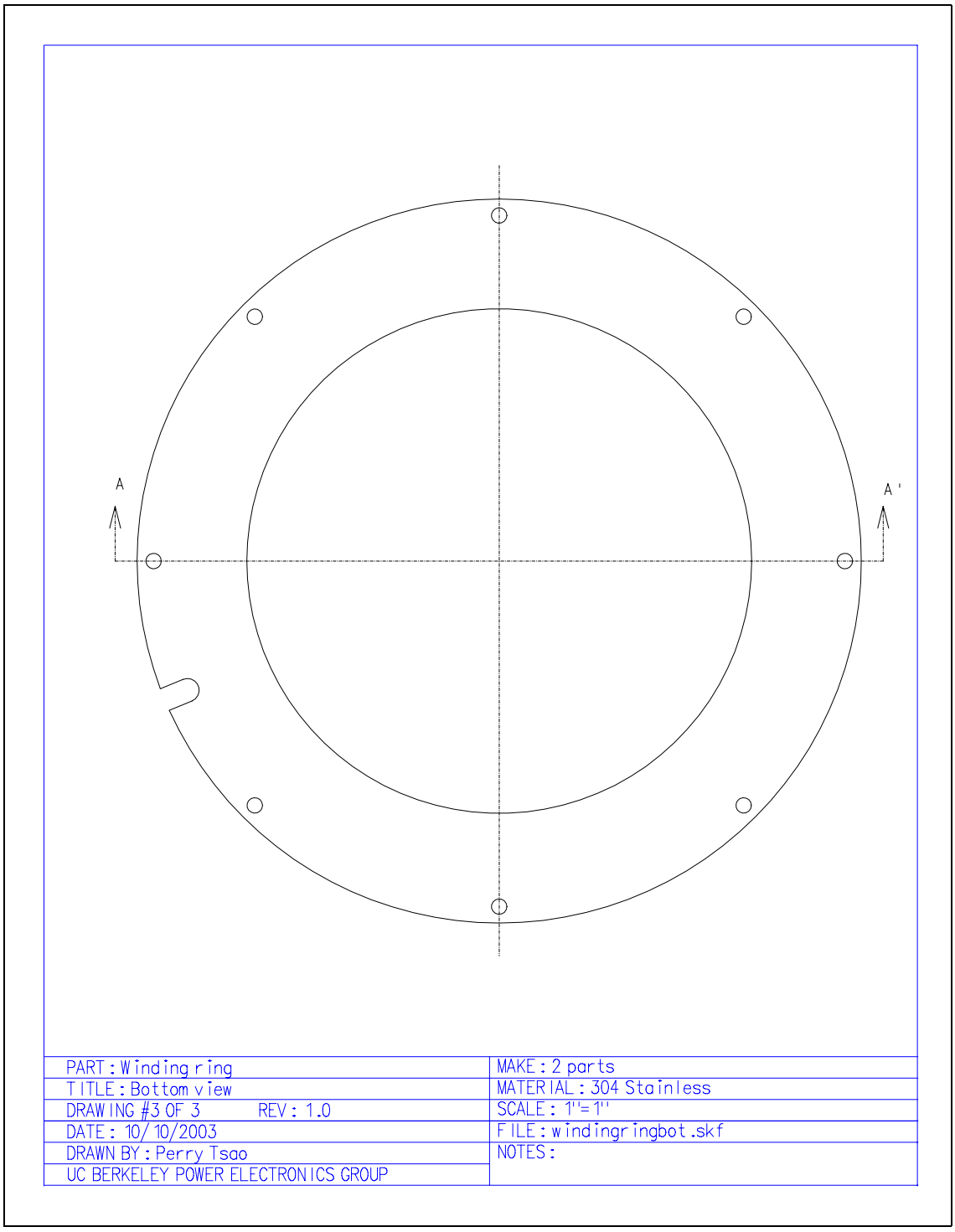


Figure A.13: Bottom view of winding ring.

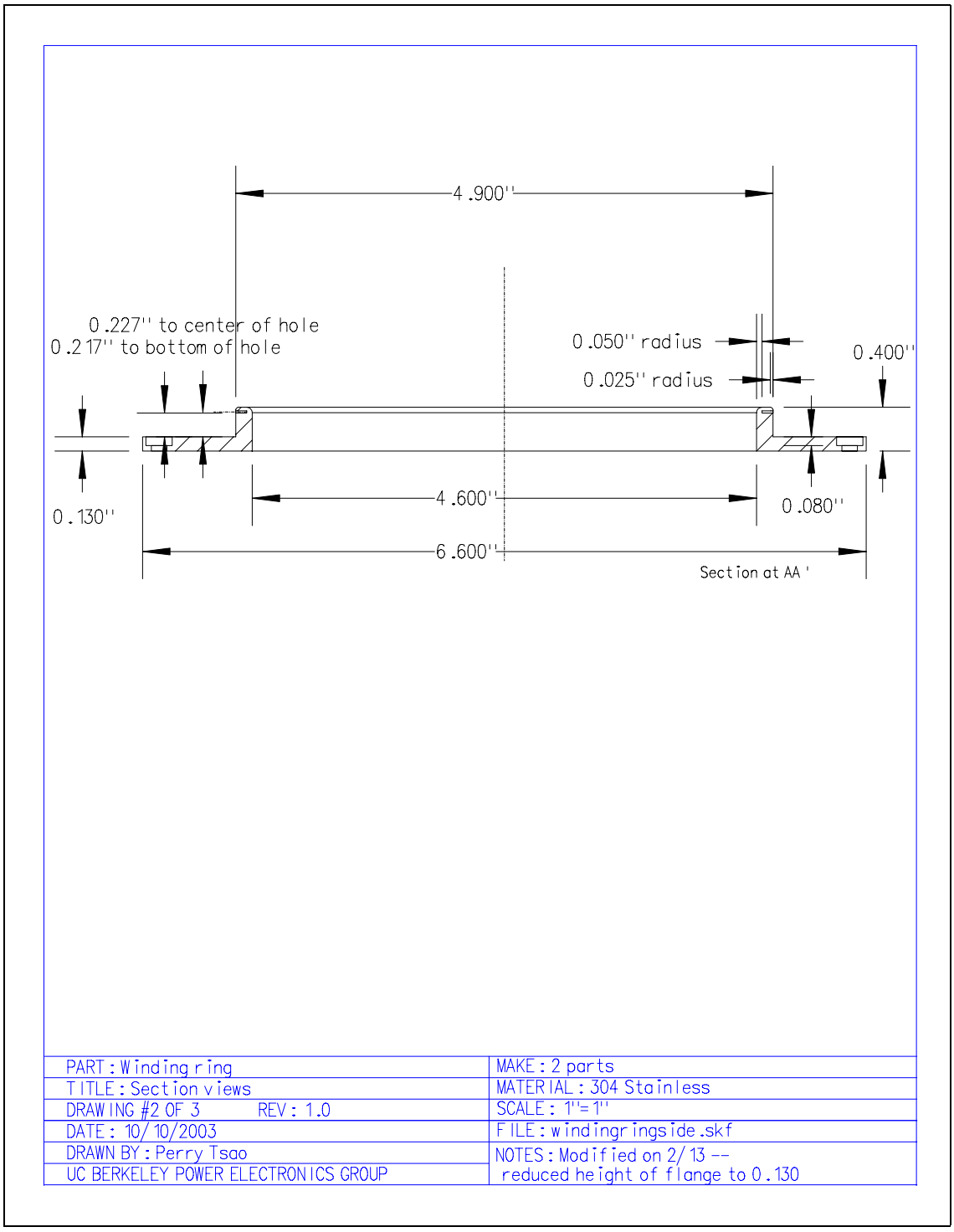


Figure A.14: Side view of winding ring. Note that this part was later modified, and the radially oriented holes were removed when the vertical portion of the inner lip was cut off.

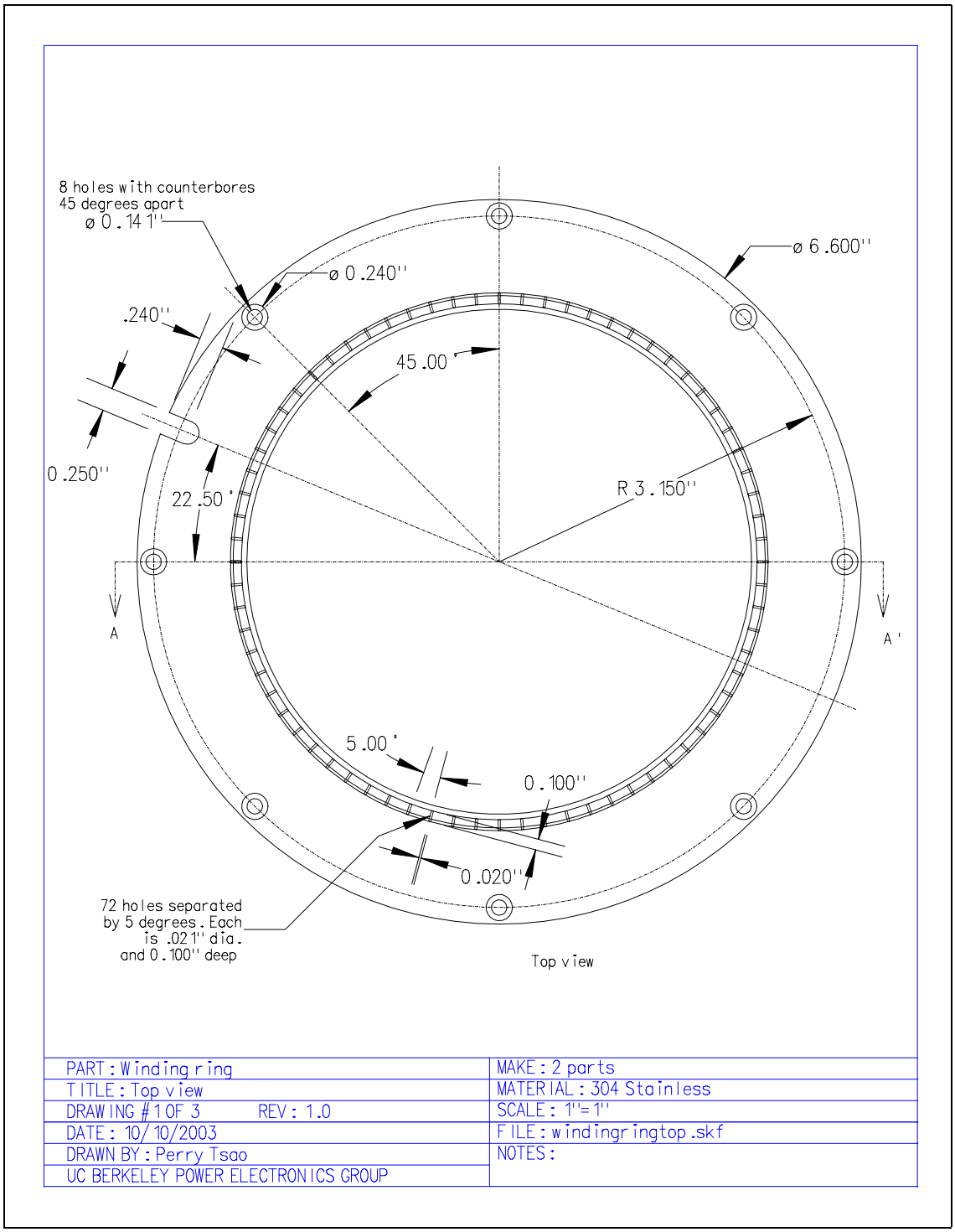


Figure A.15: Top view of winding ring. Note that this part was later modified, and the ring of 72 holes was removed when the vertical portion of the inner lip was cut off.

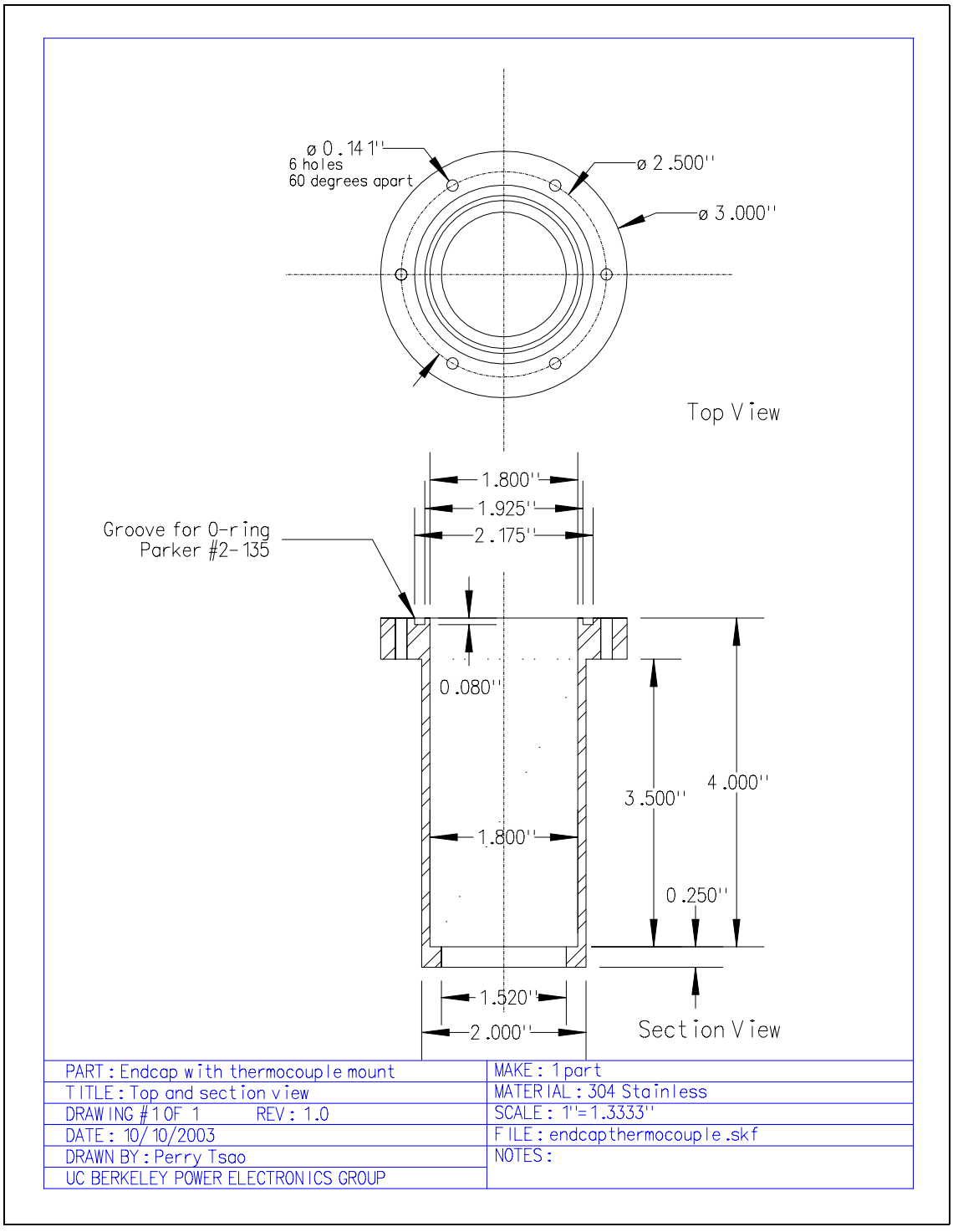


Figure A.16: View of endcap with thermocouple mount.

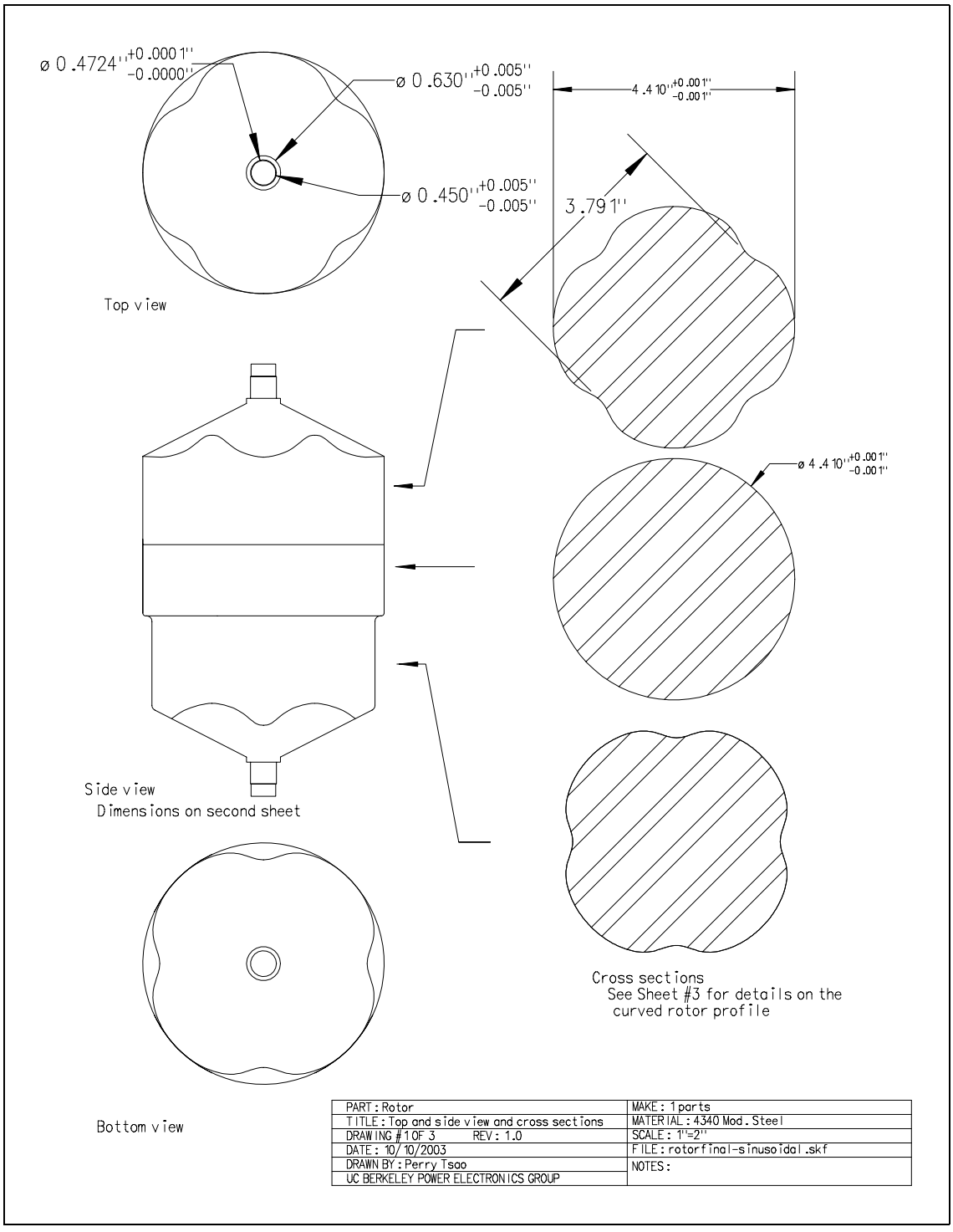


Figure A.17: Drawings of sinusoidal rotor.

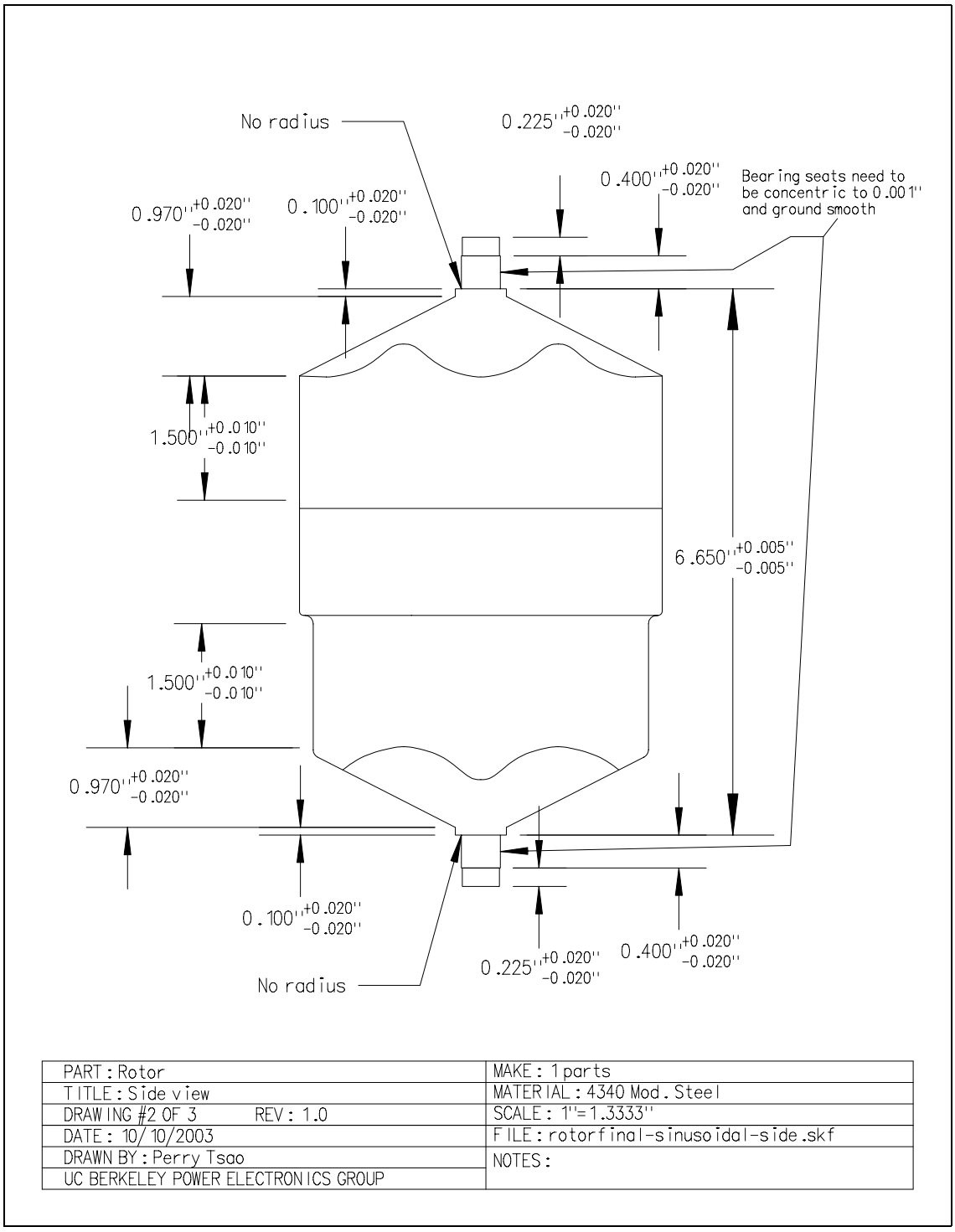


Figure A.18: Side view of sinusoidal rotor.

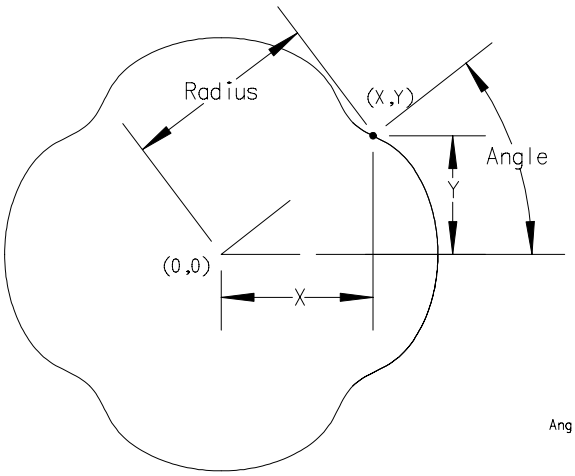


Definitions of Table Values

Profile repeats every 90 degrees

Tolerance is +/- .002

| Angle | Radius | X-Coord. | Y-Coord. | Angle | Radius | X-Coord. | Y-Coord. |
|---|---|---|---|---|---|---|---|
| 0 | 2.205 | 2.205 | 0.000 | 46 | 1.897 | 1.318 | 1.365 |
| 1 | 2.205 | 2.204 | 0.039 | 47 | 1.901 | 1.297 | 1.390 |
| 2 | 2.205 | 2.203 | 0.077 | 48 | 1.908 | 1.277 | 1.418 |
| 3 | 2.204 | 2.201 | 0.115 | 49 | 1.917 | 1.258 | 1.447 |
| 4 | 2.204 | 2.199 | 0.154 | 50 | 1.929 | 1.240 | 1.478 |
| 5 | 2.202 | 2.193 | 0.192 | 51 | 1.943 | 1.223 | 1.510 |
| 6 | 2.204 | 2.192 | 0.230 | 52 | 1.958 | 1.206 | 1.543 |
| 7 | 2.200 | 2.184 | 0.268 | 53 | 1.975 | 1.189 | 1.578 |
| 8 | 2.199 | 2.178 | 0.306 | 54 | 1.991 | 1.170 | 1.611 |
| 9 | 2.199 | 2.172 | 0.344 | 55 | 2.009 | 1.152 | 1.645 |
| 10 | 2.196 | 2.163 | 0.381 | 56 | 2.029 | 1.135 | 1.682 |
| 11 | 2.195 | 2.155 | 0.419 | 57 | 2.047 | 1.115 | 1.716 |
| 12 | 2.193 | 2.145 | 0.456 | 58 | 2.060 | 1.092 | 1.747 |
| 13 | 2.192 | 2.136 | 0.493 | 59 | 2.074 | 1.068 | 1.778 |
| 14 | 2.187 | 2.122 | 0.529 | 60 | 2.089 | 1.045 | 1.809 |
| 15 | 2.185 | 2.110 | 0.565 | 61 | 2.100 | 1.018 | 1.836 |
| 16 | 2.182 | 2.097 | 0.601 | 62 | 2.111 | 0.991 | 1.864 |
| 17 | 2.179 | 2.084 | 0.637 | 63 | 2.121 | 0.963 | 1.889 |
| 18 | 2.174 | 2.068 | 0.672 | 64 | 2.130 | 0.934 | 1.914 |
| 19 | 2.171 | 2.052 | 0.707 | 65 | 2.137 | 0.903 | 1.937 |
| 20 | 2.167 | 2.036 | 0.741 | 66 | 2.144 | 0.872 | 1.959 |
| 21 | 2.160 | 2.016 | 0.774 | 67 | 2.149 | 0.840 | 1.978 |
| 22 | 2.156 | 1.999 | 0.808 | 68 | 2.156 | 0.808 | 1.999 |
| 23 | 2.149 | 1.978 | 0.840 | 69 | 2.160 | 0.774 | 2.016 |
| 24 | 2.144 | 1.959 | 0.872 | 70 | 2.167 | 0.741 | 2.036 |
| 25 | 2.137 | 1.937 | 0.903 | 71 | 2.171 | 0.707 | 2.052 |
| 26 | 2.130 | 1.914 | 0.934 | 72 | 2.174 | 0.672 | 2.068 |
| 27 | 2.121 | 1.889 | 0.963 | 73 | 2.179 | 0.637 | 2.084 |
| 28 | 2.111 | 1.864 | 0.991 | 74 | 2.182 | 0.601 | 2.097 |
| 29 | 2.100 | 1.836 | 1.018 | 75 | 2.185 | 0.565 | 2.110 |
| 30 | 2.089 | 1.809 | 1.045 | 76 | 2.187 | 0.529 | 2.122 |
| 31 | 2.074 | 1.778 | 1.068 | 77 | 2.192 | 0.493 | 2.136 |
| 32 | 2.060 | 1.747 | 1.092 | 78 | 2.193 | 0.456 | 2.145 |
| 33 | 2.047 | 1.716 | 1.115 | 79 | 2.195 | 0.419 | 2.155 |
| 34 | 2.029 | 1.682 | 1.135 | 80 | 2.196 | 0.381 | 2.163 |
| 35 | 2.009 | 1.645 | 1.152 | 81 | 2.199 | 0.344 | 2.172 |
| 36 | 1.991 | 1.611 | 1.170 | 82 | 2.199 | 0.306 | 2.178 |
| 37 | 1.975 | 1.578 | 1.189 | 83 | 2.200 | 0.268 | 2.184 |
| 38 | 1.958 | 1.543 | 1.206 | 84 | 2.204 | 0.230 | 2.192 |
| 39 | 1.943 | 1.510 | 1.223 | 85 | 2.202 | 0.192 | 2.193 |
| 40 | 1.929 | 1.478 | 1.240 | 86 | 2.204 | 0.154 | 2.199 |
| 41 | 1.917 | 1.447 | 1.258 | 87 | 2.204 | 0.115 | 2.201 |
| 42 | 1.908 | 1.418 | 1.277 | 88 | 2.205 | 0.077 | 2.203 |
| 43 | 1.901 | 1.390 | 1.297 | 89 | 2.205 | 0.039 | 2.204 |
| 44 | 1.897 | 1.365 | 1.318 | 90 | 2.205 | 0.000 | 2.205 |
| 45 | 1.895 | 1.340 | 1.340 | | | | |

| | |
|---|---|
| PART : Rotor | MAKE : 1 parts |
| TITLE : Curved Profile | MATERIAL : 4340 Mod. Steel |
| DRAWING #3 OF 3 REV : 1.0 | SCALE : 1"=1.3333" |
| DATE : 10/10/2003 | FILE : rotorfinal-sinusoidal-profile.skf |
| DRAWN BY : Perry Tsao | NOTES : |
| UC BERKELEY POWER ELECTRONICS GROUP | |

Figure A.19: View of sinusoidal rotor profile.

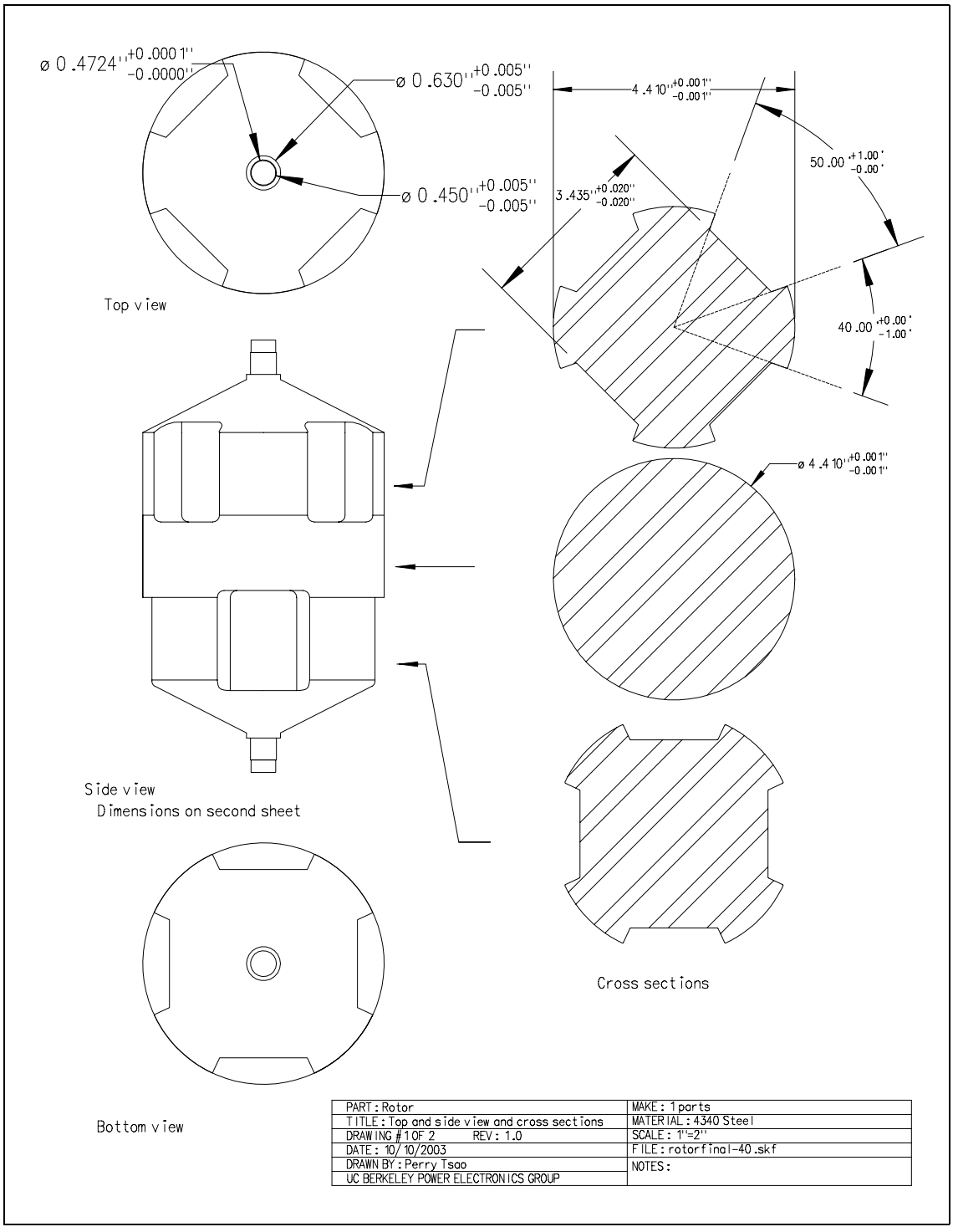


Figure A.20: Drawings of square-cut rotor.

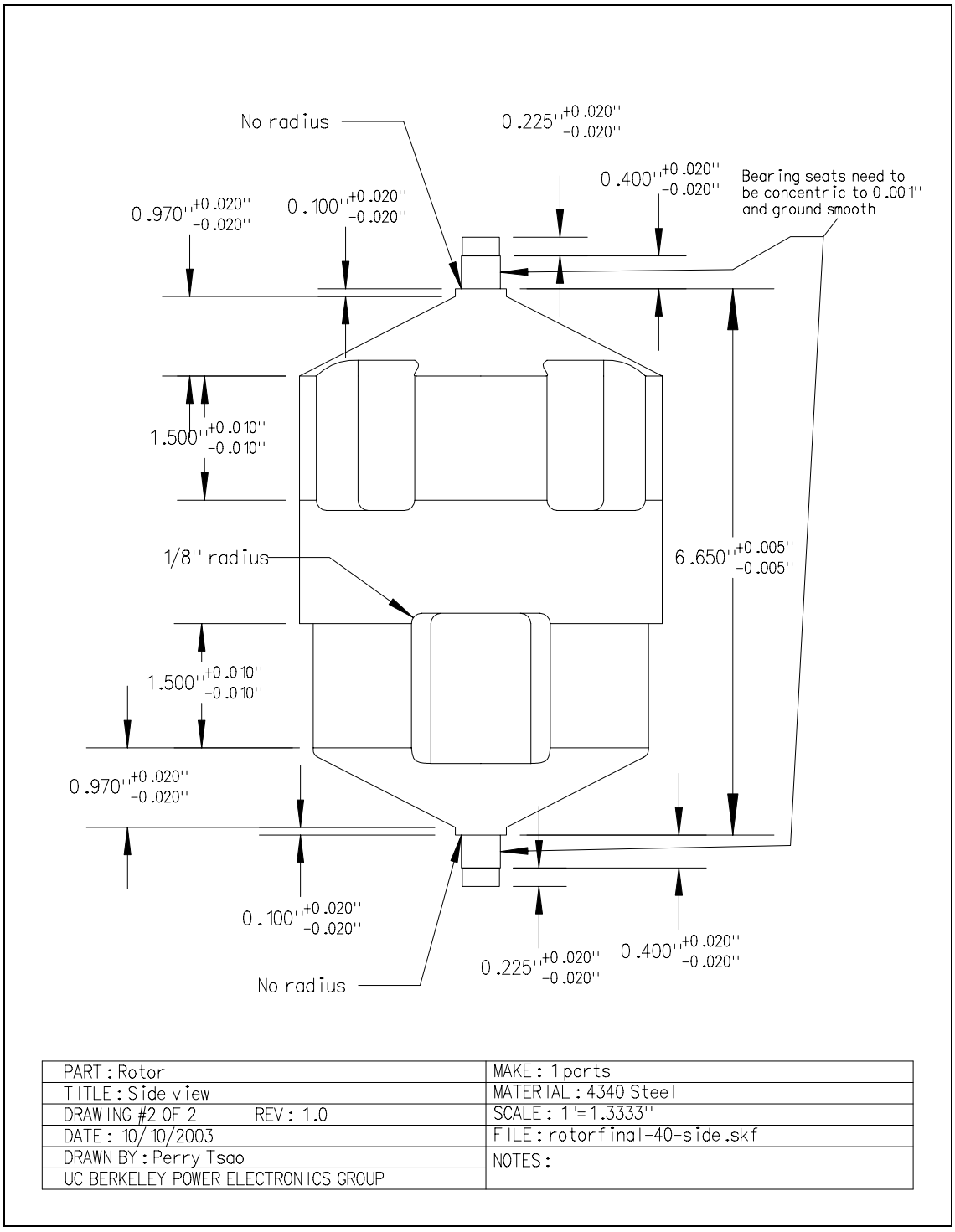


Figure A.21: Side-view of square-cut rotor.

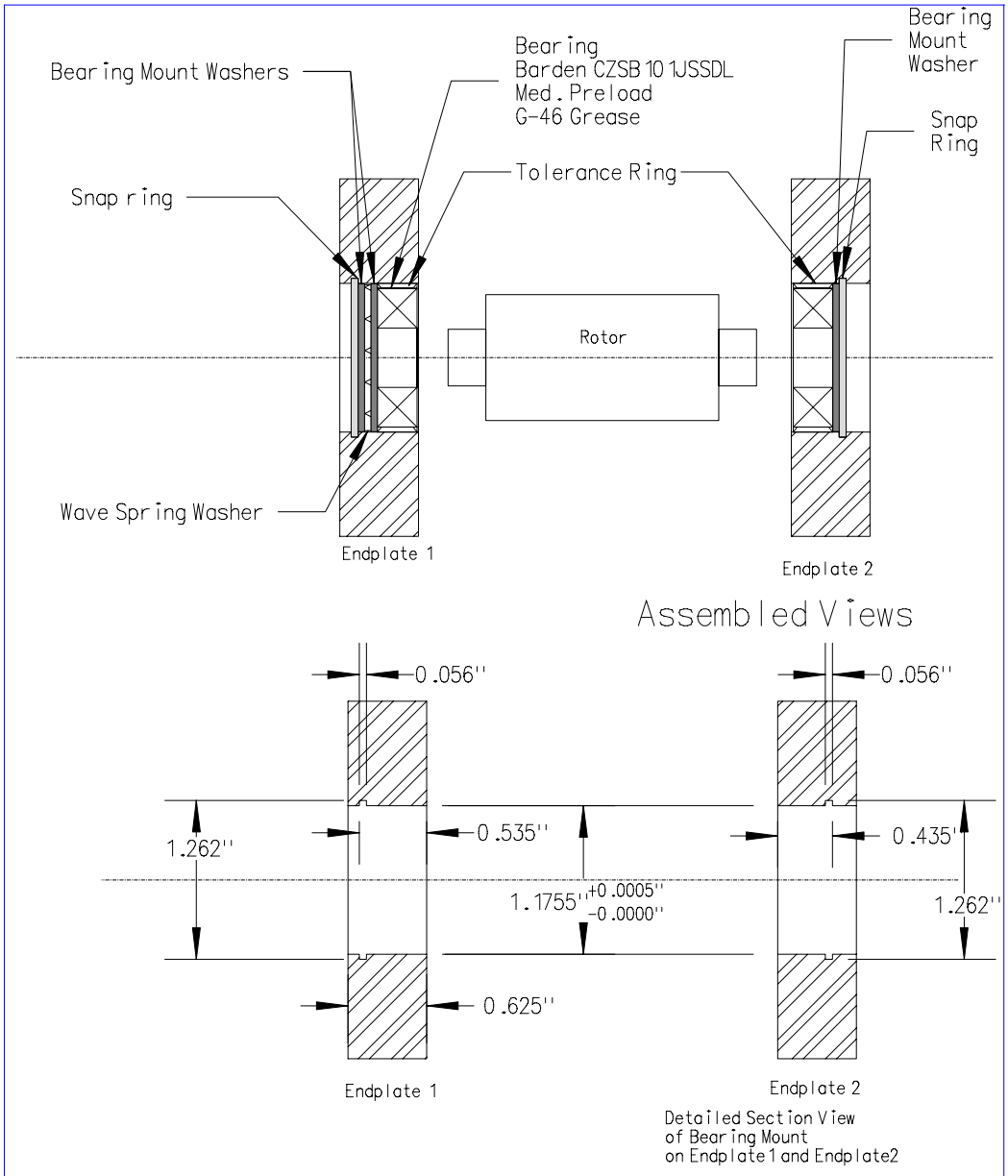


Figure A.22: Detail of bearing mount system. The tolerance ring retainer was added later and is not shown.

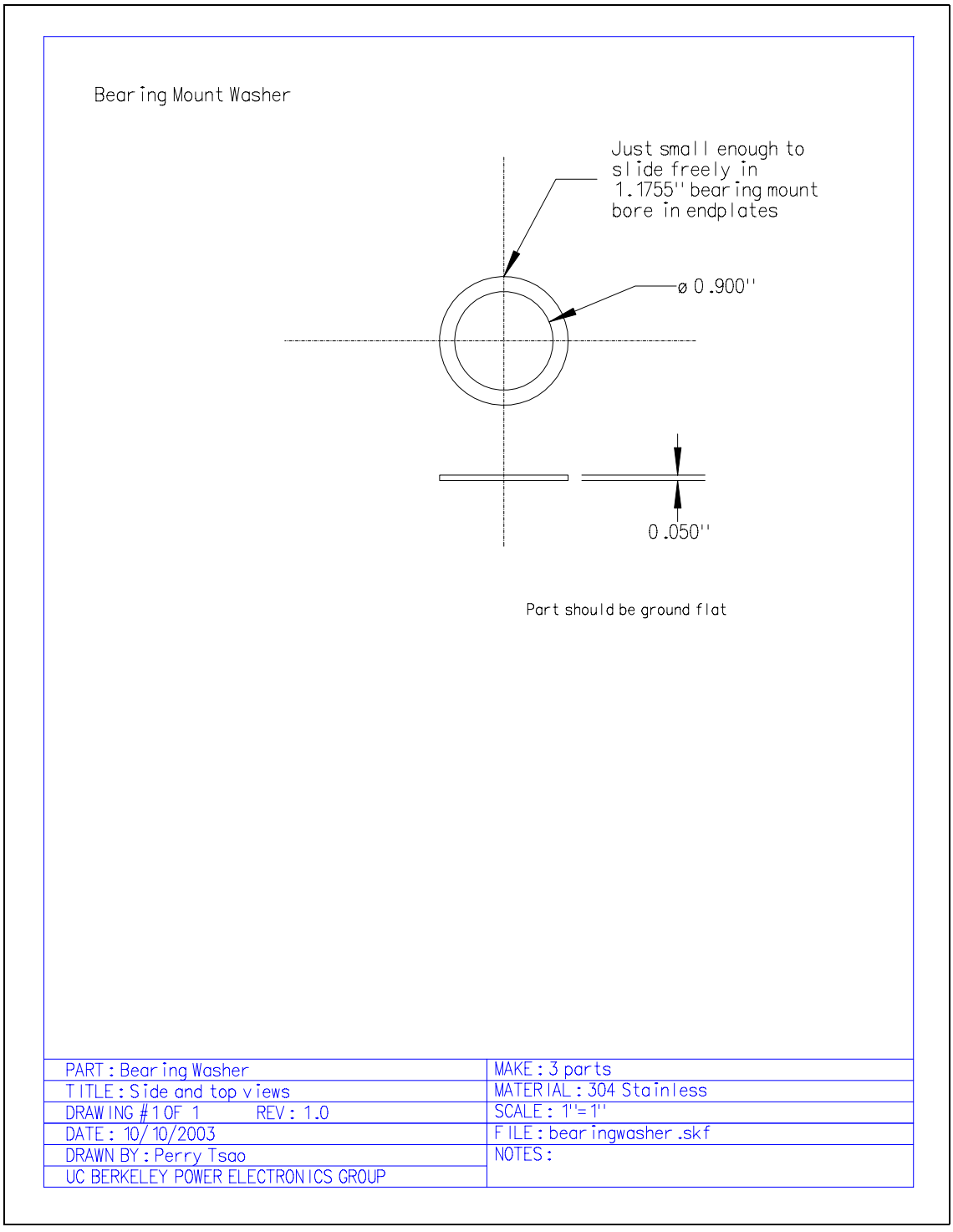


Figure A.23: Drawing of bearing washer.

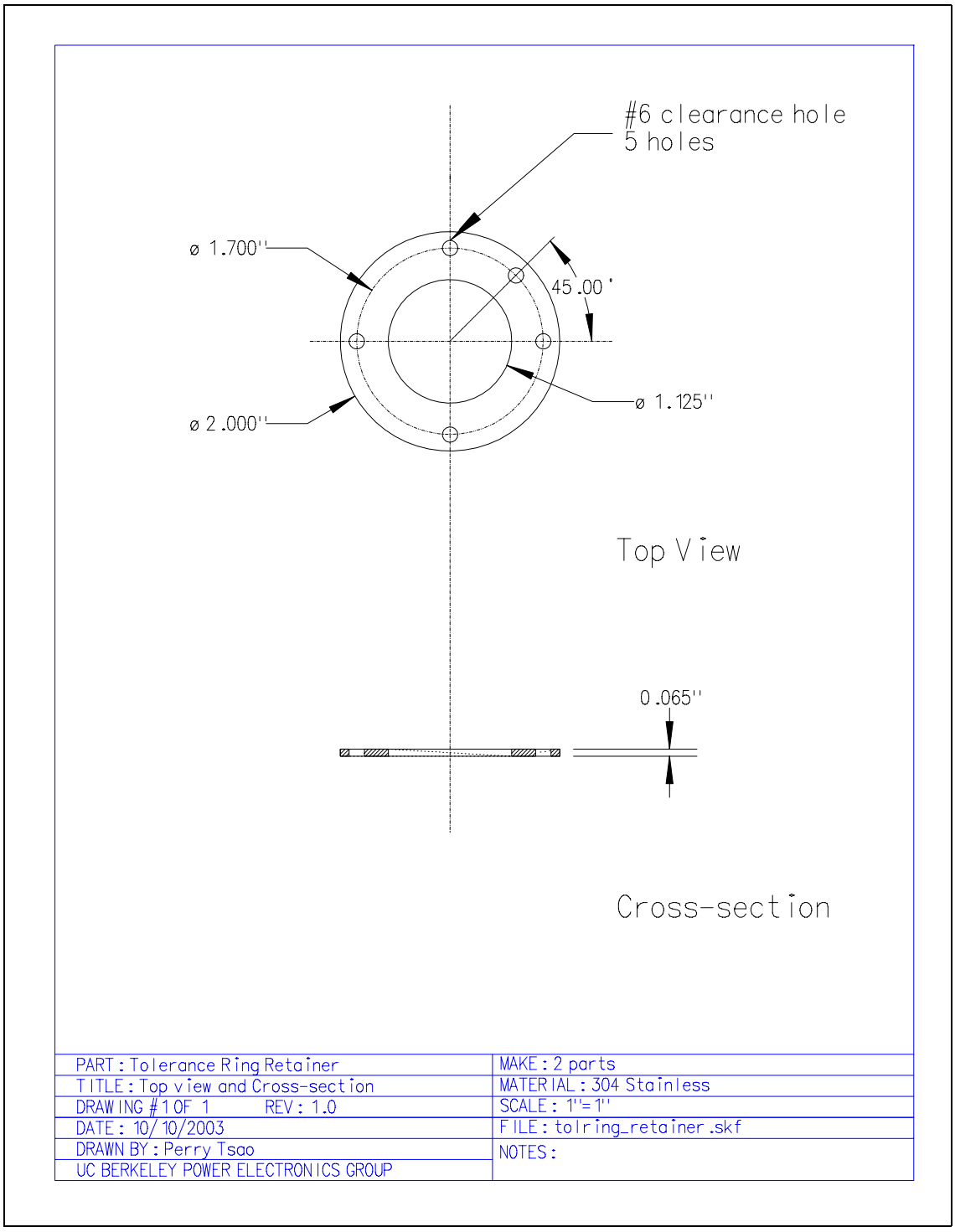


Figure A.24: Drawing of tolerance ring retainer.

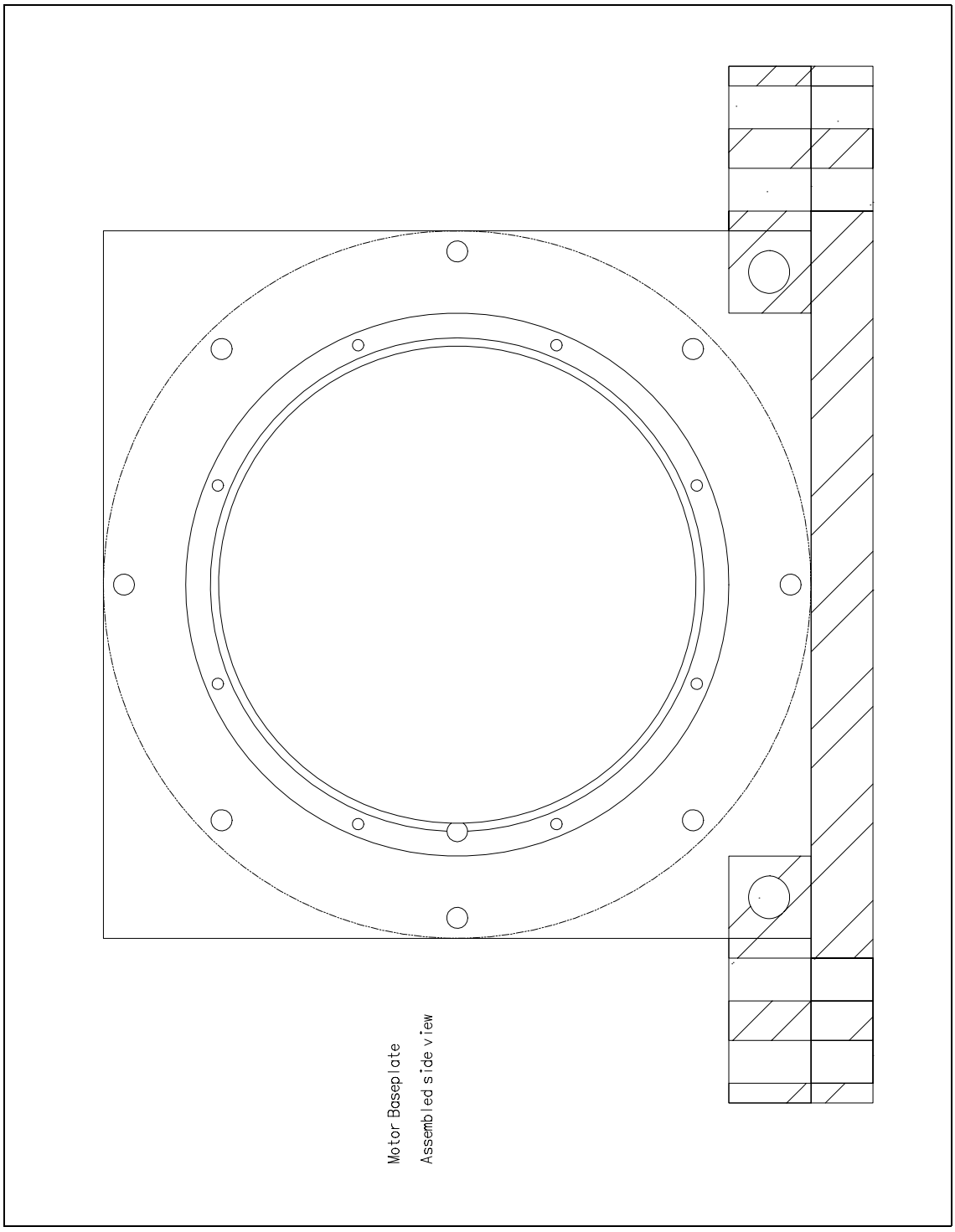


Figure A.25: Side view of assembled flywheel mounted on its baseplate.

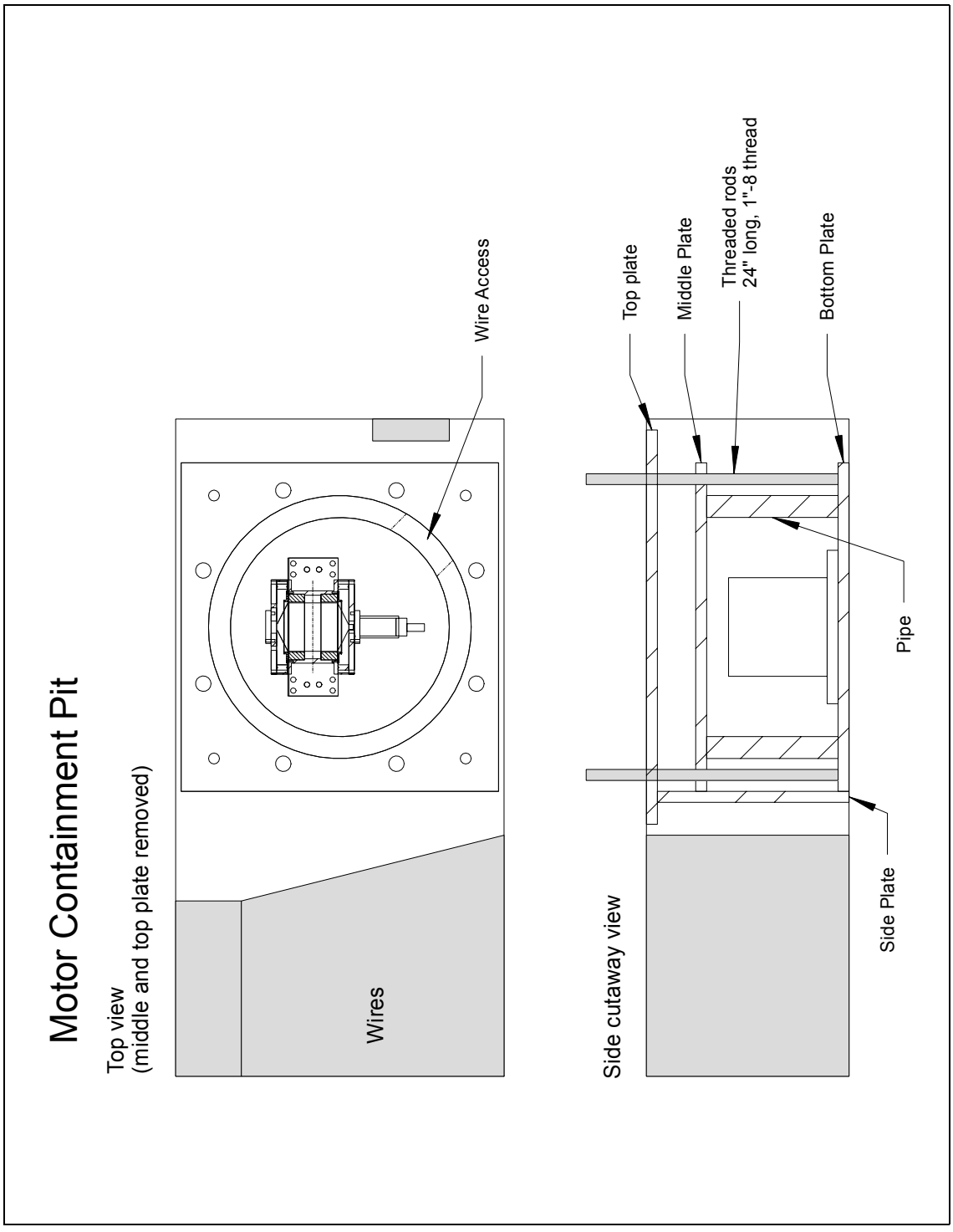


Figure A.26: Assembled view of flywheel system in the containment system.

# Appendix B

# Software and Data Files

This Appendix describes the primary computer files used in this thesis which have been archived on a CD-ROM. The table below lists the directories and files on the disc and their description. Files are listed indented under their directory names.

Table B.1: List of files and directories on CD-ROM

| Directory or filename | Description |
|---|---|
| drawings | Computer files for all drawings in Appendix A and others. In Autosketch 6.0 .SKF format. |
| fire | Directory of files on the computer named Fire, the computer that was connected to the dSPACE control card. |
| files on fire.txt | Description of where key files are located on Fire. |
| fire.tar.gz | Archive of relevant files on Fire. |
| photos | Photos of the flywheel parts, test setup, and oscilloscope captures of experiments. |
| matlab.zip | Zip file of all the matlab scripts used in this thesis. |
| thesis.pdf | The text of this thesis in .pdf format |
| thesis.ps | The text of this thesis in Postscript format |
| testdata | Directory of Matlab .mat files of data collected during testing. Not all data has been included. |